Studies on structure and function of ribonuclease H2

Misato Baba

2020

Contents

Abbreviations

Amp	ampicillin
AGS	Aicardi-Goutières syndrome
CD	circular dichroism
cGAS	cyclic GMP-AMP synthase
CRISPR	clustered regularly interspaced short palindromic repeat
CXCL10	CC-X-C motif chemokine 10
DTT	dithiothreitol
DSB	double strand DNA break
E. coli	*Escherichia coli*
EDTA	ethylenediaminetetraacetic acid
EthBr	ethidium bromide
GFC	gel filtration chromatography
GPMA	genome profiling-based mutation assay
IFIT	interferon-induced proteins with tetratricopeptide repeat
IPTG	isopropyl 1-thio-β-D-galactoside
IRF	interferon regulatory factor
ISG	interferon stimulated gene
k_{cat}	molecular activity
K_e	proton dissociation constant
KO	knockout
PAGE	polyacrylamide gel electrophoresis
PaSS	pattern similarity score

PCR	polymerase chain reaction
RER	ribonucleotide excision repair
RNase H	ribonuclease H
SDS	sodium dodecyl sulfate
sgRNA	single guide RNA
STING	stimulator of interferon gene
TGGE	temperature gradient gel electrophoresis
T_m	melting temperature
WT	wild-type enzyme

General introduction

Ribonuclease H (RNase H) [EC 3.1.26.4] is the enzyme that specifically hydrolyzes the 5'-phosphodiester bond of the RNA components of RNA/DNA hybrids. RNase H is present ubiquitously in a variety of organisms, ranging from bacteria to human. RNase H is classified into two groups, type I and type II. Type I RNase H has an activity to degrade the RNA-strand of RNA/DNA hybrids but does not have an activity to incise the 5'-phosphodiester bond of a single ribonucleotide embedded in DNA double strands. Type II RNase H has both of the activities, namely the RNA-strand degrading activity and the single-ribonucleotide incision activity (1–3).

Eukaryote type II RNase H (RNase H2) is composed of three different subunits, one catalytic subunit (A) and two accessory subunits (B and C). The active site has the conserved DEDD motif to express the activity and DSK and GRG motifs to recognize the substrate (4). For the catalysis, a two-metal-ion catalysis mechanism has been proposed, in which two divalent cations (e.g. Mg^{2+} or Mn^{2+}) coordinated by the scissile phosphate group of the substrate and by all amino acid residues of DEDD motif, play an essential role in activating a water molecule for the nucleophilic attack to the 5'-phosphorus atom (5).

Recently, replicative DNA polymerases incorporate a single ribonucleotide every few thousand base pairs. If remain unrepaired, such ribonucleotides can cause double strand DNA breaks, leading to mutation, cell death, and onset of cancer and other genetic diseases (6–8). RNase H2 is involved in the removal of ribonucleotides embedded in genomic DNA, via the first process of ribonucleotide excision repair (RER) (6).

Increasing attention is being focused on the intracellular roles of RNase H2, particularly in maintaining genomic integrity. In human, a decrease in RNase H2 activity causes Aicardi-Goutières syndrome (AGS), a severe neuroinflammatory disorder (8–10). Genomic analysis of AGS patients identified some mutations in RNase H2 genes (9). However, there is no evidence that directly links the mutations (frequently called AGS-causing mutations) and the onset of AGS. To determine whether AGS-causing mutations are a major cause of AGS, it is necessary to elucidate the effects of the mutations on the structure and function of RNase H2 *in vitro* and *in vivo*.

As described above, intracellular roles of RNase H2 in maintaining genomic integrity are of current interest. It is reasonable to assume that every organism has a system to maintain genomic integrity and to repair DNA lesions, although the capacity of the DNA repair system varies depending on organisms. In recent study, yeast has been used as a model to evaluate the DNA repair capacity (11, 12). However, the amino acid sequence homology of RNases H2 between yeast and human is low, suggesting that the results obtained in yeast are not necessarily applicable to human. To evaluate the DNA repair capacity in human, it is preferable to use mammalian cells.

The aim of this study is to understand the structure and function of RNase H2. In Chapter 1, to characterize the enzymatic properties of human RNase H2, the effects of neutral salts and pH on the enzyme activity were examined. In Chapter 2, to elucidate the effects of AGS-causing mutations on human RNase H2, the activity and stability of six single mutant enzymes were investigated. In Chapter 3, to evaluate the contribution of the active-site residue Val143 of human RNase H2 to catalytic activity and substrate specificity, saturation mutagenesis was used, and the kinetic properties of the resultant variants were determined. In Chapter 4, RNase H2 knockout NIH3T3 cells were

constructed. The accumulation of ribonucleotides in genomic DNA and the expression levels of immune response genes were compared between the RNase H2 knockout and wild-type NIH3T3 cells. In Chapter 5, the applicability of mammalian cells to genome profiling-based mutation assay (GPMA) was assessed. GPMA is a new method to detect mutations in genomic DNA caused by chemicals, and is a potential alternative to Ames test (13). *Escherichia coli*, but not mammalian, cells have been used in GPMA.

The present study contributes to understanding of the structure and function of RNase H2, and sheds new light on the relationship between AGS-causing mutations found in RNase H2 genes and the onset of AGS. We believe that this study serves as an important basis for future analysis of the contribution of RNase H2 to DNA repair capacity in cells.

Chapter 1

Effects of neutral salts and pH on the activity and stability of human RNase H2

Introduction

As described in General introduction, RNase H is involved in processing of various RNA/DNA hybrids. Such hybrids include template RNA/cDNA formed in retroviral replication, RNA primer/DNA formed in lagging strand synthesis, and telomere RNA/DNA formed in telomere elongation. The hybrid identified in recent years is R-loop, a three-strand nucleic acid structure consisting of an RNA/DNA hybrid and a single DNA strand. Recent study has shown that single ribonucleotides are embedded in DNA double strand (6−8). Both type I and II RNases H have the activity to degrade the RNA strand of RNA/DNA hybrids, while only type II has the activity to incise single ribonucleotides, initiating ribonucleotide excision repair (RER) (1−3). The failure of the RNase H-mediated processing of RNA/DNA hybrids leads to double strand DNA break (DSB) of chromosome (1−3). It was reported that DSB is repaired by homologous recombination (HR): cDNA is synthesized from the transcript RNA by reverse transcriptase, followed by the transcript RNA of the resulting RNA/DNA hybrid is degraded by RNase H, and the resulting DNA fragment is used for HR with chromosomal DNA (11, 12).

Recent study of the mechanism of AGS onset has shown that, nucleic acids are accumulated in cells, cGAS/STING works as a nucleic acid-sensing pathway, and innate

immune response is enhanced (14, 15). However, enzymatic characteristics of human RNase H2 remain to be elucidated. In this study, we examined the effects of neutral salts and pH on the activity and stability of recombinant human RNase H2 expressed in *E. coli.*

Materials and Methods

Materials – The 3'FITC-labeled or 5'Dabcyl-labeled 18-mer nucleotides were purchased from Fasmac (Atsugi, Japan). All chemicals were purchased from Nacalai Tesque (Kyoto, Japan).

Expression and purification of recombinant human RNase H2 – E.coli BL21(DE3) [F^-, *ompT*, *hsdS*$_B$ (r_B^- m_B^-) *gal dcm* (DE3)] was transformed with pET15b-hH2ABC, which was the pET-15b(+) plasmid (Merck Bioscience, Tokyo, Japan) harboring the gene encoding A, B, and C subunits of human RNase H2 with a N-terminal $(His)_6$ tag at each subunit (Figs. 1–3). The overnight culture of the transformants (15 ml) was added to 1,500 ml of LB broth in a 2-liter flask and incubated at 30°C under vigorous aeration by air-pump. When OD_{660} reached 0.3, 1.2 ml of 0.5 M IPTG was added and growth was continued for 3 h.

After centrifugation at 10,000 × *g* for 10 min, the cells were harvested, suspended with 15 ml of 20 mM Tris-HCl buffer (pH 7.5), 1 mM EDTA, 1 mM DTT (buffer A) and disrupted by sonication. After centrifugation at 20,000 × *g* for 40 min, the supernatant was collected and applied to a HiTrap Heparin HP column (GE Healthcare, Buckinghamshire, UK) previously equilibrated with buffer A. After the wash with

buffer A containing 0.2 M NaCl, the bound RNase H2 was eluted with buffer A containing 0.4 M NaCl and applied to a HisTrap HP column (GE Healthcare), previously equilibrated with 20 mM Tris-HCl buffer (pH 7.5), 0.5 M NaCl (buffer B). After the wash with buffer B containing 30 mM imidazole, the bound RNase H2 was eluted with buffer B containing 30 mM imidazole and applied to PD-10 column (GE Healthcare) previously equilibrated with buffer A. Purified enzyme solution was stored at -80°C before use. The enzyme concentration was determined using the molar absorption coefficient at 280 nm of 83,030 M^{-1} cm^{-1}.

Circular dichroism measurement – A Jasco J-820 (Tokyo, Japan) spectropolarimeter equipped with a Peltier system of cell temperature control was used. The spectrometer conditions were: spectral range 210–250 nm; 100 mdeg sensitivity; 0.1 nm resolutions; 4 s response time; 20 nm min^{-1} scan rate and 5 accumulations. The control baseline was obtained with solvent and all the components without RNase H2. Circular dichroism (CD) spectra were recorded at 25°C using 2-mm cell. The concentration of RNase H2 was 1.0 μM in 5 mM Tris-HCl buffer (pH 8.3), 20 mM KCl, 5% glycerol. CD spectra were processed with a Jasco software and finally expressed in mean-residue molar ellipticity units, [θ] (deg cm^2 $dmol^{-1}$).

Gel filtration chromatography – Human RNase H2 [0.1 ml of 1.7 μM in 20 mM Tris-HCl buffer (pH 7.5)] was applied onto a COSMOSIL Packed Column 5Diol–300–II (7.5 mm inner diameter x 600 mm) (Nacalai Tesque) pre-equilibrated with 20 mM Tris-HCl buffer (pH 7.5), 0.5 M L-Arg at a flow-rate of 1.0 ml/min and detected by absorbance at 280 nm (A_{280}).

RNase H2 assay – An RNA_{18}/DNA_{18} hybrid (named R18/D18) was prepared by incubating 1.0 µl of 100 µM 3'FITC-labeled 18-mer RNA 5'-gaucugagccugggagcu-FITC-3' (R18) and 1.2 µl of 100 µM 5'Dabcyl-labeled 18-mer DNA 5'-Dabcyl-AGCTCCCAGGCTCAGTC-3' (D18) in 50 mM Tris-HCl buffer (pH 8.0) containing 60 mM KCl at 25°C for 30 min. A hybrid consisting of DNA_{14}-RNA_1-DNA_3/DNA_{18} (named R1/D18) was prepared as described above by using 3'FITC-labeled 5'-GATCTGAGCCTGGGaGCT-FITC-3' (R1) instead of R18.

Enzyme reaction was started by adding 20 µl of 0.33 or 3 nM RNase H2 to the 180 µl of the mixture containing 2.8 or 5.6 nM substrate (R18/D18 or R1/D18) in a 96-well plate. The reaction buffers were 50 mM Tris-HCl buffer at pH 7.0–8.8 or 50 mM AMPSO–NaOH buffer at pH 8.6–10.4, each containing 5 mM $MgCl_2$. The reaction was carried out at 25, 30, or 35°C, each with the initial enzyme and R1/D18 concentrations of 33 or 300 pM and 2.5 or 5.0 nM, respectively. The reaction was monitored by following the increase in fluorescence intensity at 515 nm with excitation at 490 nm with an Ensight (PerkinElmer, Waltham, MA) every 20 s for 10 min.

The Michaelis-Menten equation was expressed as $v_0 = (k_{cat}/K_m)[E]_o[S]_o$, where v_o, k_{cat}, $[E]_o$ and $[S]_o$ are the initial reaction rate, the molecular activity, the initial enzyme concentration, and the initial substrate concentration, respectively. The proton dissociation constants (K_{e1} and K_{e2}) for the bell-shaped pH-dependence of the activity (k_{cat}/K_m) were calculated from Eqs. 1 and 2 by a non-linear least squares regression method with Kaleida Graph Version 3.5 (Synergy Software, Essex, VT):

$$(k_{cat}/K_m)_{obs} = (k_{cat}/K_m)_o / \{1+([H]/K_{e1})+(K_{e2}/[H])\} \quad (1)$$

$$(k_{cat}/K_m)_{obs} = (k_{cat}/K_m)_o / \{1+([H]^2/K_{e1}^2)+([H]/K_{e1})+(K_{e2}/[H])\} \quad (2)$$

In this equation, $(k_{cat}/K_m)_o$, $(k_{cat}/K_m)_{obs}$, and [H] are the intrinsic k_{cat}/K_m value, the k_{cat}/K_m value observed, and the proton concentration, respectively, at a specified pH.

Irreversible thermal inactivation of human RNase H2 – Human RNase H2 (330 pM) was incubated at 30, 35, and 40°C in 20 mM Tris-HCl buffer (pH 7.5) containing various salts for specified durations followed by the incubation on ice for 5 min. The remaining activity was determined at 25°C as described above.

Assuming that the thermal inactivation reaction of human RNase H2 is irreversible and consists of only one step, the first-order rate constant, k_{obs}, of the thermal inactivation was evaluated by plotting logarithmic values of the residual activity against the time of heat treatment according to Eq. 3, as described previously (16, 17).

$$\ln B = A - k_{obs}\, t \quad (3)$$

where A is the constant term, and B is the relative activity (%) defined as the ratio of the initial reaction rate at a time for the thermal incubation (=t) to that without the incubation.

Thermodynamic analysis – The enthalpy change, $\Delta H°$, of deprotonation was determined from a van't Hoff plot according to Eq. 4, as described previously (18). The activation energy, E_a, for the thermal inactivation was determined from am Arrhenius plot according to Eq. 5, as described previously (16, 17).

$$\ln(K_e) = A - (\Delta H°/R)(1/T) \quad (4)$$

$$\ln(k_{obs}) = A - (E_a/R)(1/T) \quad (5)$$

where A, R and T are the constant term, the gas constant (= 8.314 J K^{-1} mol^{-1}), and absolute temperature in degrees Kelvin, respectively.

The Gibbs free energy change of activation, $\Delta G^{‡}$, the enthalpy change of activation, $\Delta H^{‡}$, and the entropy change of activation, $\Delta S^{‡}$, for the thermal inactivation at certain temperature were determined according to Eq. 6, 7, and 8, respectively.

$$\Delta G^{‡} = - RT\,[\ln(k_{obs}) - \ln(RT/Nh)] \quad (6)$$

$$\Delta H^{‡} = E_a - RT \quad (7)$$

$$\Delta S^{‡} = (\Delta H^{‡} - \Delta G^{‡})/T \quad (8)$$

where N and h are Avogadro number (= 6.022×10^{23} mol^{-1}) and Plank constant (= 6.626×10^{-34} J s), respectively.

Results and Discussion

Production of recombinant human RNase H2 – Human RNase H2 is composed of three different subunits (A, B, and C) (Figs. 1 and 2). The human RNase H2 expression plasmid pET15b-hH2ABC (Fig. 3) has a T7 promoter sequence followed by genes for A, B, and C, each containing $(His)_6$ tag at its N-terminus (19). These three subunits were co-expressed in the *E. coli* BL21(DE3) cells transformed with pET15b-hH2ABC. The

active enzyme was purified from the soluble fractions of the cells with heparin affinity chromatography as the first step and Ni^{2+} affinity column chromatography as the second step. It is noted that human RNase H2 was eluted at relatively low imidazole concentration (30 mM). Figure 4 shows the results of SDS-PAGE analysis of the active fractions at each purification stage and the purified enzyme preparations. The purified preparation yielded three bands corresponding to A, B, and C. Figures 5 and 6 show the elution pattern of gel filtration chromatography (GFC) and circular dichroism (CD) spectrum, respectively, of the purified enzyme preparation. Human RNase H2 was eluted at the position corresponding to molecular mass of 120 kDa (Fig. 5A). On SDS-PAGE, the peak fractions showed three bands with the same intensity, indicating that the purified enzyme preparation consists of each one molecule of A, B, and C (Fig. 5D). The molecular mass of the heterotrimeric complex is calculated to be 88 kDa based on the amino acid sequence, and the difference from the value estimated from GFC analysis (120 kDa) might be derived from the unique character of human RNase H2. On CD spectroscopy, the purified enzyme preparation exhibited negative ellipticities at around 200–250 nm with minimum values around 208 nm (Fig. 6).

Effects of salts on the human RNase H2 activity – To analyze the effects of various neutral salts on the human RNase H2 activity, we performed fluorescence-based RNase H2 assay. An RNA_{18}/DNA_{18} hybrid (R18/D18) (Fig. 7A) and a hybrid consisting of DNA_{14}-RNA_1-DNA_3 and DNA_{18} (R1/D18) (Fig. 8A) were used as the substrate. R18/D18 is designed to emit fluorescence when RNA_{18} is cleaved at a site close to the 3' end, and the fluorescein-labeled RNA fragment dissociates from the complementary DNA strand. R1/D18 is designed to emit fluorescence when DNA_{14}-RNA_1-DNA_3 is

cleaved at the 5'-end of the RNA_1.

In the reaction with R18/D18, the relative activity of human RNase H2, which is defined as the ratio of the activity in the presence of salt to that in the absence, increased with increasing concentrations of NaCl, KCl, RbCl, or NaBr, reached the highest (180–390%) at 30–60 mM, and decreased (Fig. 7B). As is the case with R1/D18, the relative activity increased with increasing concentrations of NaCl, KCl, RbCl, or NaBr, reached the highest (170–250%) at 10–30 mM, and decreased (Fig. 8B). It is noted that the result with NaCl is in good agreement with those reported previously (20). In contrast, the relative activity decreased with increasing concentrations of LiCl, LiBr, or CsCl. The IC_{50} values of LiCl, LiBr, and CsCl in the reaction with R18/D18 were 32, 43, and 26 mM, respectively (Fig. 7C), and those in the reaction with R1/D18 were 51, 48, and 40 mM, respectively (Fig. 8C). These results suggest that species of cation, rather than anion, might be responsible for the effect on activity.

The feature of the activation of human RNase H2 by NaCl, KCl, RbCl, and NaBr is that the 1.7–3.9 fold activation was observed at very low salt concentration (10–60 mM) (Figs. 7B and 8B). Similar to *Thermotoga maritima* type 2 RNase H (RNase HII), the 3-fold activation was observed at 50 mM NaCl (4). In the following, we discuss the differences between the activation of human RNase H2 and those of a typical halophilic enzyme, *Halobacterium* sp. NRC-1 RNase H1 (Halo-RNase H1) (21) and *Bacillus thermoproteolyticus* zinc metalloproteinase themolysin (22). The Halo-RNase H1 activity requires the presence of 2 M NaCl, which was thought to result from the salt-mediated unfavorable suppression of negative charge repulsion at the molecular surface including the active site (21). The thermolysin activity increased in an exponential fashion with increasing concentration of NaCl and reached 1,300–1,500%

at 4 M, which was thought to result from the interaction between respective ions and particular residues and/or the salt-mediated suppression of unfavorable charge repulsion (22). It is noted that there is almost no activation at 50 mM NaCl in Halo-RNase H1 or thermolysin, much different from the case with human RNase H2.

Shaban et al (23) reported the crystal structure of mouse RNase H2. They created a model for the complex of mouse RNase H2 and the RNA/DNA hybrid using the crystal structure of the complex of *Bacillus halodurans* RNase H1 and the RNA/DNA hybrid as a starting model and showed that unlike the case with *B. halodurans* RNase H1, the RNA/DNA hybrid makes significant clash with mouse RNase H2 subunit A (23). In this study, the optimum concentrations of NaCl, KCl, RbCl, and NaBr were different according to the substrate (60, 60, 30, and 40 mM, respectively, for R18/D18 (Fig. 7B) and 20, 30, 20, and 20 mM, respectively, for R1/D18 (Fig. 8B)). These evidences suggest that the salt-based activation of human RNase H2 results from the interaction between respective ions and particular residues as well as that between respective ions and the RNA/DNA hybrid.

NaCl, KCl, RbCl, and NaBr inhibited the human RNase H2 activity at 50−200 mM (Figs. 7B and 8B), and LiCl, LiBr, and CsCl inhibited it at 0−200 mM (Figs. 7C and 8C). The inhibition by NaCl and LiCl was reported in TREX1 (24). TREX1 is a 3’→5’ exonuclease in mammalian cells. Like RNases H, TREX1 has a DEDD motif and two divalent metal ions catalytic system. In addition, decrease in TREX1 activity by the mutation of its gene causes AGS (8). Brucet et al (24) proposed that, based on the crystal structure of the complex of TREX1 and a nucleotide, LiCl and NaCl inhibited the TREX1 activity by competing with the divalent cations for the binding at the active site. Similar inhibition of enzyme activity by LiCl was reported in inositol

monophosphate (25). If such mechanism can be applied to human RNase H2, our results suggest that Na^+, K^+, and Rb^+ exhibit weak inhibition because they have low binding ability with the active site, while Li^+ and Cs^+ exhibit strong inhibition because they have high binding ability with the active site.

Effects of salts on the human RNase H2 stability – To analyze the effect of NaCl on the human RNase H2 stability, we incubated human RNase H2 at 30, 35, or 40°C for specified durations and measured the remaining activity by the assay using R18/D18. The natural logarithm of the relative activity (%) plotted against the incubation time gave linear relationships at all temperatures (Fig. 9A−C), indicating that the inactivation followed first-order kinetics. The first-order rate constant (k_{obs}) values at 30, 35, and 40°C in the presence of 10 mM NaCl were 7.1×10^{-4}, 1.7×10^{-3}, and 4.7×10^{-3} s^{-1}, respectively, and those in the absence were 7.7×10^{-4}, 2.7×10^{-3}, and 7.0×10^{-3} s^{-1}, respectively, indicating that 10 mM NaCl stabilized human RNase H2. Figure 9D show an Arrhenius plot. The natural logarithm of k_{obs} against $1/T$ showed a linear relationship, and the activation energies (E_a) of thermal inactivation were calculated from the slope to be 149 ± 5 kJ mol^{-1} for the presence of 10 mM NaCl and 175 ± 13 kJ mol^{-1} for the absence.

To analyze the effects of NaCl and KCl concentrations on the human RNase H2 stability, we incubated human RNase H2 at 37°C for 10 min in the presence of 0−200 mM NaCl or KCl, and measured the remaining activity by the assay using R18/D18. The k_{obs} values decreased with increasing NaCl or KCl concentrations and reached 40% at 80 mM NaCl or 52% at 60 mM KCl (Fig. 10A). The half-life ($t_{1/2}$) at 37°C was 3.8 min in the absence of salt. It increased with increasing NaCl or KCl concentrations and

reached 9.5 min at 80 mM NaCl or 7.3 min at 60 mM KCl (Fig. 10B).

To analyze the inactivation mechanism, we incubated human RNase H2 with or without 10 mM NaCl at 40°C for 3 min and measured their elution patters in GFC and their CD spectra. There is little difference in the elution patterns of human RNases H2 before and after the incubation at 40°C (Fig. 5A–C). On the other hand, the $[\theta]_{208}$ and $[\theta]_{222}$ values of human RNase H2 were in the order of before the incubation < after the incubation with 10 mM NaCl < after the incubation without NaCl (Fig. 6). These results suggest that the inactivation results from the denaturation rather than the dissociation of the heterotrimeric complex and that NaCl stabilizes human RNase H2 by suppressing the denaturation.

Based on the results of thermal inactivation (Fig. 9) and according to Eqs. 5−8, E_a, the Gibbs free energy change of activation ($\Delta G^{\ddagger}$), the enthalpy change of activation ($\Delta H^{\ddagger}$), and the entropy change of activation ($\Delta S^{\ddagger}$) for thermal inactivation were 175 kJ mol^{-1}, 92 kJ mol^{-1}, 172 kJ mol^{-1}, and 265 J mol^{-1} K^{-1}, respectively, in the absence of NaCl and were 149 kJ mol^{-1}, 93 kJ mol^{-1}, 146 kJ mol^{-1}, and 178 J mol^{-1} K^{-1}, respectively, in the presence of 10 mM NaCl. This indicates that the presence of 10 mM NaCl decreased $\Delta H^{\circ\ddagger}$ and $\Delta S^{\circ\ddagger}$, suggesting that the enhanced thermal stability by salt was due to the decrease in $\Delta S^{\circ\ddagger}$.

The highest stabilization of human RNase H2 was observed at 80 mM NaCl or 60 mM KCl (Fig. 10), which is similar concentration to the case with the activation (Figs. 7B and 8B). This suggests that the mechanism of stabilization by salts is similar to that of activation. On the other hand, human RNase H2 almost lacked activity at 200 mM NaCl or KCl (Figs. 7B and 8B), while it exhibited activity after incubation at 37°C for 10 min at 200 mM NaCl or KCl (Fig. 10B). This suggests that the binding of NaCl and

KCl to the active site inhibits activity, but is reversible.

Effects of pH on the RNase H2 activity – To analyze the effects of pH on the RNase H2 activity, we measured the activity at pH 7.0–10.4 at 25, 30, and 35°C by the assay using R1/D18. The k_{cat}/K_m values plotted against pH showed a narrow bell-shaped profiles, which is in good agreement with those reported previously (20). First we applied the results to the reaction scheme with two ionizable groups (Fig. 11A), which is generally used for the analysis of pH-dependence of enzyme activity. The $(k_{cat}/K_m)_o$ value and the pK_{e1} and pK_{e2} values were calculated according to Eq. 1. However, the curve expressed by Eq. 1, did not fit the data points (Fig. 11B), indicating that this scheme was not applicable. Assuming that the steep increase in $(k_{cat}/K_m)_{obs}$ at pH 7.0−8.0 results from the presence of two ionizable groups with the same pK_a values, we applied the results to the reaction scheme with three ionizable groups, in which only the EHS complex gives products (Fig. 12A). The $(k_{cat}/K_m)_o$ value and the pK_{e1} and pK_{e2} values were calculated according to Eq. 2. The curve expressed by Eq. 2 fit the data points well (Fig. 12B), indicating that this scheme was applicable. Figure 12C shows a van't Hoff plot. Enthalpy changes (ΔH^o) of deprotonation were 5 ± 21 kJ mol^{-1} for pK_{e1} and 68 ± 25 kJ mol^{-1} for pK_{e2}.

DEDD and DSK motifs are conserved in RNase H2. Shaban et al (23) showed that, based on the crystal structure of mouse RNase H2, Asp34, Glu35, Asp142, and Asp170 likely coordinates two divalent metal ions. Rychlik et al (4) showed that, based on the crystal structure of the complex of a single peptide *T. maritima* RNase HII with a nucleic acid, Asp18, Glu19, and Asp107 of DEDD motif coordinate metal ions, while Asp124 of DEDD motif does not. Consistent with that, the mutation of counterparts of

Asp18, Glu19, or Asp107 abolished the activities of RNases HII from *Archaeoglobus fulgidus* and *Thermococcus kodakaraensis*, while the mutation of Asp124 did not (26, 27). Rychlik et al (4) also showed that Lys47 of DSK motif interacts with the scissile phosphate. Based on the crystal and modelled structural analysis of the complex of human RNase H2 with a nucleic acid and the mutational analysis, Figiel et al (28) showed the followings: (i) Like *T. maritima* RNase HII, Asp34, Glu35, and Asp141 of DEDD motif coordinates metal ions, while Asp169 of DEDD motif does not; (ii) the DSK motif-containing loop is located close to the active site and is flexible in the absence of substrate; and (iii) the mutation of Lys69 of the DSK motif abolished activity. In Fig. 12A, "EH" is the free enzyme that can bind the substrate and give the product. These results suggest that the "EH" corresponds to the human RNase H2 in which Asp34, Glu35, and Asp141 are deprotonated and Lys69 are protonated. They also suggested that at least one residue out of Asp34, Glu35, and Asp141 has an ionizable group involved in the catalytic mechanism responsible for acidic pK_e (pK_{e1}) and Lys69 is that for alkaline pK_e (pK_{e2}).

pK_e values are commonly used for the estimation of ionizable groups involved in the catalytic mechanism. In this study, we used not only pK_e but also ΔH^o of deprotonation for the estimation for the following two reasons: (i) pK_a of active-site residues sometimes varies considerably depending on the microenvironment. For example, the pK_a values of the active-site glutamate were 8.4 in xylanase (29) and 7.0 in carboxypeptidase A (30); (ii) each amino acid has its own ΔH^o values of side chain, and such ΔH^o values of amino acid residues in protein are little affected by the microenvironment and are almost equal to those of free amino acids (18, 31). Activity at 25–35°C exhibited a narrow bell-shaped pH-dependence with the acidic and alkaline

pK_e (pK_{e1} and pK_{e2}) values of 7.3−7.6 and 8.1−8.8, respectively (Fig. 12B), which is similar to those of RNases HII from *E. coli* (32) and *T. maritima* (27).

In this study, the conventional reaction scheme with two ionizable groups (each at acidic and alkaline side) involved in enzyme activity was not applicable to pH dependence of human RNase H2 activity (Fig. 11). On the other hand, the one with three ionizable groups (two at acidic side and one at alkaline side) was applicable (Fig. 12). In this scheme, pK_{e1} and pK_{e2} values were calculated 7.3−7.6 and 8.1−8.8, respectively, and ΔH^o of deprotonation were calculated 5 ± 21 kJ mol^{-1} for pK_{e1} and 68 ± 25 kJ mol^{-1} for pK_{e2} (Fig. 12). It should be noted that the ΔH^o of deprotonation for pK_{e1} (5 ± 21 kJ mol^{-1}) is similar to that of the side chains of L-Asp (−6 to 6 kJ mol^{-1}) (31), suggesting that the ionizable groups responsible for pK_{e1} are two residues out of Asp34, Glu35, and Asp141 of DEDD motif. We speculate that the difference between the pK_{e1} of human RNase H2 (7.3−7.6) and the pK_a of the side chain of Asp in protein (around 3−5) might be due to the microenvironment in the active site, as discussed above. On the other hand, the pK_{e2} value of human RNase H2 (8.1−8.8) is similar to the pK_a of Lys in protein (around 8−10), and the ΔH^o of deprotonation for pK_{e2} of human RNase H2 (68 ± 25 kJ mol^{-1}) was similar to the ΔH^o of the side chain of Lys (70.4 ± 4.4 kJ mol^{-1}) (48). This suggests that the ionizable group responsible for pK_{e2} is Lys69.

Conclusion – The activity and stability of human RNase H2 are highly affected by salts and pH. Further study is required to explore the mechanisms of the activation and stabilization of human RNase H2 by salts and to assign its ionizable residues controlling the activity. On the other hand, the results presented in this study might be useful to establish the reaction condition in the screening of activators and inhibitors of human

RNase H2.

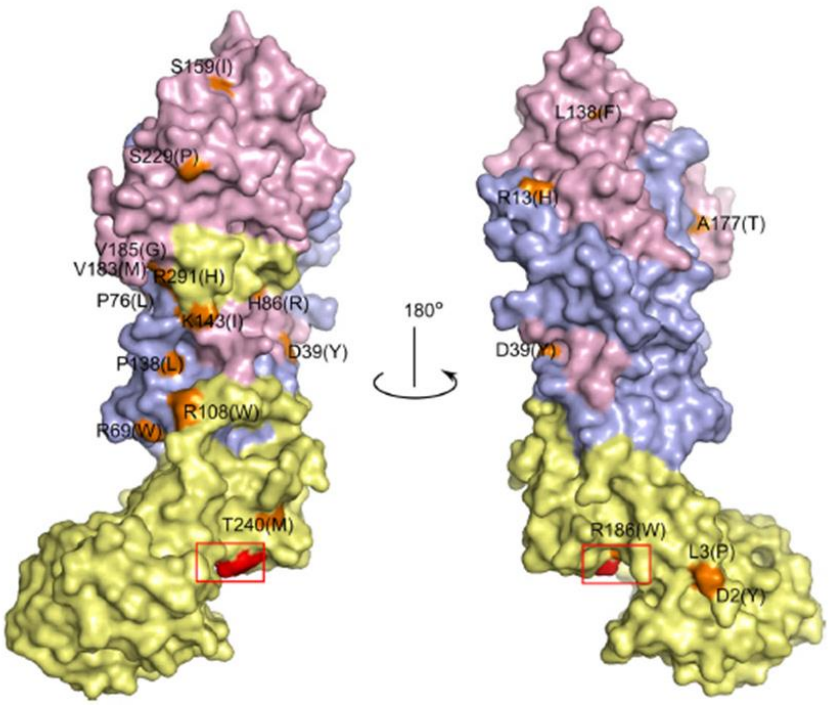

Fig. 1. Overall structure of human RNase H2. Human RNase H2 consists of A (33 kDa), B (35 kDa), and C (18 kDa) subunits. The active site is present at the A subunit.

Human RNase H2 A subunit

```
   1 ATGGATCTCAGCGAGCTGGAGAGAGACAATACAGGCCGCTGTCGCCTGAGTTCGCCTGTG
   1  M  D  L  S  E  L  E  R  D  N  T  G  R  C  R  L  S  S  P  V
  61 CCCGCGGTGTGCCGCAAGGAGCCTTGCGTCCTGGGCGTCGATGAGGCGGGCAGGGGCCCC
  21  P  A  V  C  R  K  E  P  C  V  L  G  V  D  E  A  G  R  G  P
 121 GTGCTGGGCCCCATGGTCTACGCCATCTGTTATTGTCCCCTGCCTCGCCTGGCAGATCTG
  41  V  L  G  P  M  V  Y  A  I  C  Y  C  P  L  P  R  L  A  D  L
 181 GAGGCGCTGAAAGTGGCAGACTCAAAGACCCTATTGGAGAGCGAGCGGGAAAGGCTGTTT
  61  E  A  L  K  V  A  D  S  K  T  L  L  E  S  E  R  E  R  L  F
 241 GCGAAAATGGAGGACACGGACTTTGTCGGCTGGGCGCTGGATGTGCTGTCTCCAAACCTC
  81  A  K  M  E  D  T  D  F  V  G  W  A  L  D  V  L  S  P  N  L
 301 ATCTCTACCAGCATGCTTGGGCGGGTCAAATACAACCTGAACTCCCTGTCACATGATACA
 101  I  S  T  S  M  L  G  R  V  K  Y  N  L  N  S  L  S  H  D  T
 361 GCCACTGGGCTTATACAGTATGCATTGGACCAGGGCGTGAACGTCACCCAGGTATTCGTG
 121  A  T  G  L  I  Q  Y  A  L  D  Q  G  V  N  V  T  Q  V  F  V
 421 GACACCGTAGGGATGCCAGAGACATACCAGGCGCGGCTGCAGCAAAGTTTTCCCGGGATT
 141  D  T  V  G  M  P  E  T  Y  Q  A  R  L  Q  Q  S  F  P  G  I
 481 GAGGTGACGGTCAAGGCCAAAGCAGATGCCCTCTACCCGGTGGTTAGTGCTGCCAGCATC
 161  E  V  T  V  K  A  K  A  D  A  L  Y  P  V  V  S  A  A  S  I
 541 TGTGCCAAGGTGGCCCGGGACCAGGCCGTGAAGAAATGGCAGTTCGTGGAGAAACTGCAG
 181  C  A  K  V  A  R  D  Q  A  V  K  K  W  Q  F  V  E  K  L  Q
 601 GACTTGGATACTGATTATGGCTCAGGCTACCCCAATGATCCCAAGACAAAAGCGTGGTTG
 201  D  L  D  T  D  Y  G  S  G  Y  P  N  D  P  K  T  K  A  W  L
 661 AAGGAGCACGTGGAGCCTGTGTTCGGCTTCCCCCAGTTTGTCCGGTTCAGCTGGCGCACG
 221  K  E  H  V  E  P  V  F  G  F  P  Q  F  V  R  F  S  W  R  T
 721 GCCCAGACCATCCTGGAGAAAGAGGCGGAAGATGTTATATGGGAGGACTCAGCATCCGAG
 241  A  Q  T  I  L  E  K  E  A  E  D  V  I  W  E  D  S  A  S  E
 781 AATCAGGAGGGACTCAGGAAGATCACATCCTACTTCCTCAATGAAGGGTCCCAAGCCCGT
 261  N  Q  E  G  L  R  K  I  T  S  Y  F  L  N  E  G  S  Q  A  R
 841 CCCCGTTCTTCCCACCGATATTTCCTGGAACGCGGCCTGGAGTCAGCAACCAGCCTCTAG
 281  P  R  S  S  H  R  Y  F  L  E  R  G  L  E  S  A  T  S  L  *
```

Fig. 2. Nucleotide and amino acid sequences of human RNase H2.

Human RNase H2 B subunit

```
   1 atggccgctggcgtggactgcggggacggggttggcgcccggcagcacgtgttcctggtt
   1  M  A  A  G  V  D  C  G  D  G  V  G  A  R  Q  H  V  F  L  V
  61 tcagaatatttaaaagatgcttcaaagaagatgaaaaatgggctaatgtttgtaaaactg
  21  S  E  Y  L  K  D  A  S  K  K  M  K  N  G  L  M  F  V  K  L
 121 gttaacccctgttcaggagaaggagccatttacttgttcaatatgtgtctacagcagctg
  41  V  N  P  C  S  G  E  G  A  I  Y  L  F  N  M  C  L  Q  Q  L
 181 tttgaagtaaaagttttcaaggaaaaacaccattcttggtttataaatcaatcagttcaa
  61  F  E  V  K  V  F  K  E  K  H  H  S  W  F  I  N  Q  S  V  Q
 241 tcaggaggtcttctccattttgccacacctgtggatcctctatttctgcttctccactac
  81  S  G  G  L  L  H  F  A  T  P  V  D  P  L  F  L  L  L  H  Y
 301 ctcataaaggctgataaggaggggaagtttcagccccttgatcaagttgtggtggataac
 101  L  I  K  A  D  K  E  G  K  F  Q  P  L  D  Q  V  V  V  D  N
 361 gtgtttccaaattgcatcttgttgctgaaacttcctggacttgagaagttacttcatcat
 121  V  F  P  N  C  I  L  L  L  K  L  P  G  L  E  K  L  L  H  H
 421 gtgacagaggaaaaaggtaatccagaaatagacaacaagaaatattacaagtacagcaaa
 141  V  T  E  E  K  G  N  P  E  I  D  N  K  K  Y  Y  K  Y  S  K
 481 gagaagacattaaagtggctggaaaaaaaggttaatcaaactgtggcagcattaaaaacc
 161  E  K  T  L  K  W  L  E  K  K  V  N  Q  T  V  A  A  L  K  T
 541 aataatgtgaatgtcagttcccgggtacagtcaactgcatttttctctggtgaccaagct
 181  N  N  V  N  V  S  S  R  V  Q  S  T  A  F  F  S  G  D  Q  A
 601 tccactgacaaggaagaggattatattcgttatgcccatggtctgatatctgactacatc
 201  S  T  D  K  E  E  D  Y  I  R  Y  A  H  G  L  I  S  D  Y  I
 661 cctaaagaattaagtgatgacttatctaaatacttaaagcttccagaaccttcagcctca
 221  P  K  E  L  S  D  D  L  S  K  Y  L  K  L  P  E  P  S  A  S
 721 ttgccaaatcctccatcaaagaaaataaagttatcagatgagcctgtagaagcaaaagaa
 241  L  P  N  P  P  S  K  K  I  K  L  S  D  E  P  V  E  A  K  E
 781 gattacactaagtttaatactaaagatttgaagactgaaaagaaaaatagcaaaatgact
 261  D  Y  T  K  F  N  T  K  D  L  K  T  E  K  K  N  S  K  M  T
 841 gcagctcagaaggctttggctaaagttgacaagagtggaatgaaaagtattgataccttt
 281  A  A  Q  K  A  L  A  K  V  D  K  S  G  M  K  S  I  D  T  F
 901 tttggggtaaaaaataaaaaaaaaattggaaaggtttga
 301  F  G  V  K  N  K  K  K  I  G  K  V  *
```

Fig. 2. Nucleotide and amino acid sequences of human RNase H2 (continued).

Human RNase H2 C subunit

```
   1 atggagagcggcgacgaagcggccatcgagaggcaccgcgtccacttgcgctccgccaca
   1  M  E  S  G  D  E  A  A  I  E  R  H  R  V  H  L  R  S  A  T
  61 ttgcgcgacgccgtacccgccacactgcatctgctgccctgcgaggttgcggtggacggg
  21  L  R  D  A  V  P  A  T  L  H  L  L  P  C  E  V  A  V  D  G
 121 cccgccccggtggggcgcttcttcacgcccgccatccgccagggccccgagggactcgaa
  41  P  A  P  V  G  R  F  F  T  P  A  I  R  Q  G  P  E  G  L  E
 181 gtgtcgtttcggggccgctgtctacggggagaggaggtggcggtgccgcctggcctcgtg
  61  V  S  F  R  G  R  C  L  R  G  E  E  V  A  V  P  P  G  L  V
 241 ggatacgtgatggtgacagaagagaagaaggtgtcgatggggaagccagacccttgcgg
  81  G  Y  V  M  V  T  E  E  K  K  V  S  M  G  K  P  D  P  L  R
 301 gattccgggactgacgaccaagaggaggagccgctggagcgggacttcgaccgcttcatt
 101  D  S  G  T  D  D  Q  E  E  E  P  L  E  R  D  F  D  R  F  I
 361 ggagccactgccaacttcagccgcttcaccctgtggggtctggagaccatccctggcccg
 121  G  A  T  A  N  F  S  R  F  T  L  W  G  L  E  T  I  P  G  P
 421 gatgccaaagtgcgtggggccttaacttggcccagccttgcggcagcgattcacgcacag
 141  D  A  K  V  R  G  A  L  T  W  P  S  L  A  A  A  I  H  A  Q
 481 gtgcccgaggactga
 161  V  P  E  D  *
```

Fig. 2. Nucleotide and amino acid sequences of human RNase H2 (continued).

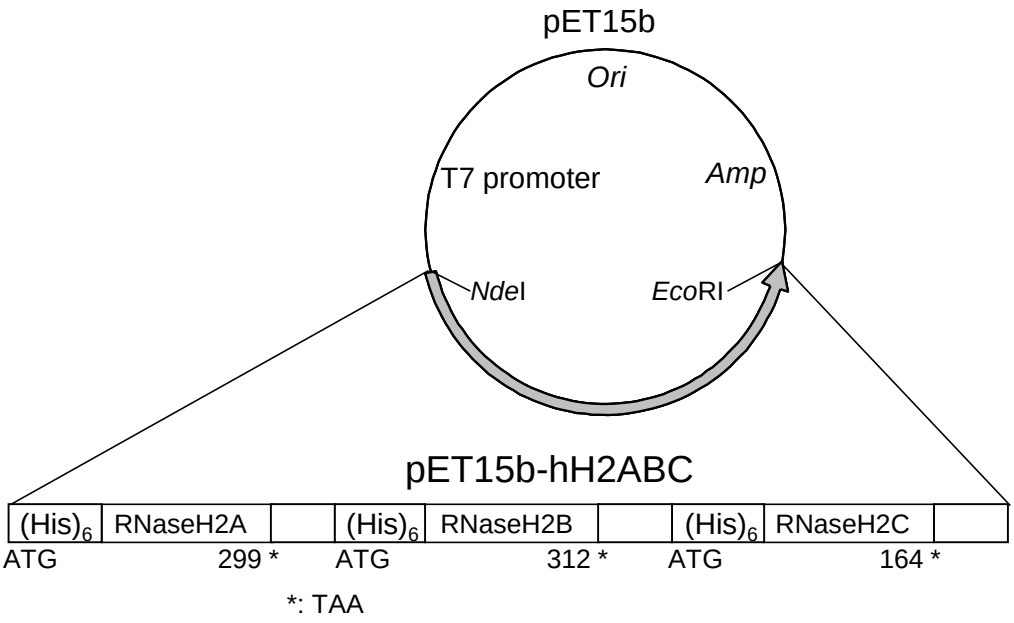

Fig. 3. Expression plasmid for human RNase H2. The asterisk indicates the termination codon.

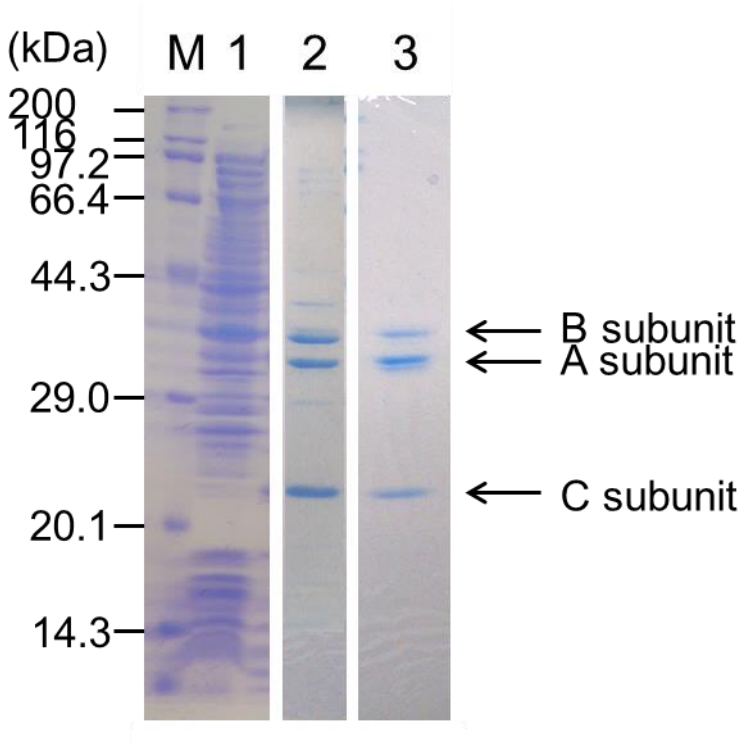

Fig. 4. SDS-PAGE under reducing conditions. Coomassie Brilliant Blue-stained 12.5% SDS-polyacrylamide gel showing marker proteins (lane M), soluble fractions of the total extracts (lane 1), active fractions of heparin affinity chromatography (lane 2), and active fractions of Ni^{2+} affinity chromatography, which was purified enzyme preparations of human RNase H2 (lane 3). A, B, and C subunits of human RNase H2 are indicated by arrows.

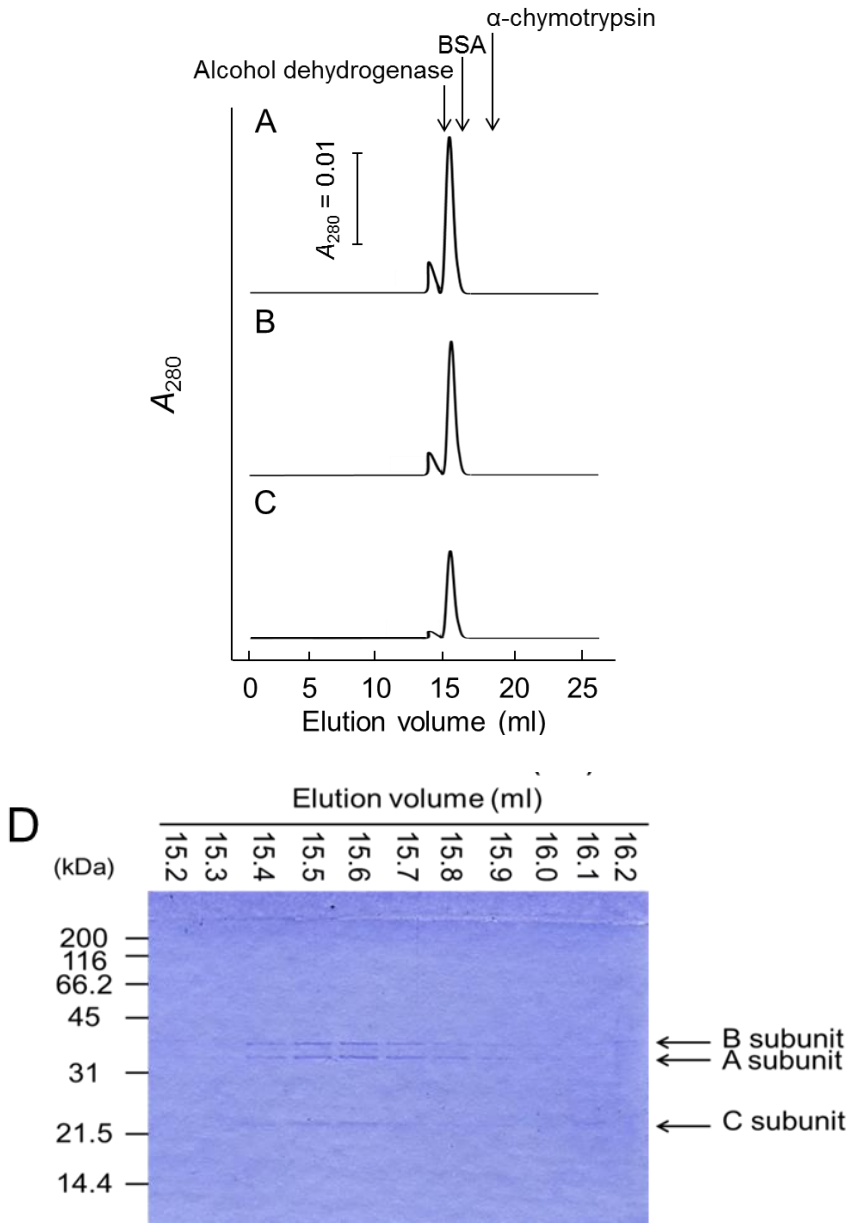

Fig. 5. Elution pattern of gel filtration column chromatography of human RNase H2. Human RNases H2 (0.1 ml of 1.7 μM in 20 mM Tris-HCl buffer (pH 7.5)) before (A) or after thermal treatment at 0 (B) or 10 mM (C) NaCl at 40ºC for 3 min were applied onto a COSMOSIL Packed Column 5Diol–300–II (7.5 mm inner diameter x 600 mm) (Nacalai Tesque) equilibrated with 20 mM Tris-HCl buffer (pH 7.5), 0.5 M L-Arg at a flow-rate of 1.0 ml/min. The elution volume of alcohol dehydrogenase (150 kDa), BSA (bovine serum albumin, 66 kDa), and α-chymotrypsin (25 kDa) is indicated by an arrow. (D) SDS-PAGE analysis of the fractions in Fig. 5A. Coomassie Brilliant Blue-stained 12.5% SDS-polyacrylamide gel with the fractions with their elution volume on top is shown.

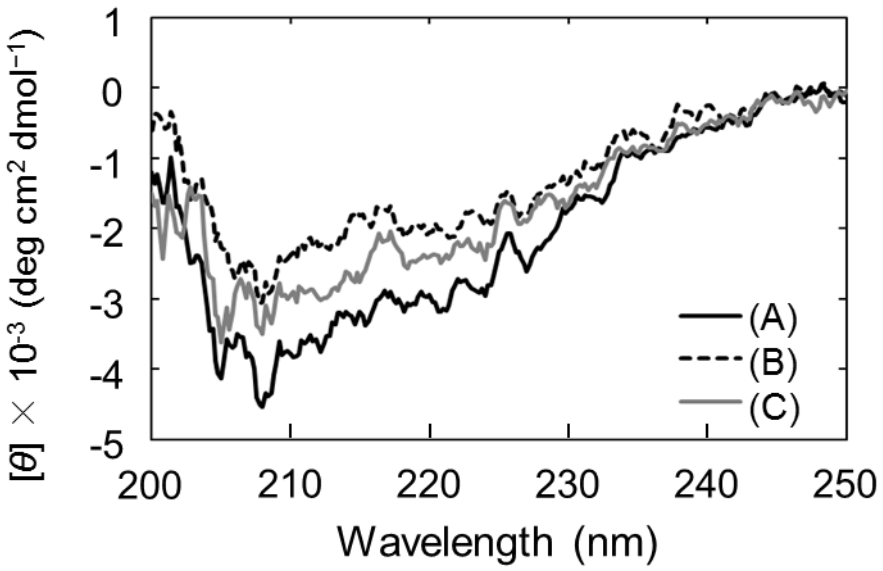

Fig. 6. CD spectra of human RNase H2. CD spectra of human RNase H2 (0.4 ml of 0.5 μM in 20 mM Tris-HCl buffer (pH 7.5)) before (A) or after thermal treatment at 0 (B) or 10 (C) mM NaCl at 40ºC for 3 min were determined with a 2-mm cell using a J-820 spectropolarimeter (Jasco) under the following condition: spectral range 200–250 nm; 25ºC; 100 mdeg sensitivity; 0.2 nm resolutions; 4 s response time; 20 nm min^{-1} scan rate; and 4 accumulations. CD spectra were processed with a Jasco software, and finally expressed in mean-residue molar ellipticity units, [θ] (deg cm^2 $dmol^{-1}$).

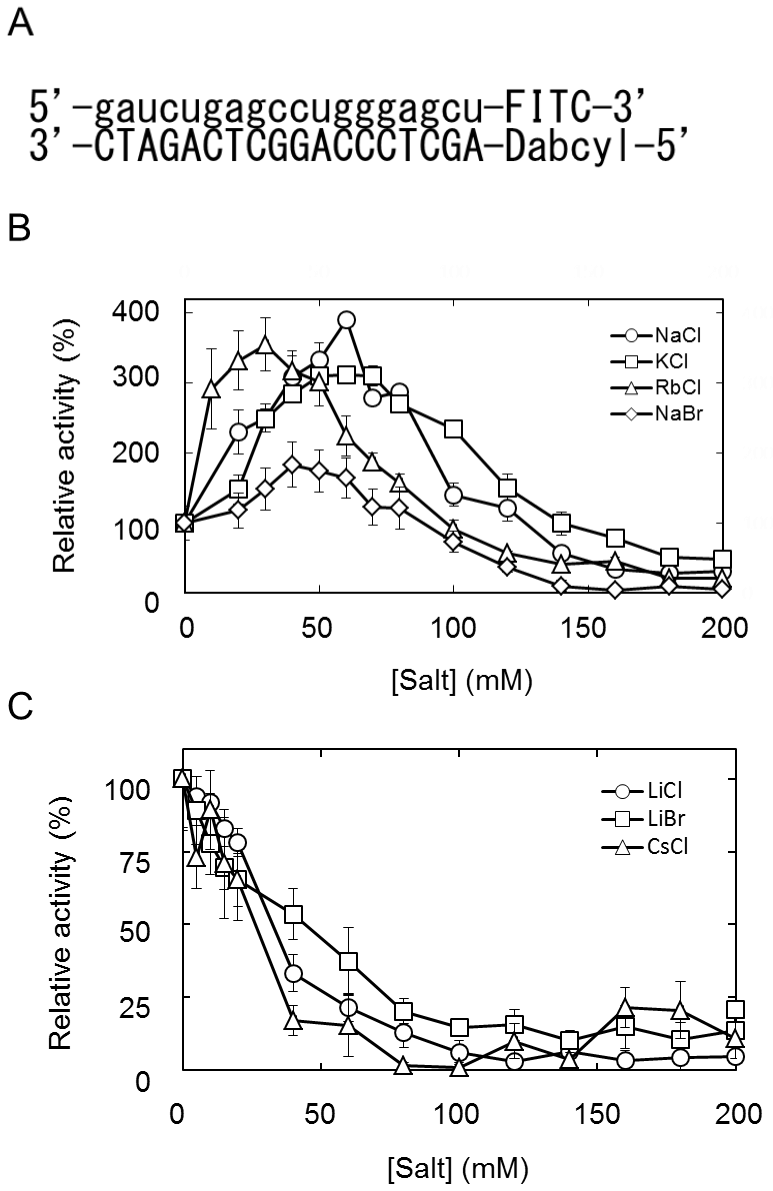

Fig. 7. Effects of salts on the human RNase H2 activity to cleave the RNA_{18} strand. (A) Sequences of the RNA-DNA hybrid substrate R18/D18. (B, C) Activity *vs.* salt concentration. The reaction was carried out in 50 mM Tris-HCl buffer (pH 8.0), 5 mM $MgCl_2$ at 37ºC. The initial enzyme and substrate concentrations were 33 pM and 2.5 nM, respectively. The relative activity is the ratio of the activity in the presence of salt to that in the absence of salt. Average values of triplicate experiments with SD value are shown.

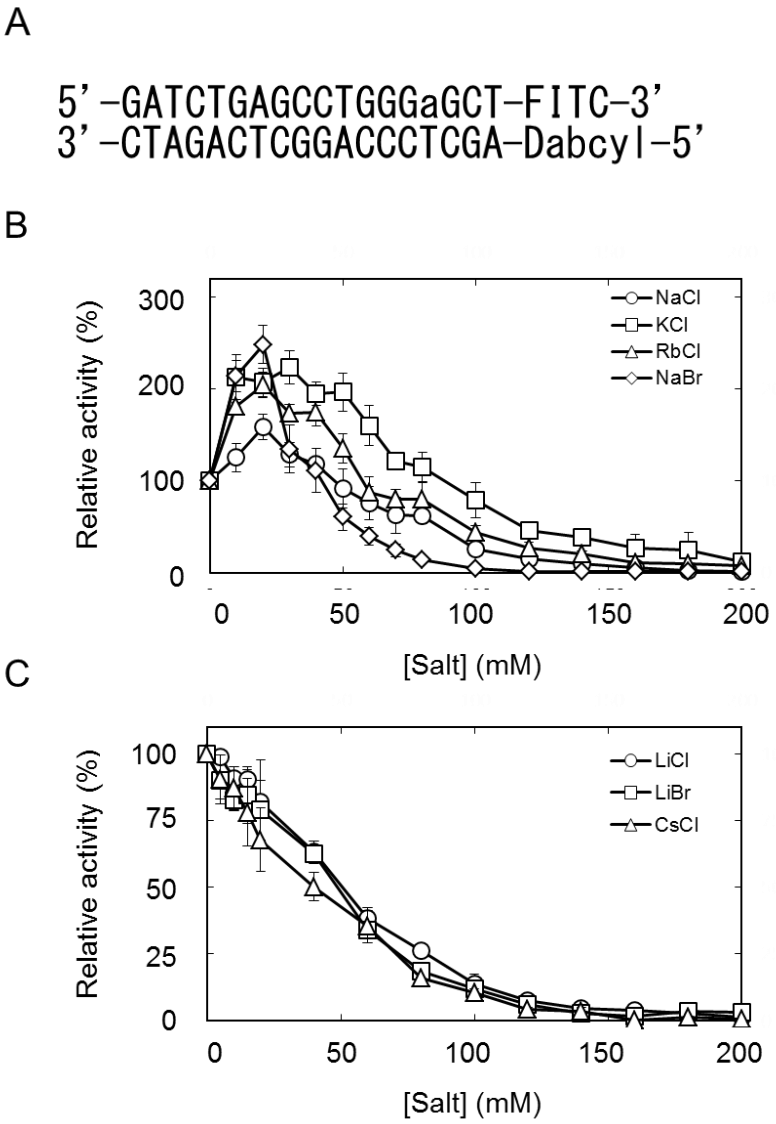

Fig. 8. Effects of salts on the human RNase H2 activity to cleave the DNA_{14}-RNA_1-DNA_3-strand. (A) Sequences of the RNA-DNA hybrid substrate R1/D18. (B, C) Activity *vs.* salt concentration. The reaction was carried out and analyzed as described in Fig. 7.

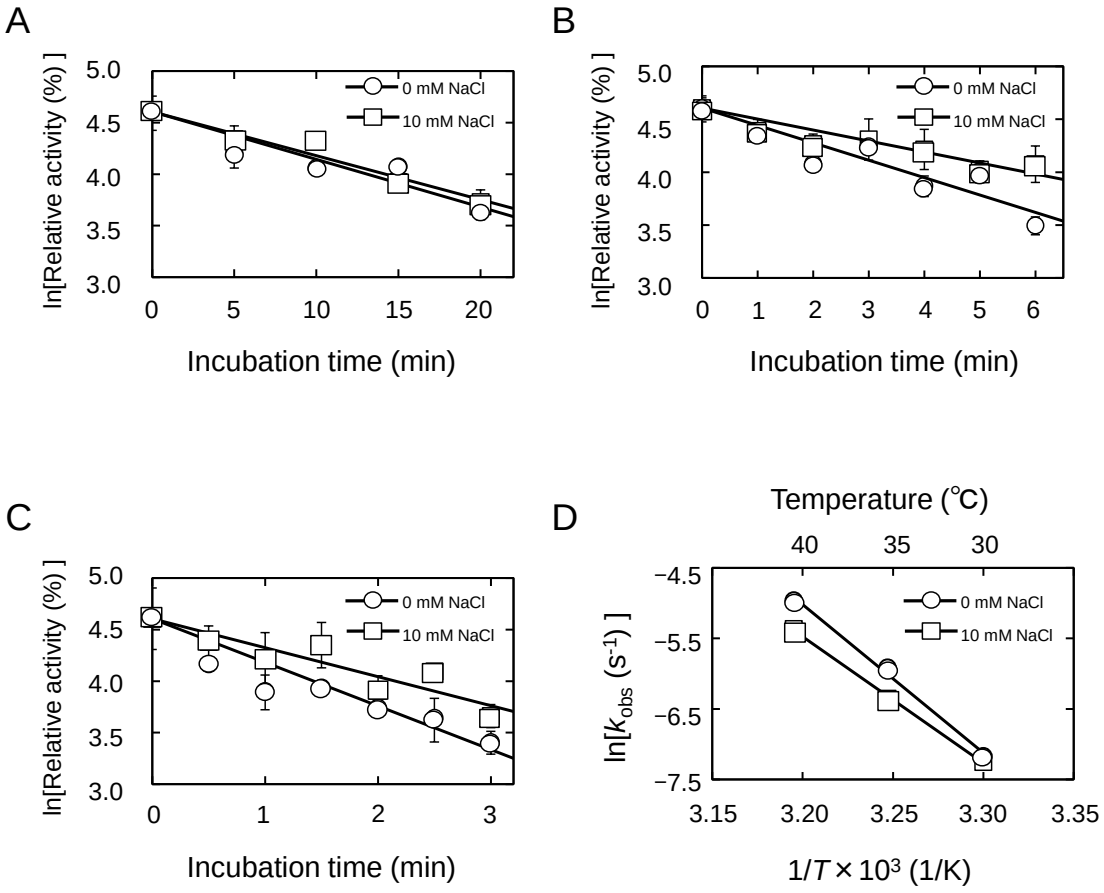

Fig. 9. Irreversible thermal inactivation of human RNase H2. Human RNase H2 (330 pM) was incubated at 30 (A), 35 (B) or 40°C (C) in 20 mM Tris-HCl buffer (pH 7.5) in the presence or absence of 10 mM NaCl for the indicated durations. Then, the reaction was carried out using R18/D18 as described in Fig. 7. The relative activity is the ratio of the initial reaction rate with incubation for the indicated durations to that without incubation. (D) Arrhenius plots of k_{obs} values. The logarithm of k_{obs} values were plotted against the reciprocal of the absolute temperature. Activation energies (E_a) of thermal inactivation were calculated from the slope to be 149 ± 5 kJ mol^{-1} for the presence of 10 mM NaCl and 175 ± 13 kJ mol^{-1} for the absence.

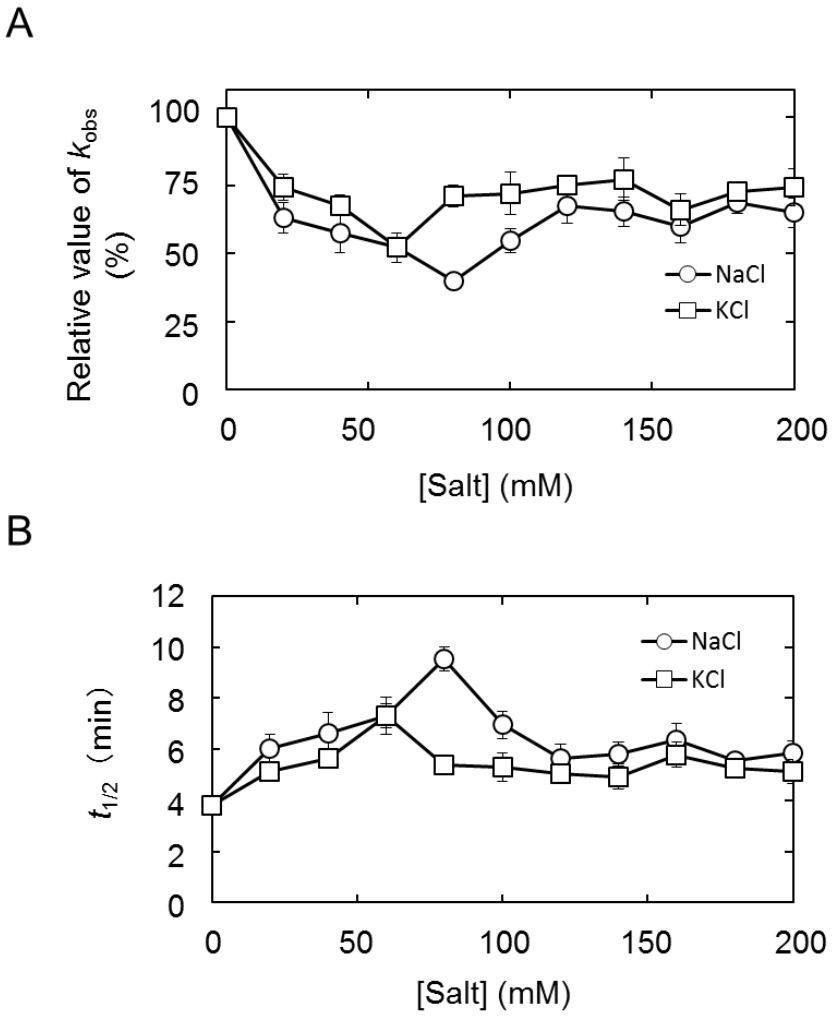

Fig. 10. Effects of salts on the human RNase H2 thermostability. Human RNase H2 (330 pM) was incubated at 37°C in the presence of 0−200 mM NaCl or KCl for specified durations. Then, the human RNase H2 reaction was carried out using R18/D18 as described in Fig. 7. (A) Relative k_{obs} *vs.* salt concentration. The relative k_{obs} is the ratio of the k_{obs} for the incubation of indicated salt concentration to that for the incubation without salts. (B) $t_{1/2}$ *vs.* salt concentration. The $t_{1/2}$ is the time required to reduce initial activity by 50% by the incubation at 37°C. Error bars indicate SD values of triplicate measurements.

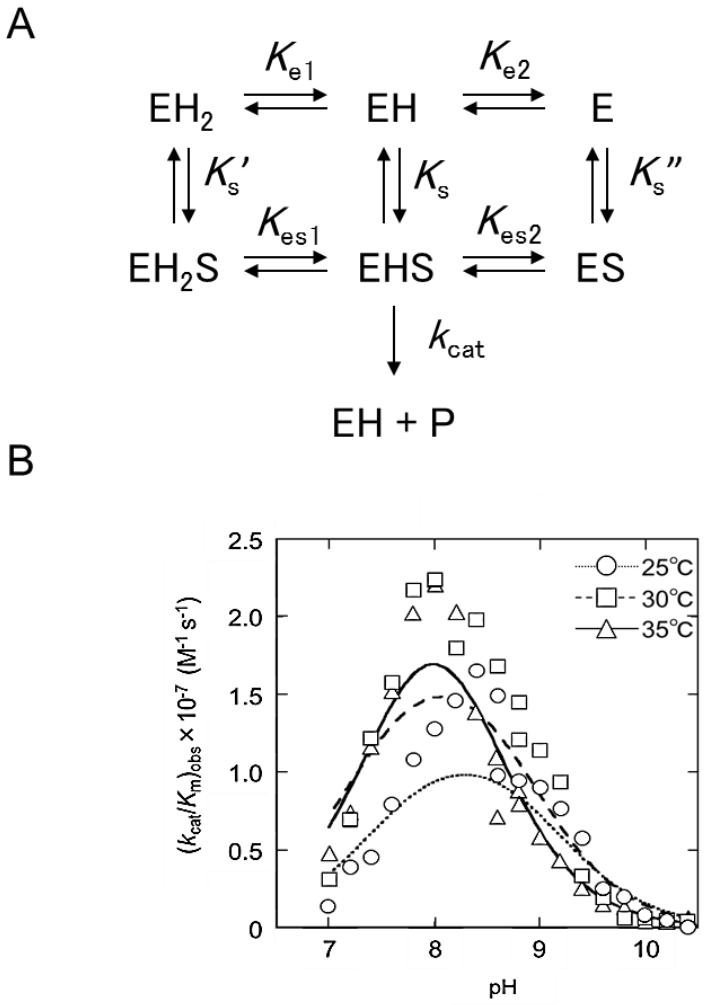

Fig. 11. Effect of pH on human RNase H2 activity. (A) Reaction scheme with two ionizable groups responsible for activity. (B) $(k_{cat}/K_m)_{obs}$ *vs.* pH. The reaction was carried out at 25 (open circle), 30 (open square), and 35ºC (open triangle), each with the initial enzyme and R1/D18 concentrations of 300 pM and 5.6 nM, respectively. Solid line represents a curve expressed by Eq. 1 with the $(k_{cat}/K_m)_o$ value and the pK_{e1} and pK_{e2} values of $(1.2 \pm 0.3)\times10^7$ M^{-1} s^{-1}, 7.4 ± 0.3, and 9.2 ± 0.3, respectively, for 25ºC, $(1.9 \pm 0.5)\times10^7$ M^{-1} s^{-1}, 7.2 ± 0.4, and 8.9 ± 0.3, respectively, for 30ºC, and $(2.9 \pm 0.7)\times10^7$ M^{-1} s^{-1}, 7.5 ± 0.2, and 8.5 ± 0.2, respectively, for 35ºC, which was drawn to fit the experimental data.

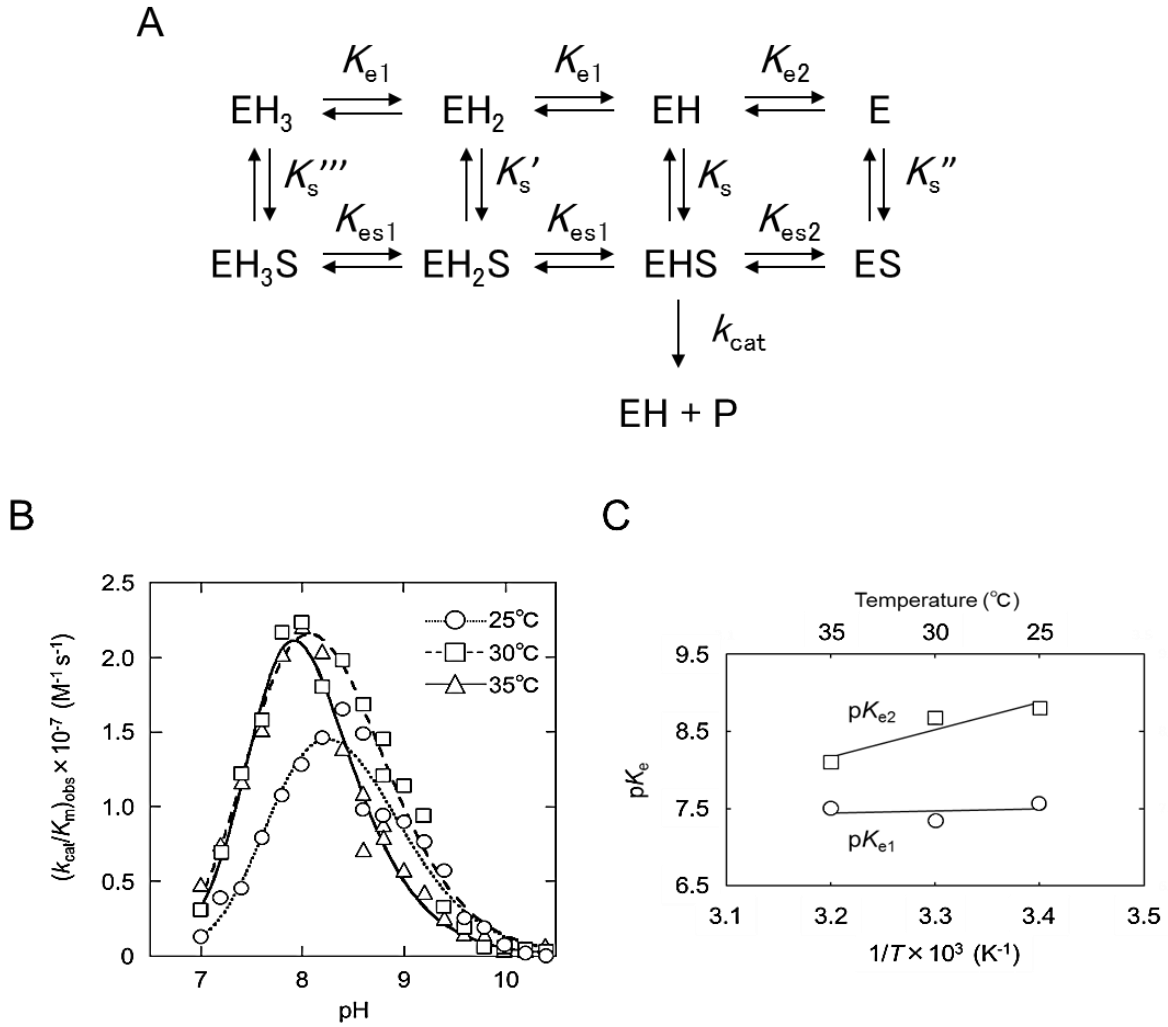

Fig. 12. Effect of pH on the human RNase H2 activity. (A) Reaction scheme with three ionizable groups responsible for activity. Only the EHS complex gives products. (B) $(k_{cat}/K_m)_{obs}$ *vs.* pH. The reaction was carried out at 25 (open circle), 30 (open square), and 35°C (open triangle) with the initial enzyme and R1/D18 concentrations of 300 pM and 5.0 nM, respectively. Solid line represents a curve expressed by Eq. 2 with the $(k_{cat}/K_m)_o$, pK_{e1}, and pK_{e2} values of (1.8 ± 0.2)×10^7 M^{-1} s^{-1}, 7.7 ± 0.1, and 8.9 ± 0.1, respectively, for 25°C, (2.7 ± 0.2)×10^7 M^{-1} s^{-1}, 7.4 ± 0.1, and 8.8 ± 0.1, respectively, for 30°C, and (3.4 ± 0.4)×10^7 M^{-1} s^{-1}, 7.5 ± 0.1, and 8.3 ± 0.1, respectively, for 35°C, which was drawn to fit the experimental data. (C) van't Hoff plot of pK_e values. pK_{e1} and pK_{e2} values were plotted against the reciprocal of the absolute temperature. Enthalpy changes (ΔH^o) of deprotonation were calculated from the slope to be 5 ± 21 kJ mol^{-1} for pK_{e1} and 68 ± 25 kJ mol^{-1} for pK_{e2}.

Chapter 2

Characterization of six recombinant human RNase H2 bearing Aicardi-Goutières syndrome causing mutations

Introduction

As described in General introduction, RNase H2 is involved in the removal of ribonucleotides embedded in genomic DNA, via the process of ribonucleotide excision repair (6). Loss of *Rnaseh2a* (35), *2b* or *2c* (36, 37) in mice leads to early embryonic lethality. Recent results have shown that knockout of RNase H2 gene leads to the accumulation of ribonucleotides in genomic DNA in mouse embryonic fibroblasts (36) and abolishes retroelement propagation in HEK293T cells (38). The yeast RNase H2 mutant bearing a double mutation P45D/Y219A in the A subunit only has RNA strand degrading activity and lacks a single ribonucleotide excision activity (20). This mutant was termed a ribonucleotide excision defective (RED) variant (20). RNase H2 A-subunit gene knockout mice (*Rnaseh2a*$^{-/-}$ and *Rnaseh2a*$^{RED/RED}$) are both embryonic lethal (35), indicating lethality due to abundant ribonucleotides in genomic DNA.

In Aicardi-Goutières syndrome (AGS), a severe neuroinflammatory disorder (9, 10, 14, 15, 39), human patients have bi-allelic mutations in any of seven genes (*RNASEH2A*, *RNASEH2B*, *RNASEH2C*, *TREX1*, *SAMHD1*, *ADAR*, or *IFIH1*). Mutations affecting the activity and/or stability of RNase H2 account for more than 50% of the total AGS patients. The majority of the RNase H2 defects are found in the *RNASEH2B* gene, accounting for 36% of the total AGS patients as of 2015 (39).

Mutations in *RNASEH2A* (5%) and *RNASEH2C* (12%) are less frequently found (39).

To explore the effects of AGS-causing mutations on AGS, it is important to analyze in detail how AGS-causing mutations affect the activity and stability of RNase H2. In Chapter 1, the characteristics of the recombinant wild-type (WT) human RNase H2 expressed in *Escherichia coli* was examined. In Chapter 2, we prepared six recombinant human RNase H2 variants bearing the mutation in G37S, N212I, or R291H in the A subunit, A177T or V185G in the B subunit, or R69W in the C subunit and characterized the activities including the salt dependence and the stabilities.

Materials and Methods

Construction of plasmids – pET15b-hH2ABC described in Chapter 1 was used as an expression plasmid of the wild-type human RNase H2 (WT). Expression plasmids of the variants were constructed by site directed mutagenesis using the pET15b-hH2ABC as a template, *E. coli* BL21(DE3) as a host.

Expression and purification of RNase H2 variants – Expression and purification of human RNase H2 were performed as described in Chapter 1.

RNase H2 assay – RNase H2 assay was performed using a fluorescence substrate as described in Chapter 1. Enzyme reaction was started by adding 20 μl of RNase H2 solution (0.5–5 nM for WT and variants except for A-G37S and 25–200 nM for A-G37S) to the 180 μl of 50 mM Tris-HCl buffer (pH 8.0), 5 mM $MgCl_2$, 60 mM KCl, either of 5.6 nM R1/D18 or 5.6 nM R18/D18 in a 96-well plate. The reaction was

monitored by following the increase in fluorescence intensity at 515 nm with excitation at 490 nm with an EnSight (PerkinElmer) every 5 s for 5 min.

Circular dichroism measurement – Circular dichroism measurement was performed as described in Chapter 1. For the analysis of thermal denaturation of RNase H2, the solution (500 μl) containing RNase H2 (1.0 μM) in 5 mM Tris-HCl buffer (pH 8.3), 20 mM KCl, 5% glycerol was incubated at 25°C for 5 min. After the incubation, the solution (400 μl) was transferred to a 2-mm cell, and mineral oil (50 μl) was added to avoid evaporation. Thermal denaturation was examined by monitoring the CD value at 222 nm, θ_{222}, with increasing cell temperature from 30 to 70°C at a rate of 1°C/min.

Gel filtration chromatography – Gel filtration chromatography was performed as described in Chapter 1.

Results and Discussion

Production of recombinant human RNase H2 variants – Figure 1 shows the structure of human RNase H2 with the amino acid residues to be mutated (28, 34). The C subunit is flanked by the A and B subunits. The C-terminal region of the A subunit interacts with the C and B subunits and emerges from the B subunit becoming visible near the top of the structure. Gly37 and Asn212 in the A subunit are located close to the active site and distant from the B and C subunits. Arg291 is located in the C-terminus of the A subunit, distant from the active site and interacting with the B and C subunits.

Ala177 and Val185 in the B subunit are located close to the C-terminal domain of the A subunit. Arg69 in the C subunit is located close to the A subunit.

Six variant enzymes, named A-G37S (Gly37 in the A subunit is replaced with Ser), A-N212I, A-R291H, B-A177T, B-V185G and C-R69W, were expressed in *E. coli* and purified from the cells. Figure 2 shows the SDS-PAGE pattern of the enzyme preparations under reducing conditions. WT and variants yielded three bands with molecular masses of 35.6, 34.2 and 18.6 kDa, corresponding to the B, A and C subunits, respectively. Figure 3 shows the CD spectroscopy of the enzyme preparations. WT and the six variants exhibited negative ellipticities at 210–250 nm. No appreciable changes were observed in each spectra between WT and variants. The results of SDS-PAGE and CD spectroscopy suggest that WT and all variants were purified as a heterotrimer to homogeneity, and that all variants did not suffer from any global or drastic structural changes.

Effects of mutation on the RNase H2 activity – We analyzed the effects of mutation on the RNase H2 activity by the fluorescence-based activity assay with R1/D18 and R18/D18 as the substrates. The activity was expressed by the initial reaction rate, which was obtained by following the increase in fluorescence intensity of the reaction solution. The dependences on the enzyme concentration of the activity are shown in Fig. 4A and B for the hydrolysis of R1/D18 and in Fig. 4C and D for the hydrolysis of R18/D18. The activities of WT and all variants increased linearly with increasing enzyme concentration. The activities of A-G37S were markedly lower than those of WT and the other five variants.

Table 1 shows summary of the activities of WT and the six variants in Fig. 4. The relative activities, defined as the ratio of the activity to that of WT, of A-G37S were markedly decreased for the hydrolysis of R1/D18 and R18/D18 (0.01 and 0.003, respectively), while those of other five variants were close to 1 (0.51–1.0 for R1/D18 and 0.71–1.2 for R18/D18). Our results were almost concordant with the results previously reported (Table 2) except for A-G37S. In Coffin et al. (10), the relative activities of A-G37S were 0.3 both for the hydrolysis of DNA_{16}-RNA_4-DNA_{10}/DNA_{30} (4-ribo) and RNA_{20}-DNA_{10}/DNA_{30} (20-ribo). They expressed the activities by the amounts of cleaved fragment during the incubation of the enzyme with 200 nM 4-ribo or 20-ribo at 25°C for 20 min, which were assessed by gel electrophoresis of the reaction products. We expressed the activities by the increase in fluorescence intensity of the reaction solution during the incubation of the enzyme with 5.6 nM R18/D18 at 25°C. We speculate that the discrepancy might be explained by the lowered affinity of A-G37S to the substrate and the difference in substrate concentrations in the reaction.

Effects of AGS-causing mutation on the salt-dependence of RNase H2 activity – In Chapter 1, the effects of neutral salts on the activity of WT in the hydrolysis of R1/D18 and R18/D18 were analyzed: NaCl, KCl, RbCl and NaBr increased the activity to 170–390%, while LiCl, LiBr and CsCl inhibited it, suggesting that species of cation, but not anion, is responsible for activity. We examined the effects of NaCl on the hydrolysis of R1/D18 (Fig. 5A) and R18/D18 (Fig. 5B), the effects of KCl on the hydrolysis of R1/D18 (Fig. 5C) and R18/D18 (Fig. 5D) and the effects of CsCl on the hydrolysis of R1/D18 (Fig. 5E) and R18/D18 (Fig. 5F). Relative activity of RNase H2 was defined as the ratio of the activity in the presence of salt to that in the absence. The relative

activities of WT and all variants were the highest at 20 mM NaCl or KCl (350% for WT and 100–250% for variants in the hydrolysis of R1/D18 (Fig. 5A), 500% for WT and 110–580% for variants in the hydrolysis of R18/D18 (Fig. 5B), 170% for WT and 110–270% for variants in the hydrolysis of R1/D18 (Fig. 5C) and 400% for WT and 190–320% for variants in the hydrolysis of R18/D18 (Fig. 5D)) and decreased with increasing NaCl or KCl concentrations. These results indicated that all variants exhibited relatively similar NaCl- and KCl-dependences of activity to WT, but the profiles were different between the hydrolysis of R1/D18 and R18/D18. Considering that potassium ion is abundant intracellularly, our results suggested that it might inhibit the RNase H2 activity in cells to some extent. The relative activities of WT and all variants except for A-G37S were stable or slightly increased at 0–60 mM CsCl in the hydrolysis of R1/D18 (Fig. 5E) and at 0–20 mM CsCl in the hydrolysis of R18/D18 (Fig. 5F) and decreased with increasing CsCl concentrations. A-G37S exhibited more rapid decrease than WT and other variants. These results indicated that all variants except for A-G37S exhibited similar CsCl-dependences of activity to WT, but the profiles were different between the hydrolysis of R1/D18 and R18/D18 like the case with the NaCl-dependences.

From these results, we speculate that the salt-based activation and inhibition of human RNase H2 might result from not only the interaction between respective ions and particular residues but also the interaction between respective ions and the RNA/DNA hybrid. In DNA synthesis by DNA polymerase, two Mg^{2+} ions bind the enzyme whereas another Mg^{2+} ion binds the α-phosphate oxygen of the incoming dNTP (41, 42). This third Mg^{2+} is thought to be involved in fidelity (43). We reported the effects of Mg^{2+} concentrations on the RNA-dependent DNA synthesis by reverse transcriptases were

different from those on the DNA-dependent DNA synthesis (44). These evidences support our speculation that the neutral salts might affect RNase H2 activity partly by interacting with the RNA/DNA hybrid.

Effects of AGS-causing mutation on RNase H2 stability – To analyze the effects of AGS-causing mutation on the RNase H2 stability, CD-based assay by monitoring θ_{222} in the range of 30–70°C was performed (Fig. 6). The denaturation curves of WT and variants showed apparent two-state model as expressed in Scheme 1

$$N \rightleftarrows D \qquad (Scheme\ 1)$$

where N and D represent the native and denatured species, respectively. Fraction unfolded (F_u) was determined according to Eq. 1 after normalizing θ_{222} of native and denatured RNase H2 between 0 and 1.

$$F_u = (A_O - A_N)/(A_D - A_N) \qquad (Eq.\ 1)$$

where A_O is the observed θ_{222} of RNase H2 at various temperatures, and A_N and A_D are θ_{222} of native and denatured enzymes, respectively. The melting temperature (T_m) was defined as the one at which F_u is 0.5. The T_m values were 56°C for WT, 53°C for A-N212I, A-R291H, B-A177T, B-V185G and C-R69W and 50°C for A-G37S. These results indicated that all six AGS-causing mutations decreased the stability. The marked decrease in A-G37S was contrary to that glycine replacement is one of general strategies

in protein engineering to increase protein stability. Our results suggest that Gly37 in the A subunit plays an important role not only in activity but also in stability.

According to Günther et al (44), the fluorescence-based thermal shift assay (ThermoFluor Assay) revealed that the T_m values of human RNase H2 variants B-F95L and B-A177T were lower by 9°C and 3°C, respectively, than that of WT, while those of other 13 variants were similar to that of WT (Table 2). In this study, the T_m values of all six variants were lower by 3–6°C than that of WT. This discrepancy might be due to the difference in the mechanism to detect denaturation between the two methods, the binding of dye to hydrophobic patches in the thermal shift assay and the detection of α helix in CD.

Effects of AGS-causing mutation on the dissociation of RNase H2 subunits – In Chapter 1, WT was eluted as a single peak at the retention time corresponding to a molecular mass of the heterotrimer (88 kDa) in gel filtration chromatography (GFC) of the purified enzyme preparation. We examined if AGS-causing mutations affected the heterotrimer-forming stability under the condition that the enzyme concentration is low. Figure 7 shows the GFC elution pattern of WT and variants together with the SDS-PAGE patterns of the GFC fractions. In GFC, L-Arg (0.5 M) was contained in the equilibrium buffer to improve resolution (45), although WT and all variants of RNase H2 did not exhibit the activity in the presence of 0.5 M L-Arg. When 8.6 μg of WT was applied, a single peak appeared at the retention time of 15.3–16.5 min. The peak fractions contained all A, B and C subunits, suggesting that WT was eluted as a heterotrimer. Same results were obtained with other five variants except for A-R291H. When 8.6 μg of A-R291H was applied, two peaks appeared at the retention time of

15.3–17.7 and 17.7–18.7 min, respectively. The first peak fractions contained all three subunits, while the second peak contained only the A subunit. These results suggested that in A-R291H, the heterotrimer dissociated into the A subunit and, presumably, the complex of the B and C subunits. The presence of the complex of the B and C subunits was previously suggested in the co-expression of the A subunit which lacked the C-terminal and the intact B and C subunits (34). When 2.9 μg of enzyme was applied, multiple peaks appeared in A-G37S, A-R291H, B-A177T and B-V185G. On the other hand, when 26 μg of enzyme was applied, such multiple peaks were less obvious, indicating that dissociation depended on enzyme concentration. These results suggested that the AGS-causing mutations decrease the heterotrimer-forming stability.

Conclusion – The AGS-causing mutations affected the activity and stability of human RNase H2 with varying degrees depending on mutation species. A-G37S exhibited markedly lower activity and stability than other variants, while other five variants had decreased stability rather than decreased activity. Uehara et al (35) showed that even G37S was active enough for mouse embryo to survive to birth. Construction of mammalian cells possessing the AGS-causing mutation in the RNase H2 gene and characterization of the cellular events of the cells and the activity and stability of the RNase H2 variants expressed in the cells are required for exploring the effects of the mutation on cellular events.

Table 1. Activity of RNase H2 variants.

	R1/D18 hydrolysis[a] ($v_o/[E]_o$) × 1000 (s^{-1}) (A)	R18/D18 hydrolysis[a] ($v_o/[E]_o$) × 1000 (s^{-1}) (B)	B/A
WT	111 (1.0)[b]	177 (1.0)	1.6 (1.0)
A-G37S	1.0 (0.01)	0.3 (0.003)	0.3 (0.19)
A-N212I	73 (0.66)	144 (0.81)	2.0 (1.3)
A-R291H	57 (0.51)	212 (1.2)	3.7 (2.3)
B-A177T	109 (0.98)	127 (0.72)	1.2 (0.75)
B-V185G	82 (0.74)	127 (0.72)	1.5 (0.93)
C-R69W	112 (1.0)	125 (0.71)	1.1 (0.70)

[a]The reaction was carried out in 50 mM Tris-HCl buffer (pH 8.0), 5 mM $MgCl_2$, 60 mM KCl, 5.6 nM R1/D18 or 5.6 nM R18/D18 at 25ºC.

[b]Numbers in parentheses indicate values relative to WT.

Table 2. Activity and stability of RNase H2 variants previously reported.

	Substrate used for measuring the activity					ΔT_m
	p(rA)/p(dT)[a]	1-ribo[b]	4-ribo[c]	20-ribo[d]	18-ribo[e]	(°C)[f]
A-G37S	< 0.01[g] (19)[h]	< 0.01 (19), 0.005 (10)	0.3 (10)	0.3 (10)		
A-E75Q/A-E294K		0.6 (46)				–1 (46)
A-R108W		0.3 (10)	0.5 (10)	1 (10)		
A-A121T		1 (46)				0 (46)
A-V133M		0.4 (47)			0.1 (47)	–1.3 (47)
A-P158S		0.5 (47)			0.6 (47)	–1.8 (47)
A-A178V		< 0.01 (46)				–1 (47)
A-R186W		0.006 (10)	0.1 (10)	0.1 (10)		
A-L202S		0.7 (46)				0 (46)
A-L202S/A-D205E		0.5 (46)				0 (46)
A-N212I		1 (10)	1 (10)	1 (10)		
A-K221R		0.7 (46)				0 (46)
A-I244V		0.5 (46)				0 (46)
A-F230L		0.8 (10)	0.3 (10)	0.3 (10)		
A-R235Q		0.003 (10)	0.002 (10)	0.001 (10)		
A-T240M		0.1 (10)	1 (10)	2 (10)		
A-R280G		0.9 (47)			1 (47)	–0.5 (47)
A-R291H		0.05 (34), 2 (10)	2 (10)	2 (10)		–0.7 (34)
B-G10R		0.4 (46)				–1 (46)
B-F95L		0.4 (46)				–9 (46)
B-D105A		0.3 (46)				–1 (46)
B-K162T	1 (19)	1.1 (19)				
B-A177T	1 (19)	0.6 (19), 1 (34), 1 (46)				–3(34, 46)
B-V185G	0.9 (19)	0.8 (19)				
B-K233Q		0.2 (46)				–1 (46)
B-K248N		0.1 (46)				–1 (46)
B-T280A		0.9 (47)			1 (47)	–0.5 (47)
B-A287S		0.2 (46)				0 (46)
C-R69W	0.4 (19)	0.3 (19), 0.3 (34)				–2.6 (34)
C-P76L		0.8 (34)				–3 (34)
C-K90del		0.9 (46)				–1 (46)
C-E110P		0.9 (46)				–1 (46)
C-P138L		1 (34)				–2.4 (34)
C-K143I	0.9 (19)	0.7 (19), 0.1 (34)				–0.8 (34)
C-R145C		0.6 (47)			0.7 (47)	–0.5 (47)
C-P151S		0.1 (34)				–3.3 (34)

Variants characterized in this study are marked in bold.

[a]poly(rA)/poly(dT);

[b]DNA_{12}-RNA_1-DNA_{27}/DNA_{40} (19), DNA_{14}-RNA_1-DNA_3/DNA_{18} (34), DNA_{19}-RNA_1-DNA_{10}/DNA_{30} (10);

[c]DNA_{16}-RNA_4-DNA_{10}/DNA_{30}; [d]RNA_{20}-DNA_{10}/DNA_{30}; [e]RNA_{18}/DNA_{18};

[f]ΔT_m [= (T_m of variants) – (T_m of WT)] in the fluorescence-based thermal stability assay;

[g]The activitiy compared to that of the wild-type RNase H2; [h]Numbers in parentheses indicate references.

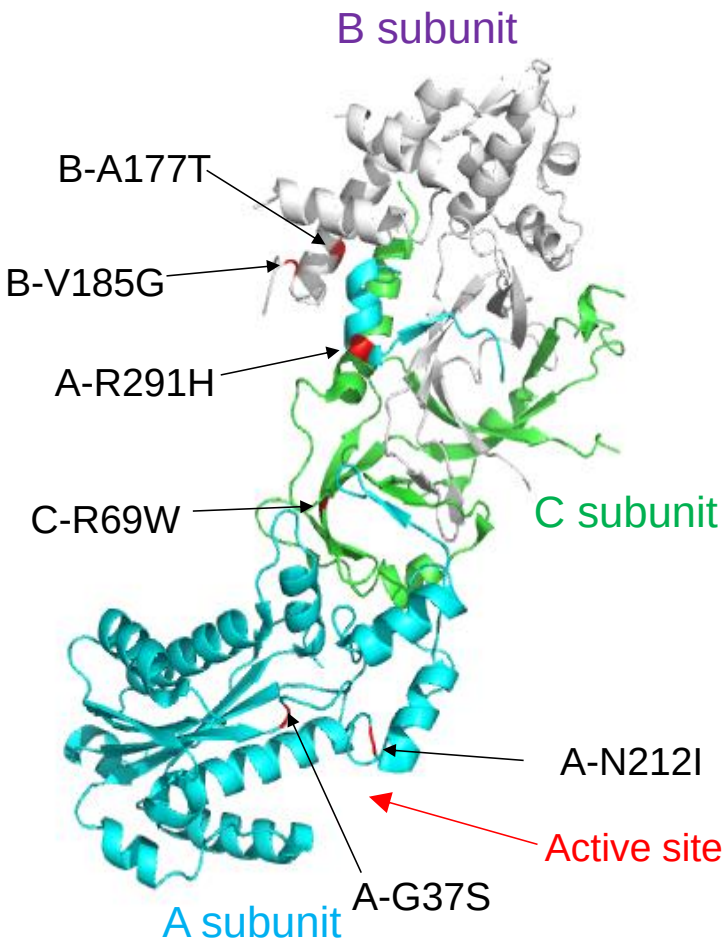

Fig. 1. Structure of human RNase H2. The PyMOL program was used to visualize the whole structure of human RNase H2 (PDB accession no. 3PUF). Mutated residues, Gly37, Asn212, and Arg291 in the A subunit, and Ala177 and Val185 in the B subunit, and Arg69 in the C subunit are colored in red.

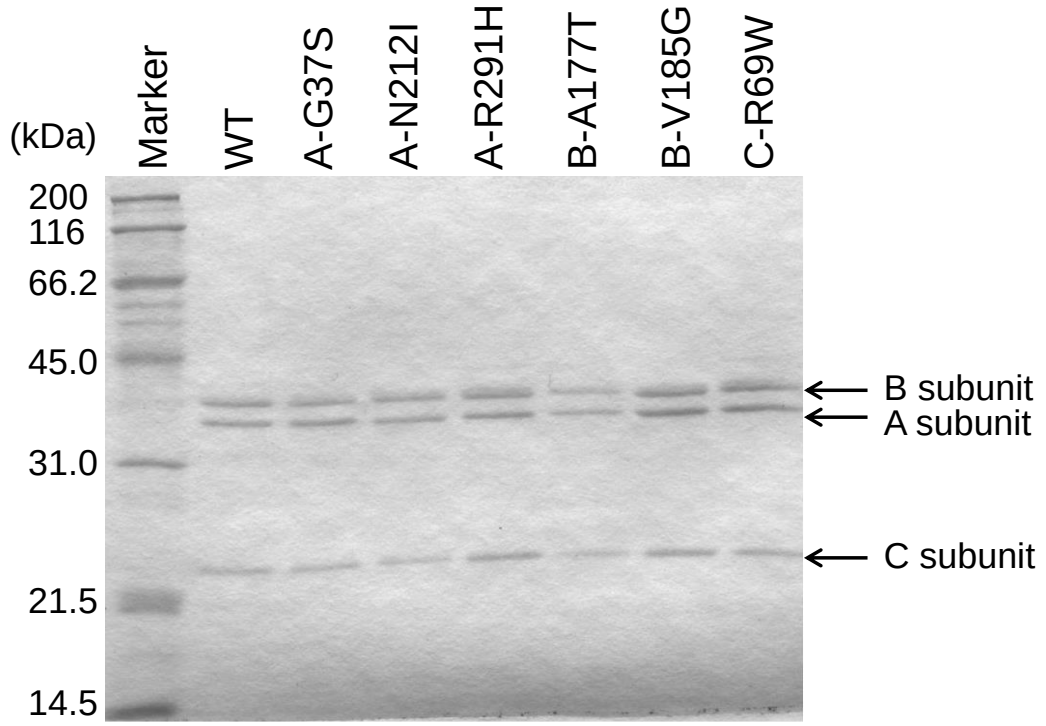

Fig. 2. SDS-PAGE of human RNase H2 variants under reducing conditions. Coomassie Brilliant Blue-stained 12.5% SDS-polyacrylamide gel showing marker proteins (Protein Molecular Weight Marker (Broad), Takarabio, Otsu, Japan) and purified enzyme preparations of the wild-type human RNase H2 and its variants.

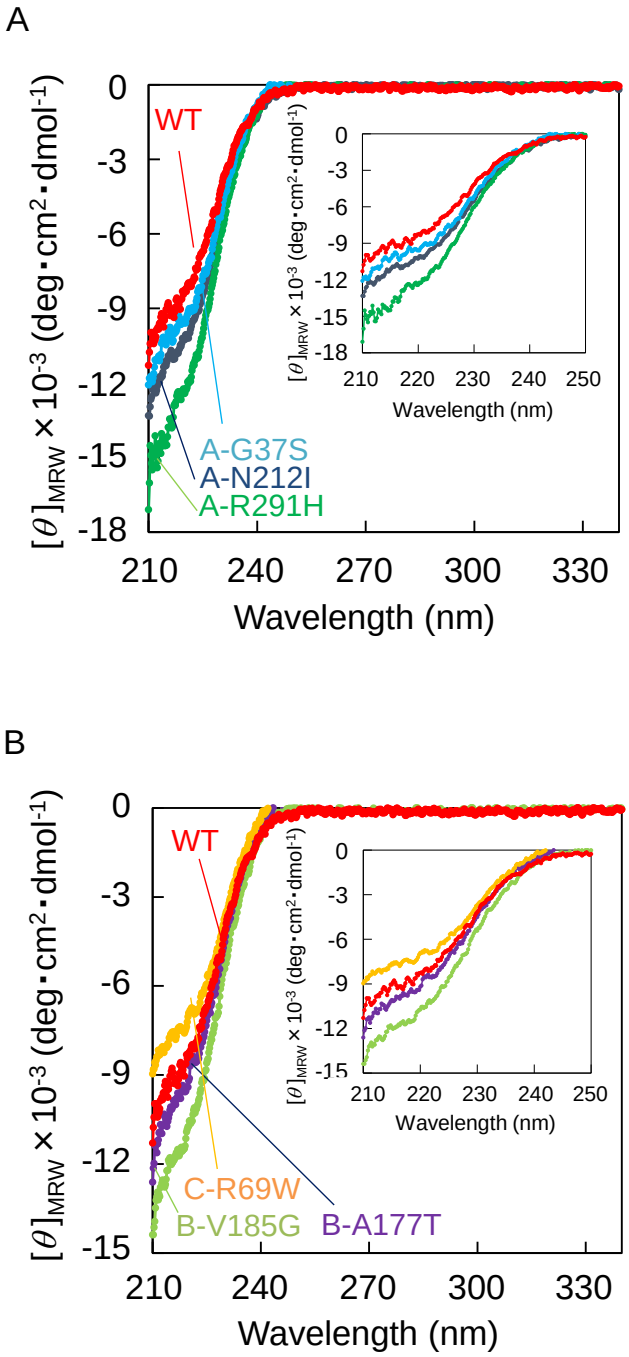

Fig. 3. CD spectra of human RNase H2 variants. The spectra at 210–340 nm were measured in 5 mM Tris-HCl buffer (pH 8.3), 20 mM KCl, 5% glycerol at 25ºC with protein concentrations of 1.0 μM. Inset shows the spectra at 210–250 nm.

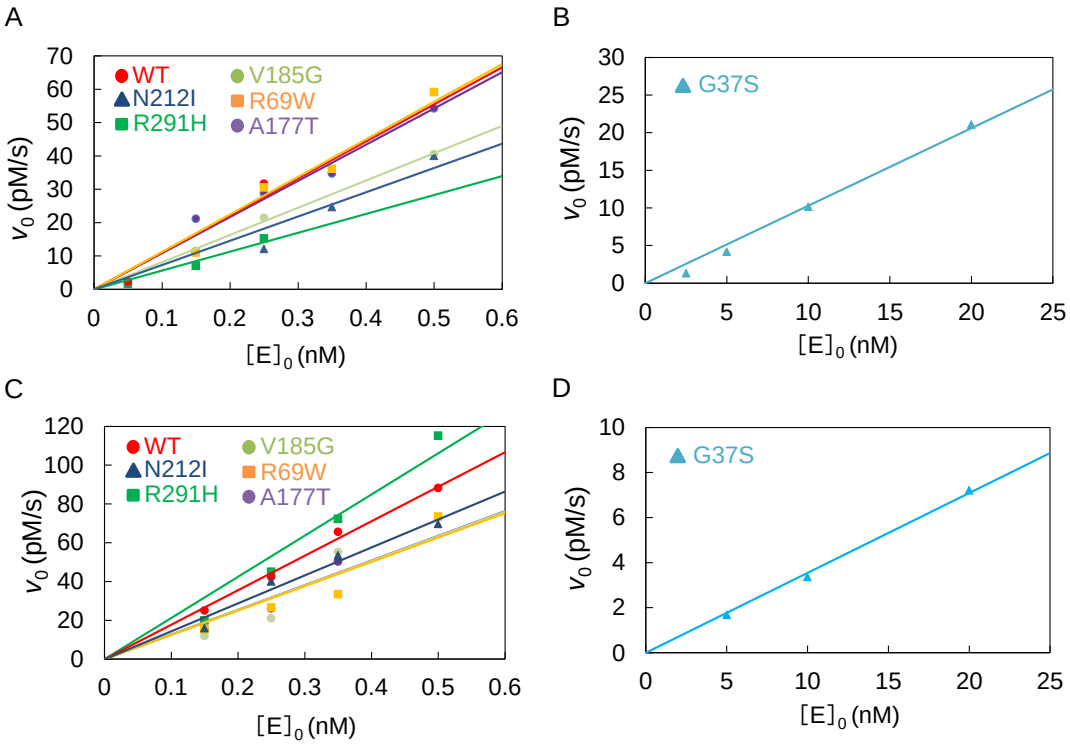

Fig. 4. Dependence of activity of human RNase H2 variants on the enzyme concentration. (A) Hydrolysis of R1/D18 by A-N212I, A-R291H, B-A177T, B-V185G, and C-R69W. (B) Hydrolysis of R1/D18 by A-G37S. (C) Hydrolysis of R18/D18 by A-N212I, A-R291H, B-A177T, B-V185G, and C-R69W. (D) Hydrolysis of R18/D18 by A-G37S. The reaction was carried out in 50 mM Tris-HCl buffer (pH 8.0), 5 mM $MgCl_2$, 60 mM KCl at 25ºC.

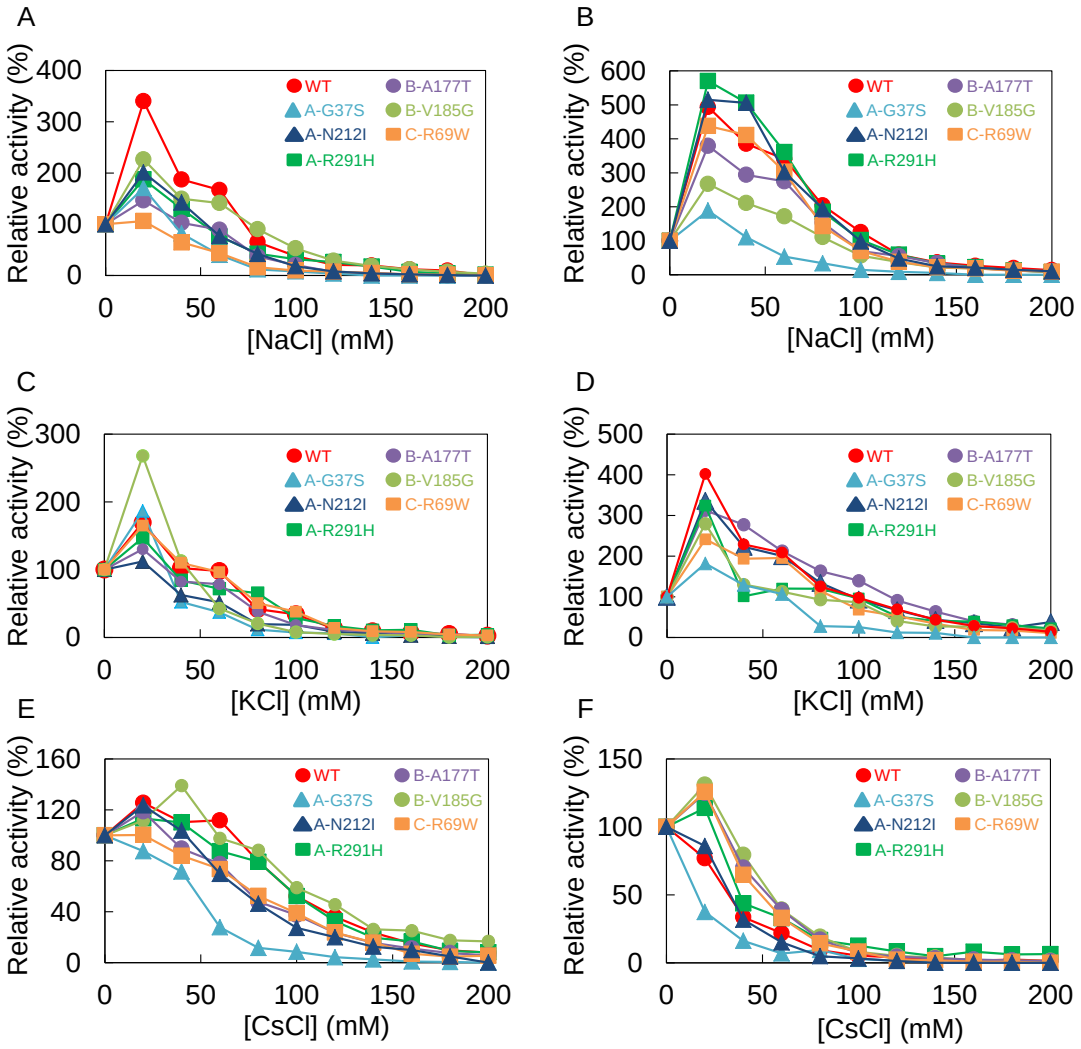

Fig. 5. Dependence of activity of human RNase H2 variants on salt concentration. (A) Hydrolysis of R1/D18 at 0–200 mM NaCl. (B) Hydrolysis of R18/D18 at 0–200 mM NaCl. (C) Hydrolysis of R1/D18 at 0–200 mM KCl. (D) Hydrolysis of R18/D18 at 0–200 mM KCl. (E) Hydrolysis of R1/D18 at 0–200 mM CsCl. (F) Hydrolysis of R18/D18 at 0–200 mM CsCl. The reaction was carried out in 50 mM Tris-HCl buffer (pH 8.0), 5 mM $MgCl_2$, 0–200 mM NaCl, KCl, or CsCl at 25ºC.

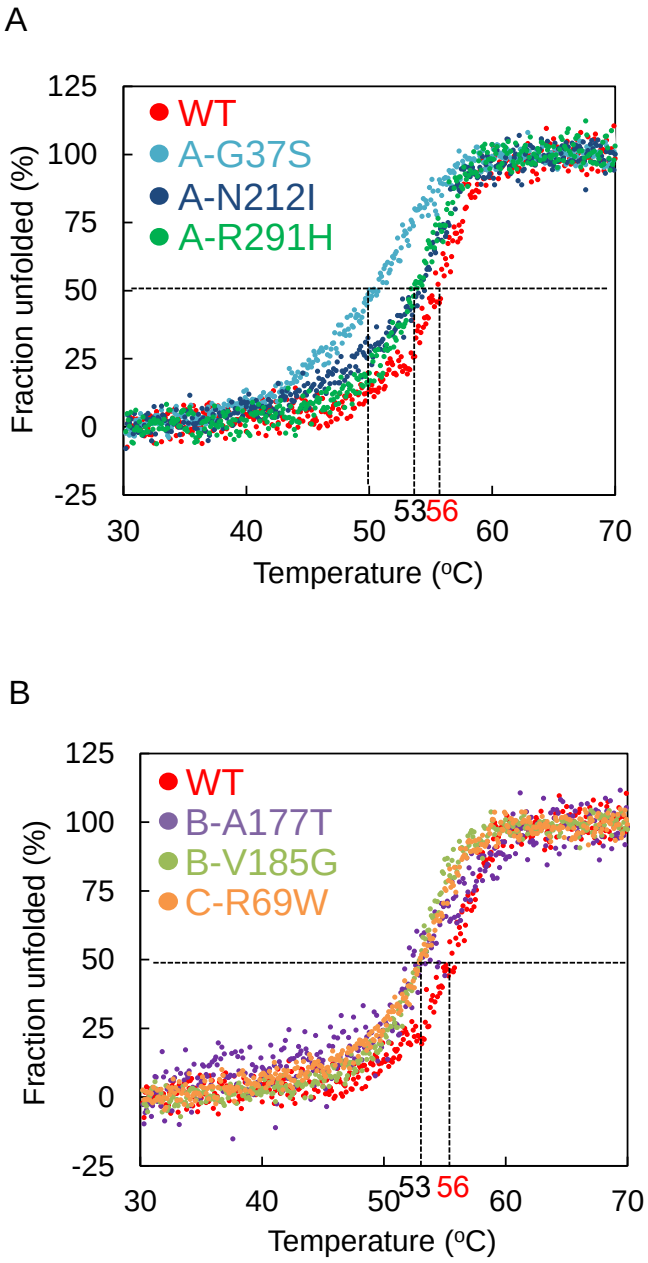

Fig. 6. Thermal denaturation of human RNase H2 variants. θ_{222} of WT and variants were monitored from 30 to 70ºC at 1ºC/min. (A) WT, A-G37S, A-N212I, and A-R291H. Their melting temperatures are 56, 50, 53, and 53ºC, respectively. (B) WT, B-A177T, B-V185G, and C-R69W. Their melting temperatures are 56, 53, 53, and 53ºC, respectively.

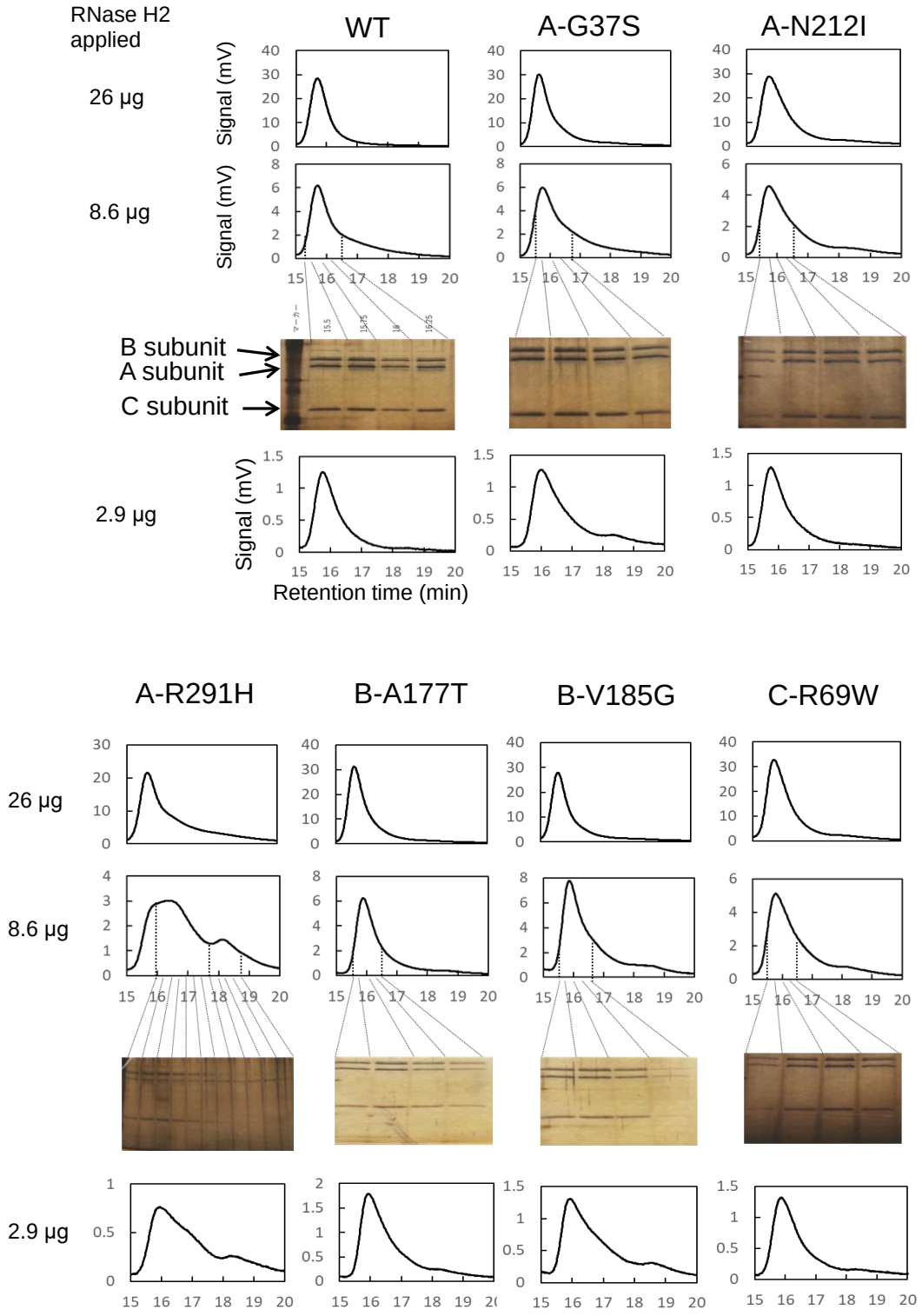

Fig. 7. Elution patterns of gel filtration column chromatography of human RNase H2 variants. WT and variants (26, 8.6, or 2.9 μg) were applied onto the column. Silver-stained 12.5% SDS-polyacrylamide gel is also shown.

Chapter 3

Val143 of human RNase H2 is not critical for, but plays a role in determining catalytic activity and substrate specificity

Introduction

Seven crystal structures of RNases HII and RNases H2 are currently available (48). In mouse (23) and human (28, 34) RNases H2, the C subunit is flanked by the A and B subunits, and the N-terminal domain of the B subunit and the entire C subunit are intimately interwoven to form the triple β-barrel fold, which interacts with the C-terminal domain of the A subunit. The active site in the A subunit has a conserved GRG (Gly37, Arg38, and Gly39 in human), DEDD (Asp34, Glu35, Asp141, and Asp169 in human) and DSK (Asp67, Ser68, and Lys69 in human) motifs. Residues in the DEDD motif coordinate metal ions. The GRG motif- and DSK motif-containing loops are located close to the active site to recognize a substrate.

The structure of the complex of *Thermotoga maritima* RNase HII and a hybrid consisting of DNA_5-RNA_1-DNA_6 and DNA_{12} revealed that the hydroxyl group of the side chain of Tyr163 is located in the proximity with the 2'-OH of the sugar moiety of the ribonucleotide at the 3' side of the scissile phosphodiester bond of the substrate (4). This Tyr residue is conserved in RNase HII and RNase H2. In yeast RNase H2, the counterpart of this tyrosine residue is Tyr219. This tyrosine residue is critical for substrate specificity.

Unlike the tyrosine residue mentioned above, little is known about a role of other

conserved amino acid residues in the active site of RNase H2 in activity and stability. The active-site residue Val143 (Fig. 1) is conserved in eukaryotic RNase H2 but not in prokaryotic RNase HII (Fig. 2). In Chapter 3, to explore the role of Val143 in the RNA strand degrading and single ribonucleotide excision activities, we performed saturation mutagenesis of this residue and analyzed the variants.

Materials and Methods

Construction of plasmids – pET15b-hH2ABC described in Chapter 1 was used as an expression plasmid of the wild-type human RNase H2 (WT). Expression plasmids of variants were constructed by site directed mutagenesis using the pET15b-hH2ABC as a template, *E. coli* BL21(DE3) as a host.

Purification of RNase H2 variants – Purification of human RNase H2 was performed as described in Chapter 1.

RNase H2 assay – RNase H2 assay was performed using a fluorescence substrate as described in Chapter 1. The reaction was started by adding 20 μl of RNase H2 solution (0.03–350 nM) to the 180 μl of 50 mM Tris-HCl buffer (pH 8.0), 5 mM $MgCl_2$, 0–200 mM KCl, either of 5.6 nM R1/D18 or 5.6 nM R18/D18 in a 96-well plate at 25°C. The reaction was monitored by following the increase in fluorescence intensity at 515 nm with excitation at 490 nm with an EnSight (PerkinElmer) every 5 s for 5 min.

Circular dichroism measurement – Circular dichroism measurement was

performed as described in Chapter 1 and 2.

Results and Discussion

Location of Val143 in the active site of human RNase H2 – Val143 is located in the small loop (Val143-Gly144-Met145) connecting the β sheet (Val135–Thr142) that contains Asp141 of the DEDD motif and the α helix (Pro146–Ser156) that is closely located to Arg38 of the GRG motif (Fig. 1). Val143 is conserved only in eukaryotic RNase H2 (Fig. 2). We thus hypothesized that Val143 plays an important role and explored its role by saturation mutagenesis. Figures 3 and 4 show the modelled human RNase H2 complexed with an RNA/DNA hybrid, suggesting that Val143 is located near the sugar moiety of the deoxyribonucleotide at the 5' side of the scissile phosphodiester bond of the substrate although they are crude modeling.

Production of recombinant human RNase H2 variants – Expression and purification of 19 Val143 variants from *E.coli* was attempted. However, purified preparations were not obtained for V143C and V143M. This might be due to unfavorable structural damage caused by the substitution of sulfur-containing amino acids. Figure 5 shows the SDS-PAGE pattern of the preparations of the wild-type human RNase H2 (WT) and other 17 variants under reducing conditions. WT and all variants yielded three bands with molecular masses of 35.6, 34.2, and 18.6 kDa, corresponding to the B, A, and C subunits, respectively.

Effects of mutation of Val143 on the RNase H2 activity – We analyzed the effects of

mutation of Val143 on RNase H2 activity by the fluorescence based assay with R1/D18 and R18/D18 as substrates. The initial reaction rate was obtained by following the increase in fluorescence intensity of the reaction solution. In both substrates, the initial reaction rates of WT and all 17 variants increased linearly with increasing enzyme concentration (Fig. 6). However, the slope differed depending on variants and substrates. Table 1 shows initial reaction rate for WT and 17 variants. When the activity of WT was set as 100%, the relative activities for R1/D18 of the 17 variants were in the range of 0.05–130%, and those for R18/D18 were in the range of 0.02–42%. In the hydrolysis of R1/D18, V143I exhibited the highest activity followed by WT. In the hydrolysis of R18/D18, WT exhibited the highest activity followed by V143I. When the ratio of the relative activity for R1/D18 to the relative activity for R18/D18 of WT was set as 1, the ratios of the 17 variants were in the range of 0.2–5.7, indicating that the substrate specificity varied depending on variants. For the grouping of variants, the hydrolytic activities of WT and the 17 variants for R1/D18 and R18/D18 were compared (Fig. 7). All variants can be divided into three groups according to the residue into which Val143 was substituted: (i) Variants with charged residues at position 143 (V143D, V143E, V143K, V143H, and V143R). Their relative activities for R1/D18 and R18/D18 were markedly reduced (less than 2% of that of WT). (ii) Variants with bulky hydrophobic (V143F, V143I, V143L, and V143W) or bulky polar (V143Y) residues at position 143. Their relative activities for R1/D18 and R18/D18 were moderate (15–130% of that of WT). (iii) Variants with non-bulky hydrophobic (V143A and V143G) or non-bulky polar (V143N, V143P, V143Q, V143S, and V143T) residues at position 143. Their relative activities for R1/D18 and R18/D18 were markedly reduced (less than 2% of that of WT). In order to examine the effects of the amino acid residue at position 143 on the

activity and structure of human RNase H2, we selected V143D and V143K from group (i), V143I and V143Y from group (ii), and V143G and V143N from group (iii) for subsequent analyses.

The catalytic mechanism of human RNase H2 has been described as follows. Two metal ion mechanism of DNA polymerase (49), in which two divalent metal ions are present in the active site and are coordinated by the carboxylate of the conserved aspartate residues and the α-phosphate oxygen of the incoming dNTP, can be applied to RNase H (48), considering that the α-phosphate oxygen of the incoming dNTP corresponds to the oxygen of the scissile phosphodiester bond. In the crystal structure of the complex of *Thermotoga maritima* RNase HII and a DNA_5-RNA_1-DNA_6/DNA_{12} hybrid, two Mg^{2+} ions in the active site are coordinated by Asp18, Glu19, Asp107, and Asp124 of the DEDD motif; Lys47 of the DSK motif interacts with the non-bridging oxygen of the scissile phosphodiester bond; and Arg22 of the GRG motif and Tyr163 interact with the oxygen of 2'-OH of the sugar moiety of the ribonucleotide at the 3' side of the scissile phosphodiester bond (4). In Chapter 1, ionizable groups responsible for acidic pK_e might be two of the three Asp34, Glu35 and Asp141 of DEDD motif, and that for alkaline pK_e might be Lys69 of DSK motif by thermodynamic analysis, pH and temperature dependence of human RNase H2 activity. Thus, the following catalytic mechanism can be proposed for human, and probably other eukaryotic, RNase H2. In the absence of substrate, the enzyme Asp34, Glu35, and Asp141 of DEDD motif must be in their deprotonated state to coordinate two Mg^{2+} ions, and Lys69 must be in their unionized state for catalysis. Michaelis complex is formed, in which Arg38 of the GRG motif, Tyr210 that is a counterpart of Tyr163 in *T. maritima* RNase HII, and Lys69 of the DSK motif are involved in the binding with an RNA/DNA hybrid. Mg^{2+} ion

polarizes the phosphodiester bond by coordinating to the non-bridging oxygen of the scissile phosphodiester bond. The complex in the transition state is formed when the ionized Mg^{2+}-bound water attacks the phosphorus of the scissile bond. The phosphodiester bond is incised when the proton that binds to the non-bridging oxygen of the scissile phosphodiester bond is transferred to the binding oxygen of the scissile phosphodiester bond. In this mechanism, Val143 is not revealed as an important residue.

All Val143 variants except for V143C and V143M retained activity (Table 1). Variants in which Val143 is replaced with charged residues (V143D, V143E, V143K, V143H, and V143R) (group A) and those in which Val143 is replaced with non-bulky hydrophobic or non-bulky polar (V143A, V143G, V143N, V143P, V143Q, V143S, and V143T) (group B) exhibited markedly reduced activity (less than 2% of that of WT) (Table 1, Fig. 7). Considering that Val143 is located in the small loop (Val143-Gly144-Met145) connecting the β sheet (Val135–Thr142) that contains Asp141 of the DEDD motif and the α helix (Pro146–Ser156) (Fig. 1), the decrease in activity in group A might be because the mutation altered the geometry of Arg38, resulting in the decrease in the binding ability of the enzyme to the substrate, and the decrease in activity in group B might be because the mutation increased the flexibility of this loop and altered the geometry of Asp141, resulting in the decrease in catalytic activity.

Variants in which Val143 is replaced with bulky hydrophobic (V143F, V143I, V143L, and V143W) or bulky polar (V143Y) residues at position 143 exhibited moderate activity (14–130%) for the hydrolysis of R1/D18, suggesting that the substitution did not affect the geometry of Asp141. Interestingly, the substitution altered the ratios of R1/D18-hydrolyzing activity to R18/D18-hydrolyzing activity. When the ratio of WT was set as 1, the ratios of V143Y and V143W were 5.6 and 5.5, respectively,

and that of V143Q was 0.2, suggesting the substitution affected the specificity. The alteration observed in V143Y and V143W might be because the bulky side chains caused steric hindrance with the 2'-OH of the sugar moiety of the ribonucleotide at the 5' side of the scissile phosphodiester bond.

Effects of the mutation at position 143 on the salt-dependence of RNase H2 activity – The effects of KCl on the hydrolysis of R1/D18 (Fig. 8) and R18/D18 (Fig. 9) were analyzed. Relative activity was defined as the ratio of the activity to the highest activity. The relative activities of WT and variants were high at 20–50 mM KCl for R1/D18 and R18/D18, indicating that there was no difference in the KCl concentration at which the enzyme exhibited high activity between WT and variants.

Salt-dependence of activity revealed that the magnitude of activation by KCl of all variants examined were 1.3–5 fold more than WT. This could be due to the mutation at position 143 causing unfavorable electrostatic repulsion with the substrate, possibly through changing the geometry of Arg38 and/or Asp141. Neutral salts may alleviate this repulsion to some extent. Taken together, these results indicated that Val143 is not critical but plays a role in determining catalytic activity.

Effects of the mutation at position 143 on the stability of RNase H2 – First, we analyzed the secondary structure of WT and the six variants by CD spectroscopy (Fig. 10). All exhibited negative ellipticities at 200–250 nm. No appreciable changes were observed in each spectrum between WT and variants. Next, we analyzed the stability of WT and six variants by monitoring θ_{222} in the range of 30–70°C (Fig. 11). The melting temperature (T_m) was defined as where the Fraction unfolded (F_u) is 0.5. The T_m values

of WT and all variants were approximately 56ºC, and the differences in T_m values were in the range of 1°C. These results suggested that except for the mutation to Cys or Met, the mutation at position 143 neither caused drastic structural changes nor made drastic reduction in stability.

In this study, all Val143 variants examined exhibited similar secondary structure (Fig. 10) and thermostability (Fig. 11) to WT, indicating that Val143 does not play a role in stability. Val143 is present in the A subunit and is not involved in the association with the B or C subunit thereby limiting its influence on structure and stability. In AGS, more than 50% of total AGS patients have biallelic mutations in one of the three genes encoding RNase H2: 5% for *RNASEH2A*, 36% for *RNASEH2B*, and 12% for *RNASEH2C* (39). The mutation of Val143 has not been observed in AGS. It was reported that a number of recombinant RNase H2 variants bearing AGS-causing mutations exhibited reduced stability and/or hetrotrimer forming ability (10, 19, 28, 34, 46, 47).

According to the genomic analyses of esophageal squamous cell carcinoma (ESCC) cells isolated from 104 patients, the mutation of G427A was found in *RNASEH2A* in chromosome 19, which corresponds to the 359 mutation of V143I in the A subunit of human RNase H2 (50). To elucidate the relationships of the mutations of RNase H2 genes and diseases, further study is required.

Conclusion – We performed saturation mutagenesis analysis of Val143 of the A subunit in human RNase H2. The results revealed that Val143 is not critical for catalytic activity but fine-tunes the activity and specificity of human RNase H2.

Table 1. Activities of Val143 variants.

Val143 variants	Initial reaction rate (s^{-1}) ×1000				A/B[c]
	R1/D18 (A)[a]		R18/D18 (B)[a]		
WT	307 ± 12	100[b]	235 ± 6	100[b]	1.31 (1.0)
V143G	0.237 ± 0.016	0.08	0.0721 ± 0.0039	0.03	3.29 (2.7)
V143A	63.1 ± 2.9	21	19.4 ± 0.7	8.2	3.25 (2.6)
V143L	129 ± 1	42	35.0 ± 0.7	15	3.69 (2.8)
V143I	399 ± 1	130	98.7 ± 3.0	42	4.04 (3.1)
V143F	43.6 ± 3.0	14	14.8 ± 0.2	6.3	2.95 (2.3)
V143Y	97.9 ± 3.3	32	13.3 ± 0.5	5.7	7.36 (5.6)
V143W	79.3 ± 2.8	26	11.2 ± 0.4	4.7	7.08 (5.5)
V143K	0.517 ± 0.009	0.17	0.0673 ± 0.0049	0.03	7.68 (5.7)
V143R	0.153 ± 0.009	0.05	0.0562 ± 0.0009	0.02	2.72 (2.5)
V143H	4.39 ± 0.02	1.4	1.42 ± 0.06	0.60	3.09 (2.3)
V143D	0.401 ± 0.024	0.13	0.286 ± 0.006	0.12	1.40 (1.1)
V143E	0.750 ± 0.020	0.24	0.135 ± 0.005	0.06	5.56 (4.0)
V143N	27.4 ± 1.1	8.9	5.56 ± 0.14	2.3	4.93 (3.9)
V143Q	2.49 ± 0.03	0.81	7.90 ± 0.17	3.4	0.315 (0.2)
V143T	5.55 ± 0.31	1.8	3.87 ± 0.07	1.6	1.43 (1.1)
V143S	0.950 ± 0.130	0.31	0.187 ± 0.001	0.08	5.08 (3.9)
V143P	0.524 ± 0.068	0.17	0.167 ± 0.001	0.07	3.14 (2.4)

[a]The reaction was carried out in 50 mM Tris-HCl buffer (pH 8.0), 5 mM $MgCl_2$, 60 mM KCl, 5.6 nM R1/D18 or 5.6 nM R18/D18 at 25ºC.

[b]Numbers in parentheses indicate values relative to WT.

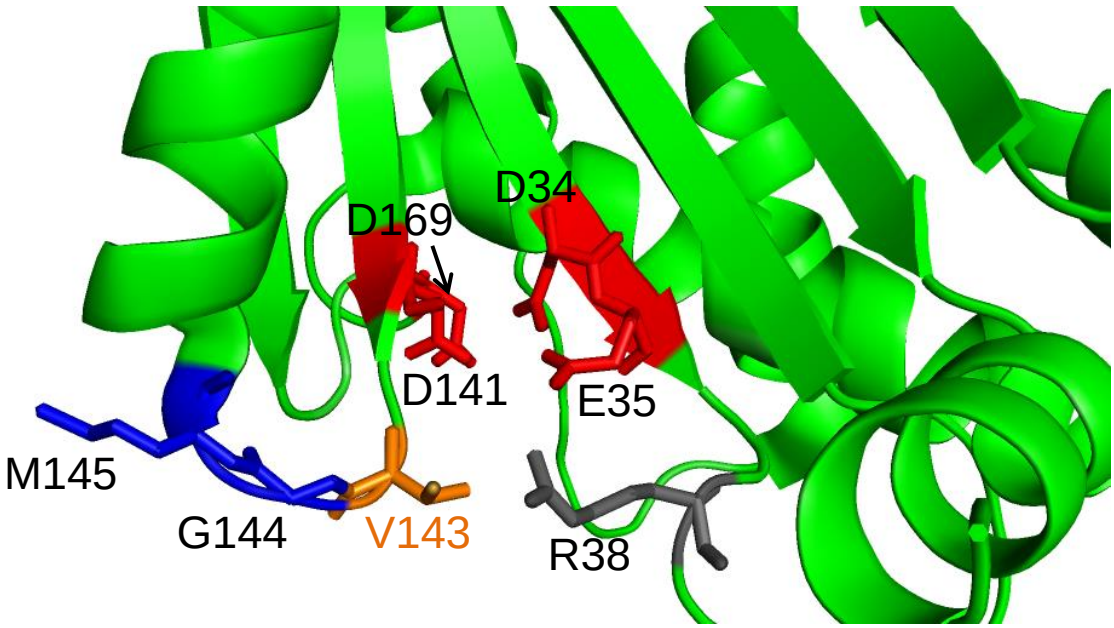

Fig. 1. Close-up view of the active site of human RNase H2. The active site of human RNase H2 (PDB accession no. 3PUF) (48) is shown. Val143, Asp169, and Arg38 are shown in orange, red, and gray, respectively, and Gly144 and Met145 are shown in blue.

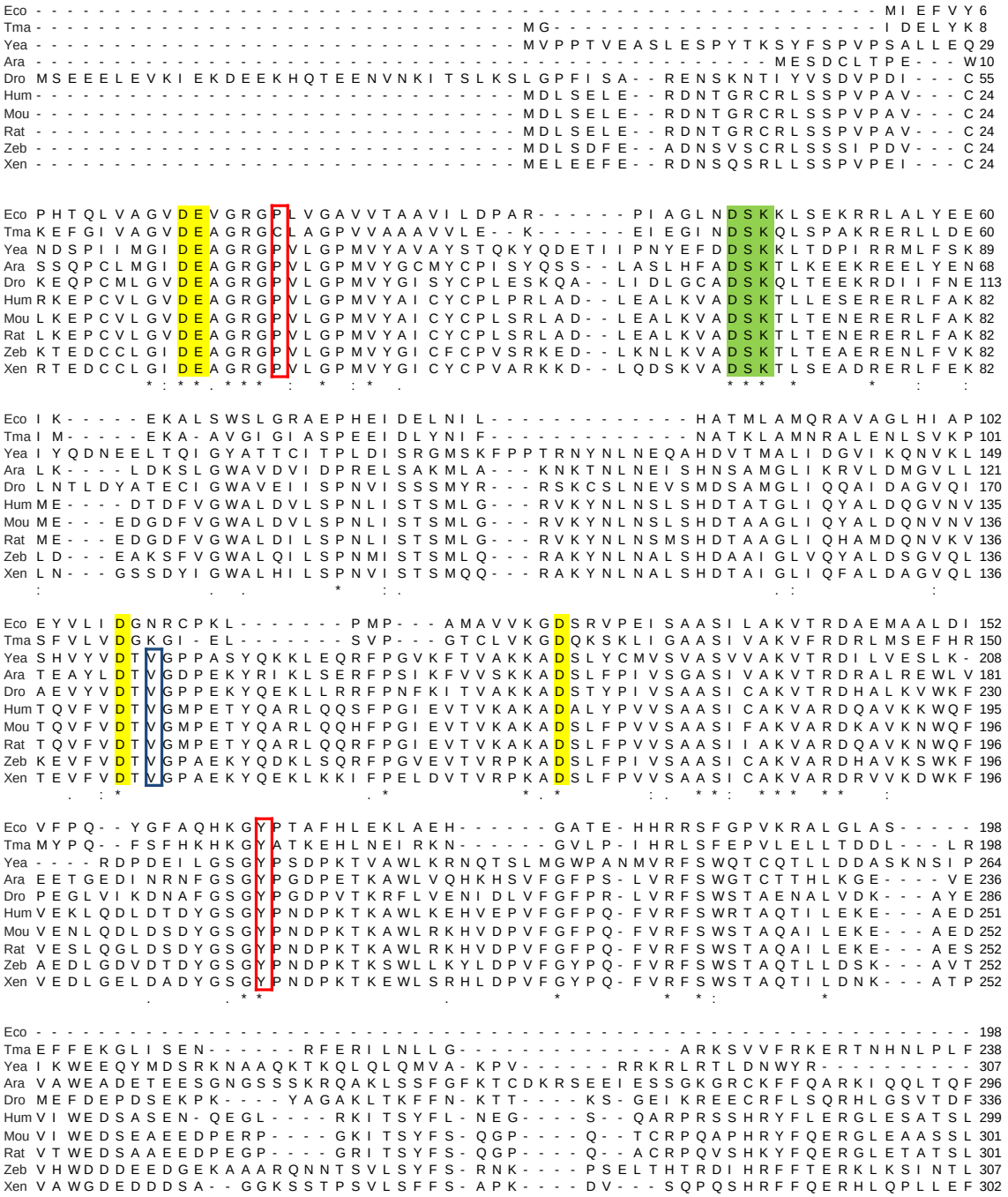

Fig. 2. Amino acid sequences of RNases H2. A multiple sequence alignment was created using Clustal Omega. Eco, *Escherichia coli* (NP_414725.1); Tma, *Thermotoga maritima* (NP_228723.1); Yea, *Saccharomyces cerevisiae* (NP_014327.1); Ara, *Arabidopsis lyrata subsp. lyrata* (XP_002880652.1); Dro, *Drosophila willistoni* (XP_002074967.1); Hum, *Homo sapiens* (NP_006388.2); Mou, *Mus musculus* (NP_081463.1); Rat, *Rattus norvegicus* (NP_001013252.1); Zeb, *Danio rerio* (NP_956520.2); and Xen, *Xenopus laevis* (NP_001180335.1). Residues in the DEDD motif are highlighted in yellow, and those in the DSK motif are in green. The Pro40 and Tyr210 in human RNase H2 and their counterparts are boxed in red, and Val143 of human RNase H2 and its counterparts are boxed in blue.

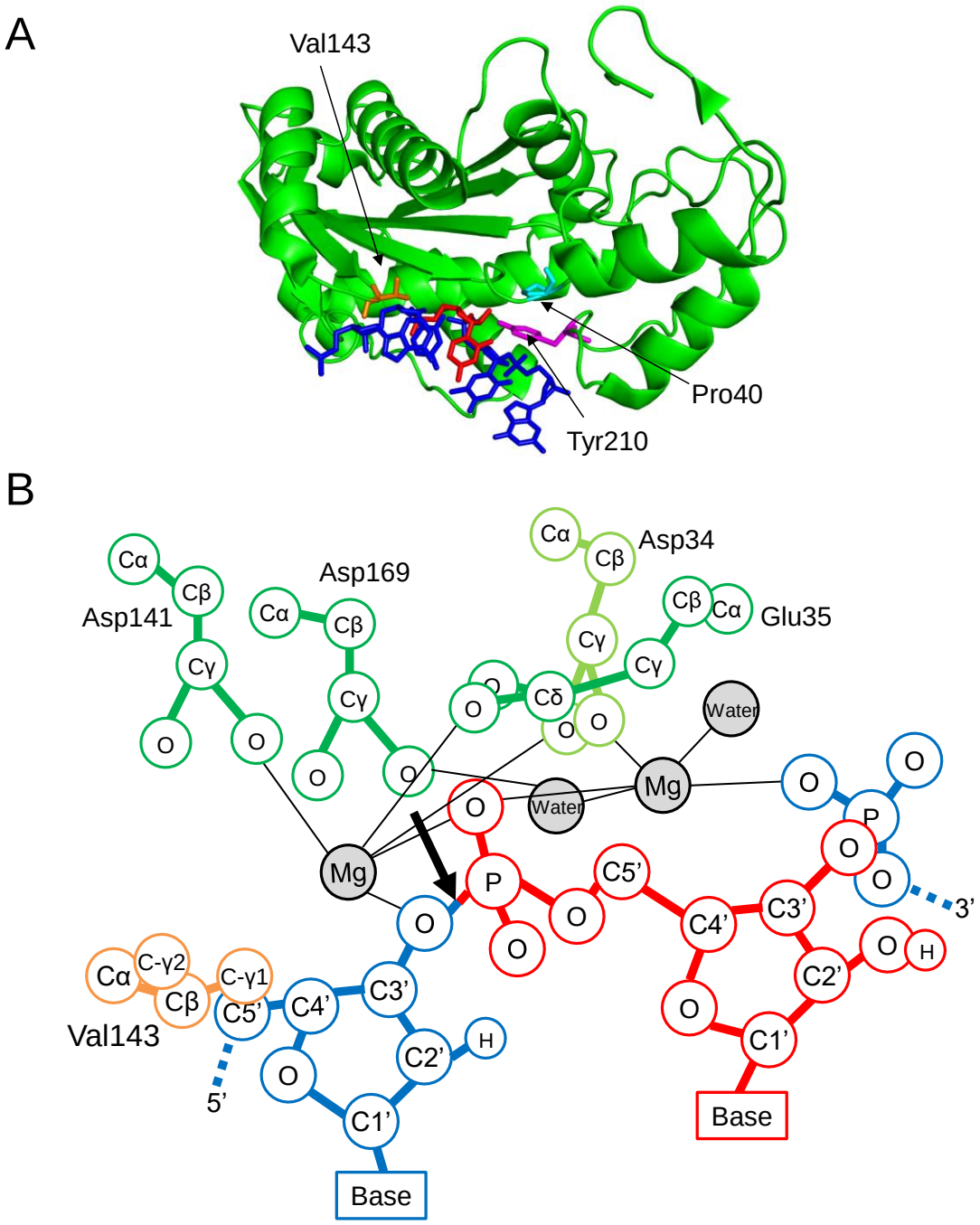

Fig. 3. Modelled structure of the A subunit of human RNase H2 complexed DNA_5-RNA_1-DNA_6/DNA_{12}. (A) Overall structure. The A subunit of human RNase H2 is shown as ribbon in green, and Pro40, Val143, and Tyr210 are shown as sticks in cyan, orange, and magenta, respectively. Deoxyribonucleotide and ribonucleotide in the scissile strand of the hybrid are shown as sticks in blue and red, respectively. Deoxyribonucleotide in another strand of the hybrid is not shown. (B) Close-up view of the active site. The arrow indicates the site of cleavage.

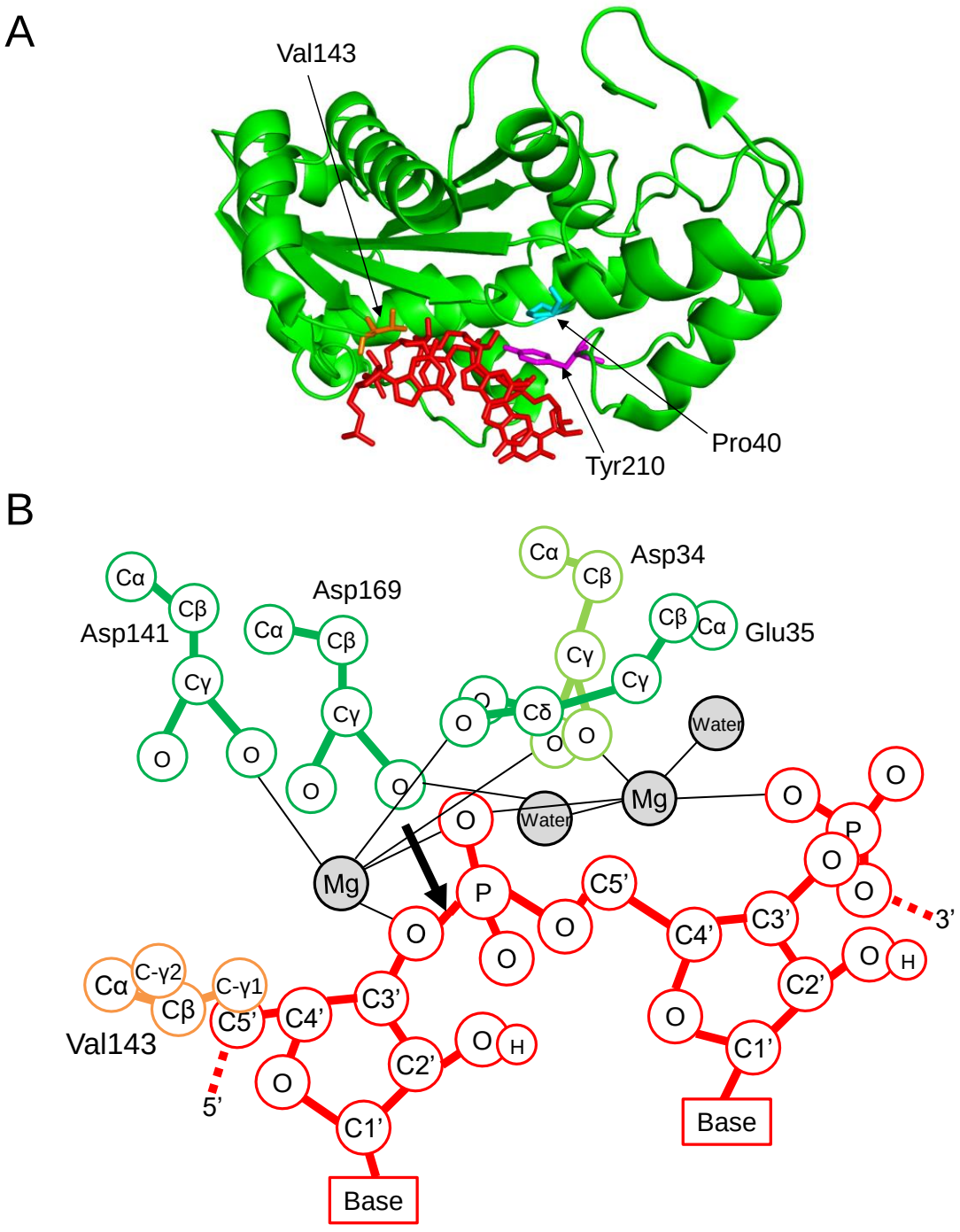

Fig. 4. Modelled structure of the A subunit of human RNase H2 complex with RNA_{19}/DNA_{19}. (A) Overall structure. The colors of the structure correspond to Fig. 3. (B) Close-up view of the active site. The arrow indicates the site of cleavage.

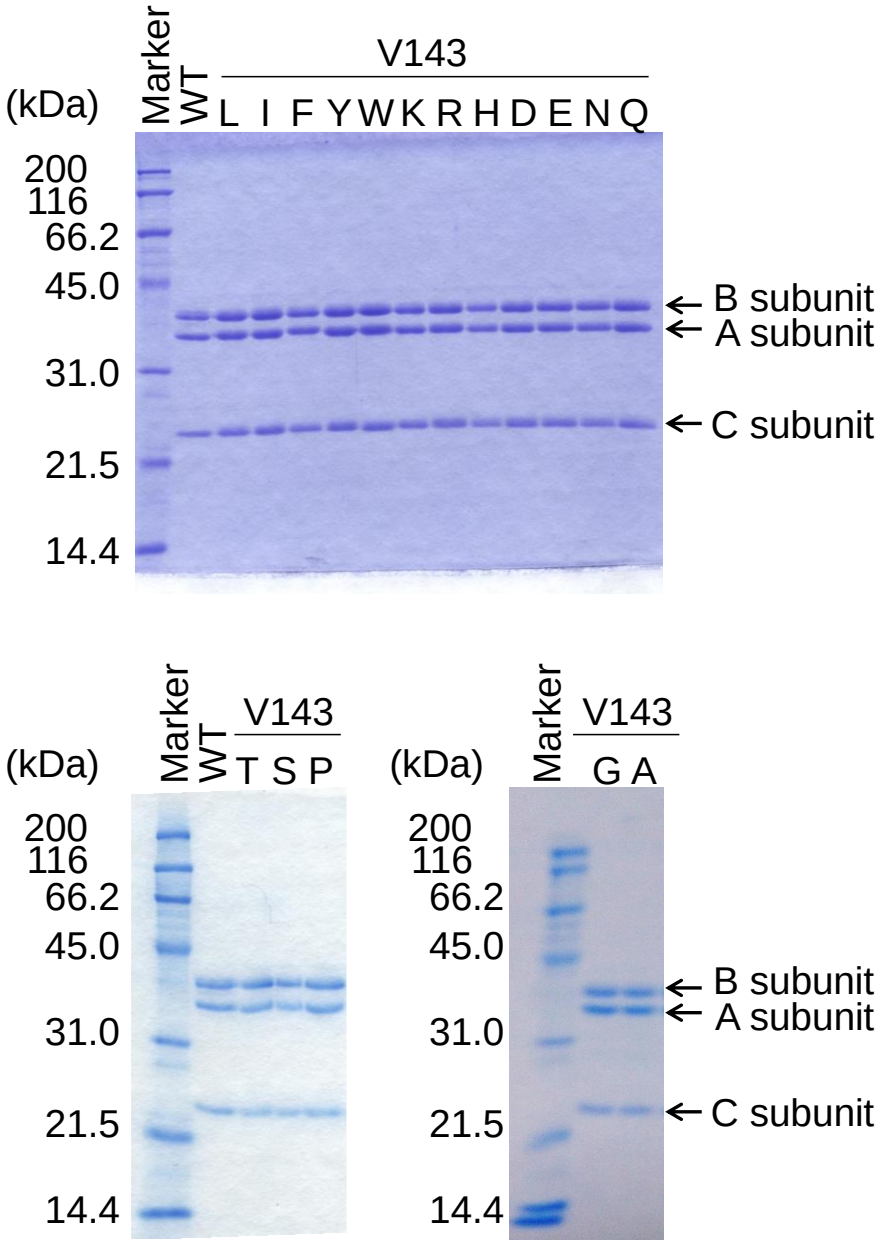

Fig. 5. SDS-PAGE of Val143 variants under reducing conditions. Coomassie Brilliant Blue-stained 12.5% SDS-polyacrylamide gel showing marker proteins (Protein Markers for SDS-PAGE, Nacalai Tesque) and purified enzyme preparations of WT and 17 Val143 variants.

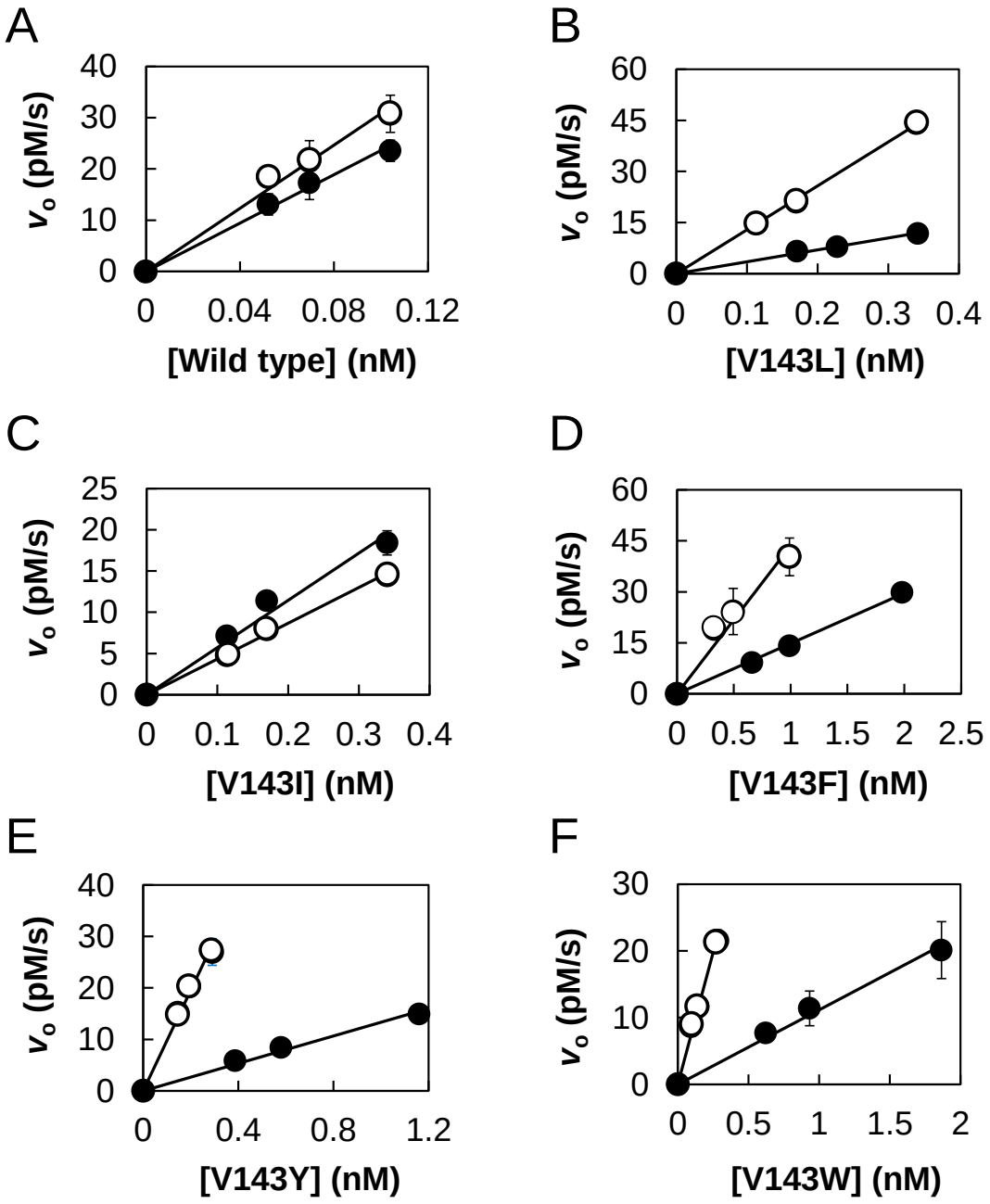

Fig. 6. Comparison of the R1/D18-hydrolytic activity (open circle) with the R18/D18-hydrolytic activity (filled circle) of Val143 variants.

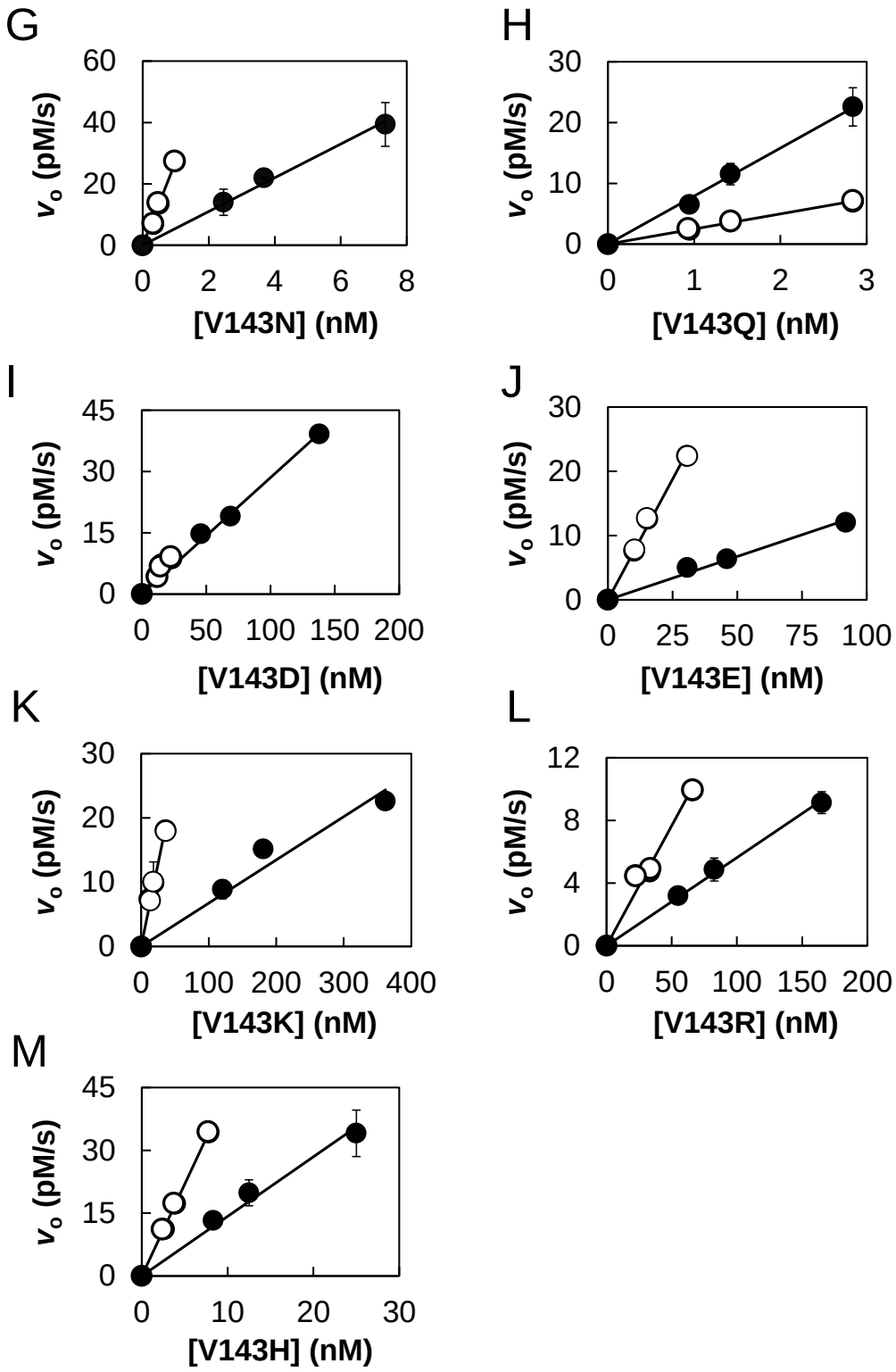

Fig. 6. Comparison of the R1/D18-hydrolytic activity (open circle) with the R18/D18-hydrolytic activity (filled circle) of Val143 variants (continued).

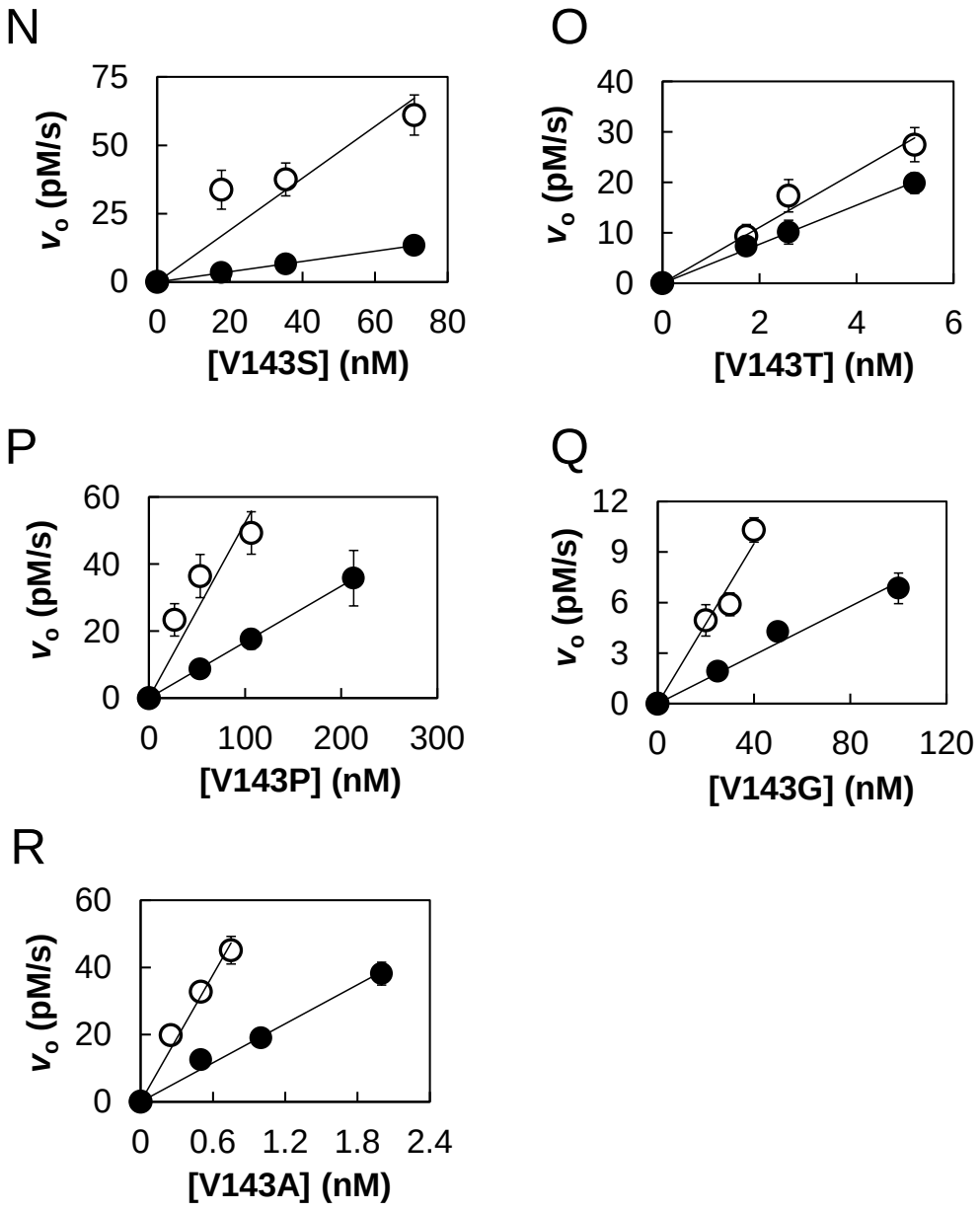

Fig. 6. Comparison of the R1/D18-hydrolytic activity (open circle) with the R18/D18-hydrolytic activity (filled circle) of Val143 variants (continued).

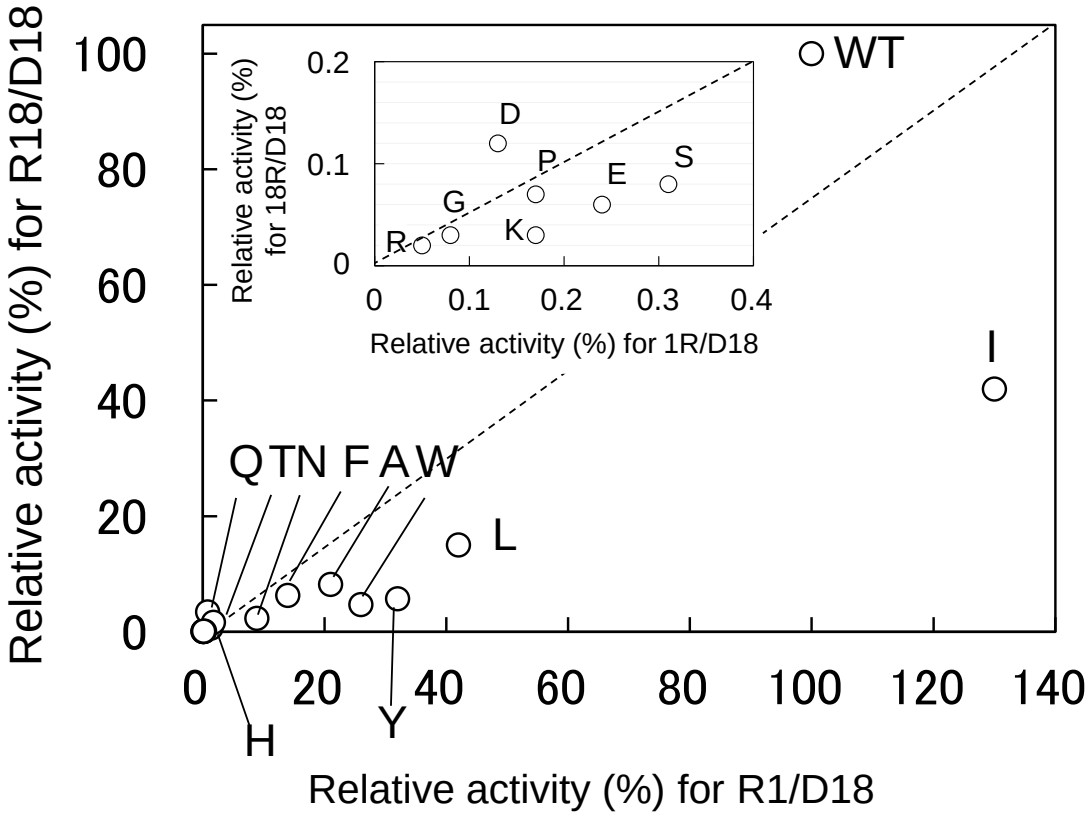

Fig. 7. Comparison of the R1/D18-hydrolytic activity with the R18/D18-hydrolytic activity of Val143 variants. The reaction was carried out in 50 mM Tris-HCl buffer (pH 8.0), 5 mM $MgCl_2$, 60 mM KCl, 5.6 nM R1/D18 or 5.6 nM R18/D18 at 25ºC. Relative activities, which were activities relative to WT, in the hydrolysis of R1/D18 and R18/D18 were plotted.

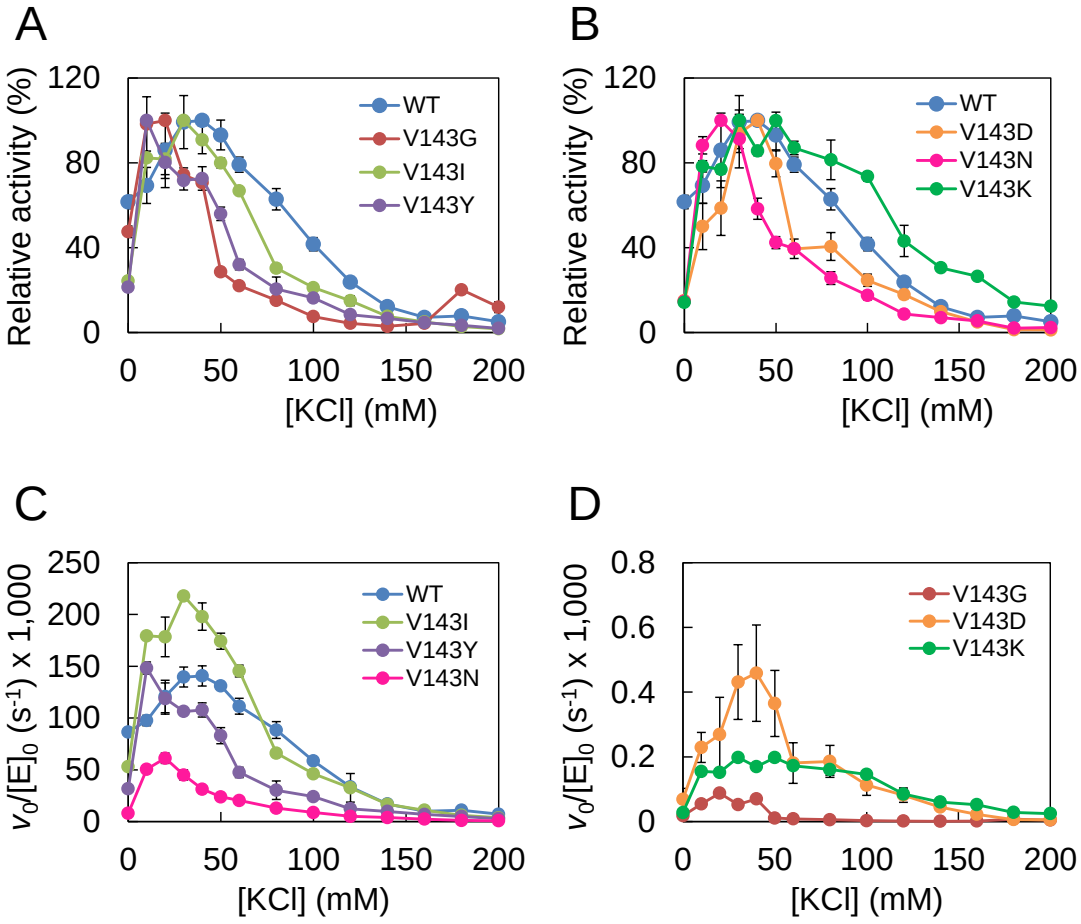

Fig. 8. Dependence of activity of Val143 variants on KCl concentration for R1/D18. The reaction was carried out with 5.6 nM R1/D18 in 50 mM Tris-HCl buffer (pH 8.0), 5 mM $MgCl_2$, 0–200 mM KCl at 25ºC. Relative activity (A, B), which was defined as the ratio of the activity to the highest activity, and the initial reaction rates per enzyme concentration (C, D) against KCl concentration are shown. Error bars indicate SD values of triplicate determination.

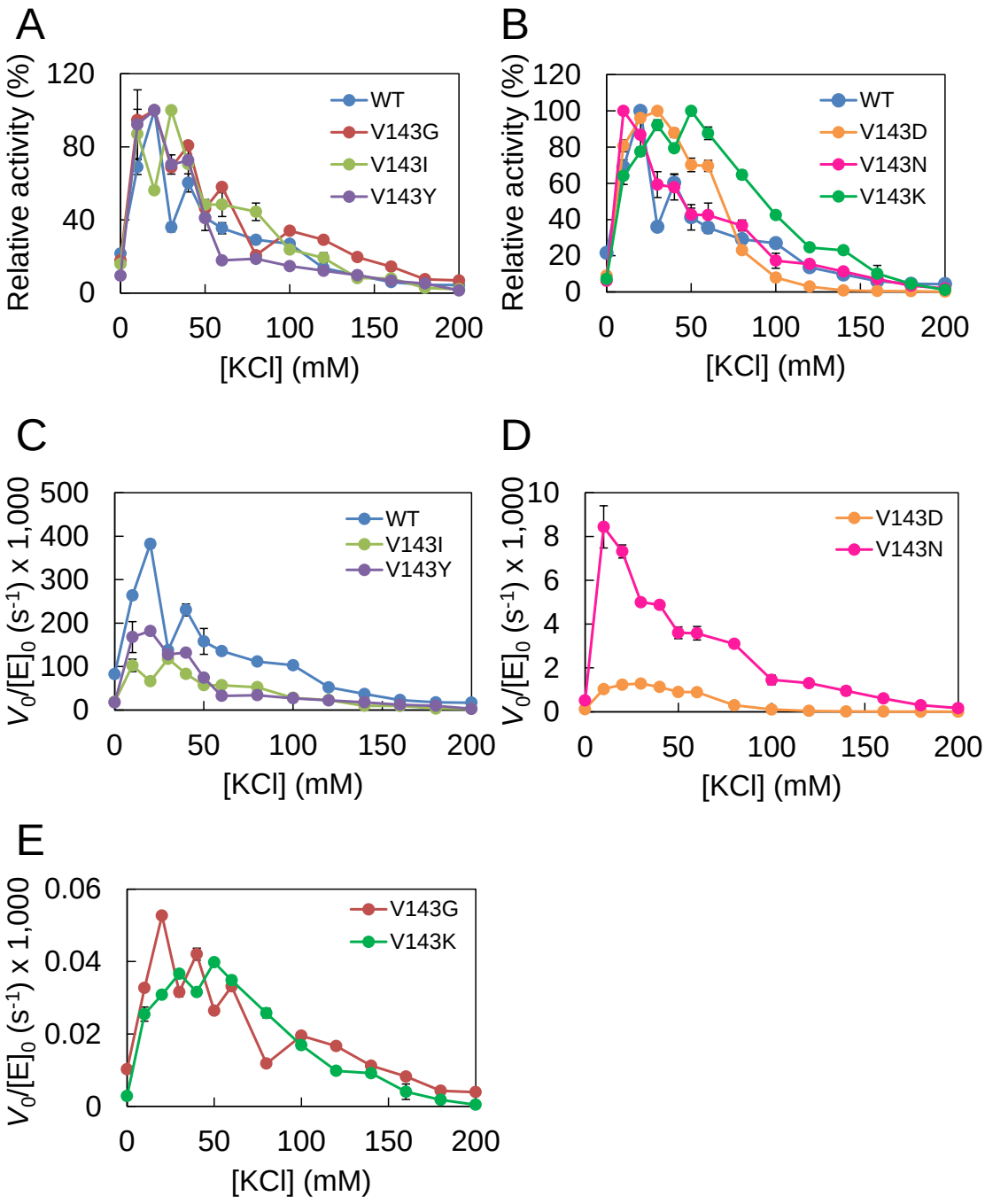

Fig. 9. Dependence of activity of Val143 variants on KCl concentration for R18/D18. The reaction was carried out with 5.6 nM R18/D18 in 50 mM Tris-HCl buffer (pH 8.0), 5 mM $MgCl_2$, 0–200 mM KCl at 25ºC. Relative activity (A, B), which was defined as the ratio of the activity to the highest activity, and the initial reaction rates per enzyme concentration (C–E) against KCl concentration are shown. Error bars indicate SD values of triplicate determination.

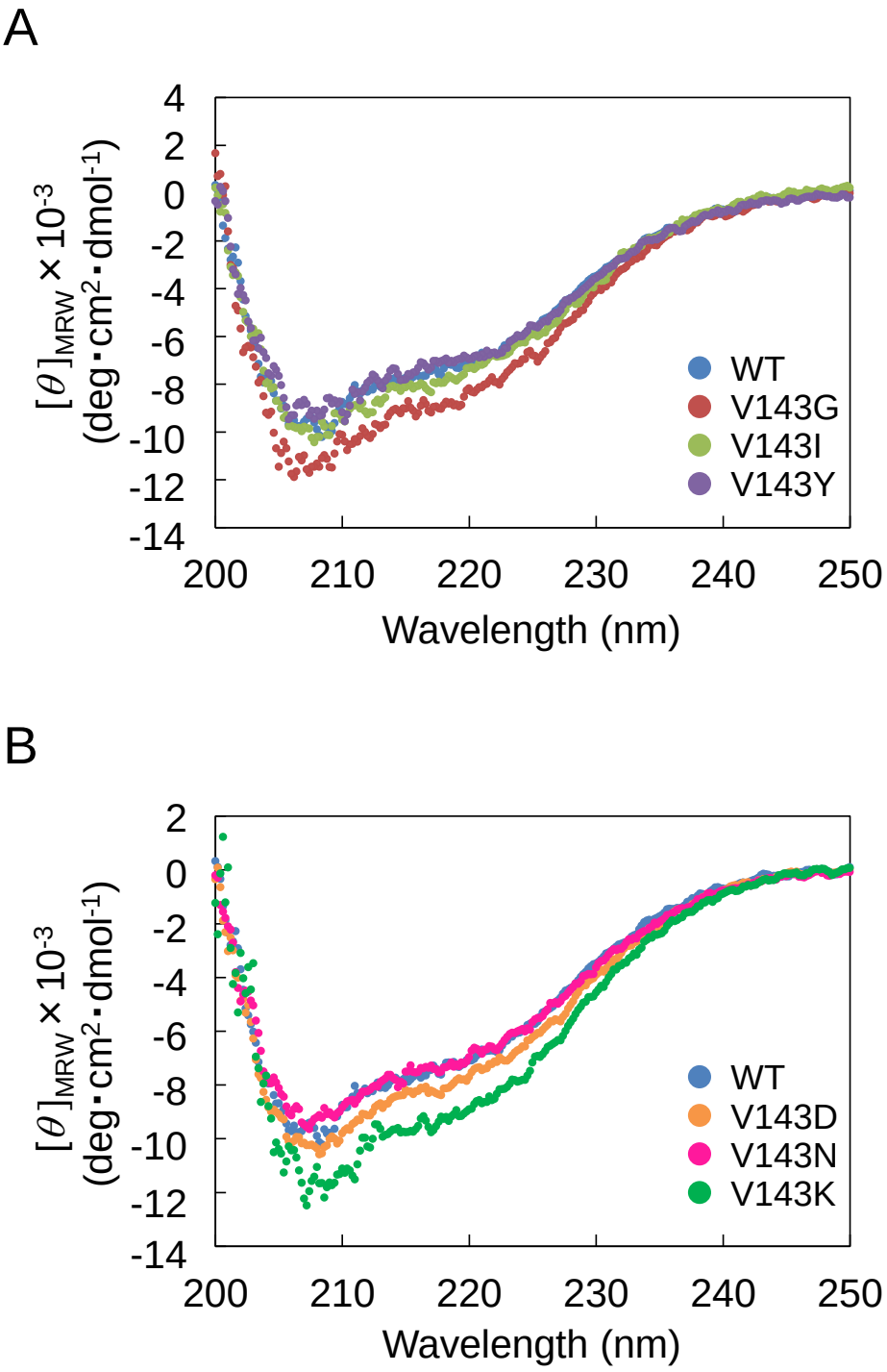

Fig. 10. CD spectra of Val143 variants. The spectra at 200–250 nm were measured in 5 mM Tris-HCl buffer (pH 8.3), 20 mM KCl, 5% glycerol at 25ºC with protein concentrations of 1.0 μM. One of the representative data of duplicate determination is shown.

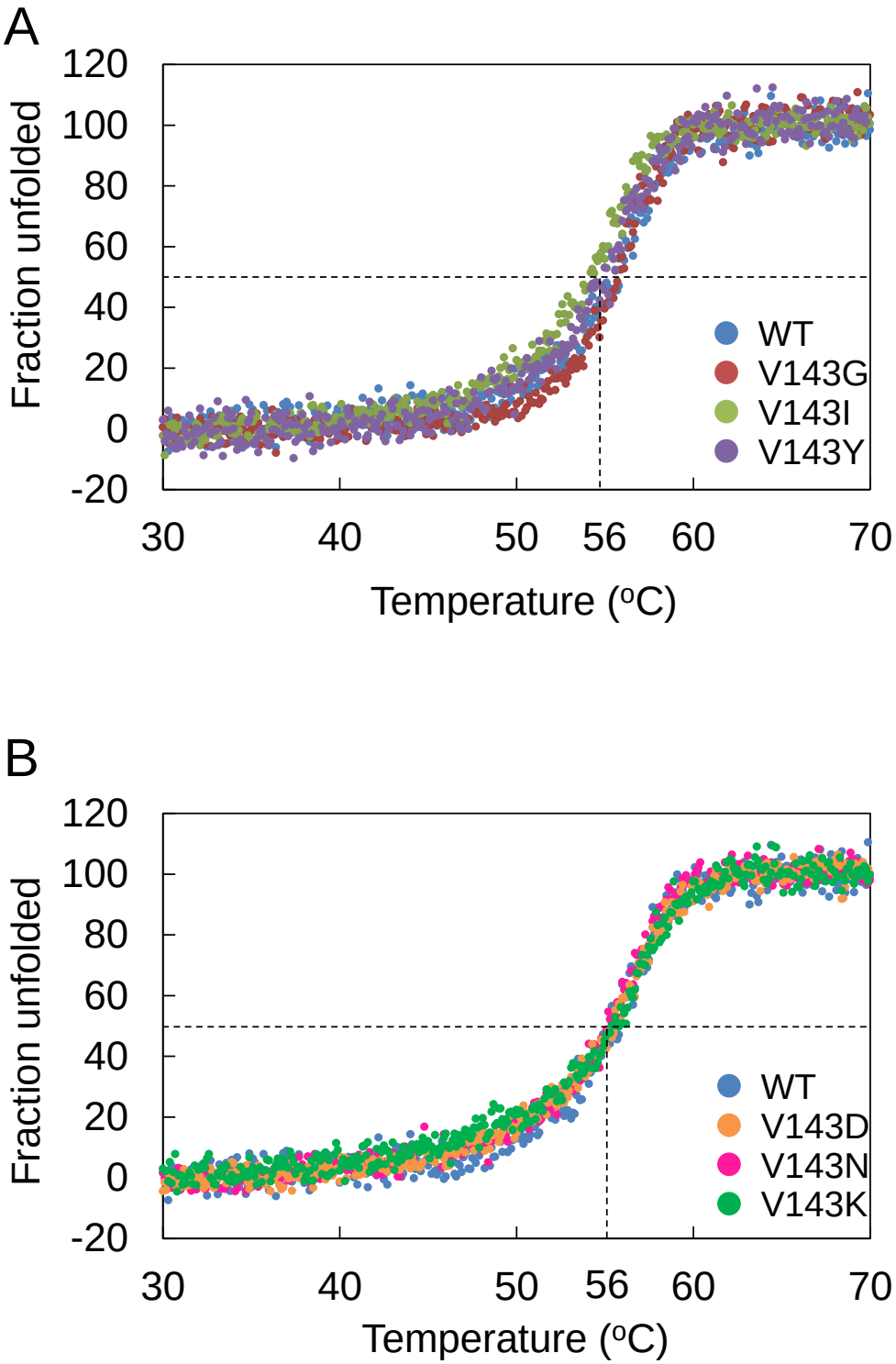

Fig. 11. Thermal denaturation of Val143 variants. θ_{222} of WT and variants were monitored from 30 to 70ºC at 1ºC/min.

Chapter 4

Construction and characterization of RNase H2 knockout NIH3T3 cells

Introduction

As described in General introduction, eukaryotic RNase H2 is composed of three different subunits, one catalytic subunit (A) and two accessory subunits (B and C) (4). In yeast, RNase H2 is not critical for viability, but deletion of the RNase H2 gene enhanced the sensitivity to hydroxyurea (HU), which caused enhanced accumulation of ribonucleotides in genomic DNA and increased number of double strand DNA break (DSB) (51). In mice, RNase H2 knockout caused embryonic death (36, 37). In human, decrease in RNase H2 activity by the mutation of RNase H2 gene causes AGS (8–10).

Originally, DNA polymerase misincorporates ribonucleotides as low as in the order of 10^{-5}. However, the concentration of ribonucleotide is 100-fold higher than that of deoxyribonucleotide in cells, so that ribonucleotide is incorporated at every few thousand base pairs in genomic DNA (52). Such ribonucleotides destabilize genomic DNA due to the presence of reactive 2'-OH group in ribose, leading to DSB. RNase H2 is involved in the removal of ribonucleotides embedded in genomic DNA by the mechanism analogous to maturation of Okazaki fragments. In this mechanism, RNase H2 cuts phosphodiester bonds on the 5'-side of single ribonucleotides, initiating ribonucleotide excision repair (RER) of double-stranded DNA followed by strand displacement synthesis by proliferating cell nuclear antigen (PCNA) and DNA

polymerase, cut-off by flap-structure specific endonuclease 1, and ligation by DNA ligase (6).

When genomic DNA is destabilized, nuclear DNA is released into the cytoplasm. Cyclic GMP-AMP synthase (cGAS)/stimulator of interferon genes (STING) pathway converts the presence of cytosolic DNA into the expression of type I interferons as well as numerous interferon-stimulated genes (ISGs) (53). The products of ISGs play an important role in resisting and controlling pathogens and innate immune response. Recent studies have shown that AGS is the consequence of accumulation of nucleic acids in cells and associated increase in the induction of ISGs, a nucleic acid-sensing cGAS/STING pathway, and innate immune response, and that ISGs expression is a specific indicator of AGS compared to standard inflammatory markers (14, 15). However, the degree of various cellular events might vary depending on cell species. Indeed, characterization of mammalian RNase H2 knockout cell lines remains to be elucidated. To address these issues, in Chapter 4, we generated RNase H2 knockout NIH3T3 cells and characterized them.

Materials and Methods

Materials – NIH3T3 cells were purchased from Cell Resource Center for Biomedical Research, Institute of Development, Aging and Cancer, Tohoku University. [γ-^{32}P]ATP (111 TBq/mmol) and [α-^{32}P]dCTP (111 TBq/mmol) were purchased from PerkinElmer. Oligonucleotides were purchased from Eurofins genomics (Tokyo, Japan) and Fasmac. Protein concentration was determined according to the bicinchoninic acid (BCA) method using Protein Assay Bicinchoninate kit (Nacalai Tesque) with bovine

serum albumin (Nacalai Tesque) as a standard.

Knockout of Rnaseh2a gene – Knockout of *Rnaseh2a* gene was carried out by the method of CRISPR/Cas9 system using Guide-it™ CRISPR/Cas9 System (Green) (Takarabio). The Cas9-sgRNA expression plasmid pGuide-it-ZsGreen1-mRNaseH2A was constructed as follows. The reaction mixture for annealing (10 μl) was prepared by mixing 1 μl of 50 μM oligo-1 5'-CCGGTAACAGATGGCGTAGACCA-3', 1 μl of 50 μM oligo-2 5'-AAACATGGTCTACGCCATCTGTTA-3', and 8 μl of Guide-it Oligo Annealing Buffer, and incubated at 95ºC for 2 min, at room temperature for 10 min, and at 4ºC for 30 min. The reaction mixture for ligation (5 μl) was prepared by mixing of 1 μl of 7.5 μg/μl linearized pGuide-it plasmid, 0.5 μl of 100 nM annealing products, 1 μl of water, and 2.5 μl of DNA Ligation Mighty Mix, incubated at 16ºC for 30 min, and transfected into Stellar^{TM} Competent Cells (Takarabio).

Transfection and cloning were carried out as follows. NIH3T3 cells were cultured to 50% confluency in 500 μl of RPMI 1640 medium containing 10% fetal bovine serum in 12-well microplates in a 5% CO_2 incubator at 37ºC. Then, pGuide-it-ZsGreen1-mRNaseH2A (2.5 μg) was transfected using Xfect Transfection Reagent (Clontech, Mountain View, CA). The cells were cultured for 2 days to 100% confluency and cloned by limiting dilution in 96-well microplates. After 1 month, colonies originating from single cells were transferred to 12-well microplates for expansion.

Screening was carried out as follows. Genomic DNA was prepared from the wild-type NIH3T3 cells (WT cells) or RNase H2 knockout NIH3T3 cells (KO cells) using GenElute Mammalian Genomic DNA Miniprep Kits (Sigma, St. Louis, MO). The

reaction mixture for PCR (50 µl) was prepared by mixing water (33.5 µl), genomic DNA (1 µl), 10×PCR buffer for KOD-Plus-Neo (5 µl), 25 mM $MgSO_4$ (3 µl), 10 µM primer F 5'-GACAAGTGGTTGTTTCCCGATT-3' (1 µl), 10 µM primer R 5'-GGGTGAAAGGGGTGCAGTTTT-3' (1 µl), 2 mM dNTP (5 µl), and 1 U/µl recombinant KOD-Plus-Neo (0.5 µl) (Toyobo, Osaka, Japan). PCR was performed in a 0.2-ml PCR tube for 45 cycles of 10 s at 98°C, 30 s at 60°C, and 30 s at 68°C. The *Nco*I digestion of the PCR products was performed with 1 U *Nco*I at 37°C for 1 h. The products were applied to 1.0% w/v agarose gel and the gel was stained with ethidium bromide (1 µg/ml).

Western blot – Aliquots of 5×10^7 cells were washed with PBS (-) three times and suspended with 1 ml of Cell Lysis Buffer (50 mM Tris-HCl (pH 8.0), 60 mM KCl, 0.1% v/v Triton X-100, 100-fold diluted Protease Inhibitor Cocktail (Nacalai Tesque)). Then, cells were disrupted by sonication. After centrifugation at 20,000 × g for 20 min, the supernatant was collected. Twenty µl of the supernatant was mixed with 4 µl of the SDS-PAGE sample buffer (0.25 M Tris-HCl buffer (pH 6.8), 50% v/v glycerol, 10% w/v SDS, 5% v/v 2-mercaptoethanol, 0.05% w/v bromophenol blue) and was boiled for 10 min. The solution (20 µl) was applied to 12.5% w/v SDS-polyacrylamide gel and was run at 40 mA for 40 min. Pre-stained Protein Markers (Nacalai Tesque) consisting of β-galactosidase (112 kDa), bovine serum albumin (87 kDa), glutamine dehydrogenase (59 kDa), ovalbumin (47 kDa), carbonic anhydrase (33 kDa), myoglobin (27 kDa), and lysozyme (20 kDa) was used for marker proteins. After separation, the proteins were transferred by electroblotting onto a polyvinylidene difluoride (PVDF) membrane Sequi-BlotTM PVDF (BioRad, Hercules, CA) in 25 mM Tris-HCl (pH 8.3)

buffer, 192 mM glycine, 20% v/v methanol at 25 V for 45 min. After blotting, the membrane was washed with 50 mM Tris-HCl (pH 8.3) buffer, 138 mM NaCl, 2.7 mM KCl, 0.05% Tween 20 (TBS-T), blocked with TBS-T containing 5% w/v skim milk, and incubated with anti-mouse β-actin monoclonal antibody (Santa Cruz Biotechnology, Dallas, TX, SC-47778; 1:3000) or mouse anti mouse RNase H2 A subunit monoclonal antibody (Santa Cruz Biotechnology, SC-515475, 1:3000) in TBS-T containing 2.5% w/v skim milk. Then, the membrane was incubated with HRP-conjugated rabbit anti-mouse immunoglobulins (Agilent technologies, Santa Clara, CA, P0260, 1:3000). After washing with TBS-T for three times, the protein bands were visualized using a Peroxidase Stain Kit (Nacalai Tesque).

RNase H2 assay – The kinase reaction (20 µl) was carried out with 10 units/µl T4 polynucleotide kinase (Toyobo), 100 µM 12-nt RNA 5'-gacaccugauuc-3' (R12) or 100 µM DNA_5-RNA_1-DNA_6 5'-GACACcTGATTC-3' (R1), and [γ-^{32}P]ATP (370 MBq/ml; 111 Bq/pmol) at 37°C for 45 min. An RNA_{12}/DNA_{12} hybrid (named R12/D12) was prepared by incubating 16 µl of 2.5 µM 5'-[^{32}P]-labelled R12 and 4 µl of 10 µM unlabeled complementary 12-nt DNA 5'-GAATCAGGTGTC-3' (D12) in water at 70ºC for 4 min. A hybrid consisting of DNA_5-RNA_1-DNA_6 and DNA_{12} (named R1/D12) was prepared similarly by using 5'-[^{32}P]-labelled R1 instead of 5'-[^{32}P]-labelled R12. The RNase H reaction (7.5 µl) was carried out with indicated concentrations of the extracts of the WT or KO cells and 200 nM R12/D12 or R1/D12 in 50 mM Tris–HCl (pH 8.0) buffer containing 60 mM KCl and 5 mM $MgCl_2$ at 25ºC for indicated time. Then, the reaction was stopped by adding 4 µl of sample-loading buffer (10 mM EDTA, 90% v/v formamide, 1 mg/ml xylene cyanol FF, 1 mg/ml bromophenol blue). The resulting

solution (1 µl) was applied to denaturing 20% polyacrylamide gel and was run in 89 mM Tris-HCl (pH 8.0), 89 mM boric acid, 2 mM EDTA at 30 W for 5 h. After the electrophoresis, the gel was analyzed by a Typhoon FLA 9500 (GE Healthcare) using the program ImageQuant TL (GE Healthcare).

Alkaline hydrolysis of genomic DNA – Genomic DNA was prepared from the WT or KO cells using GenElute Mammalian Genomic DNA Miniprep Kits (Sigma). The reaction mixture for alkaline hydrolysis (26 µl) was prepared by mixing 0.25 µg/µl genomic DNA (20 µl) and 1 M KOH (6 µl). After the reaction at 55ºC for 2 h, 4 µl of alkaline sample-loading buffer (300 mM KOH, 6 mM EDTA, pH 8.0, 18 % glycerol, 0.15 % bromocresol green, 0.25 % xylene cyanol FF) was added. The solution (25 µl) was applied to 1% w/v alkaline agarose gel (50 mM NaOH, 1 mM EDTA) and was run at 30 V for 13 h. After the electrophoresis, the gel was neutralized in 1 M Tris-HCl buffer (pH 7.6) containing 1.5 M NaCl for 2 h, 2 times and stained with SYBR Gold (Thermo Fisher Scientific, Waltham, MA) diluted 10000-fold with 1 × TAE.

Nick translation assay – The mixture for RNase H reaction (50 µl) was prepared by mixing 0.5 U *E. coli* RNase HII (New England BioLabs, Ipswich, MA) (1 µl), 8.8 µg of genomic DNA of the WT or KO cells, 10 × ThermoPol Buffer (5 µl) and water (up to 50 µl). The reaction was carried out at 37ºC for 150 min. The reaction mixture for DNA polymerization (20 µl) was prepared by mixing 5 U *E. coli* DNA polymerase I (Takarabio) (0.8 µl), the products of the RNase H reaction (5 µl of 40 ng/µl), 10 × *E. coli* DNA polymerase I Buffer (2 µl), dNTP mix solution (0.2 mM dATP, dTTP, and dGTP each) (2 µl), 1 µl of [α-^{32}P]dCTP (370 MBq/ml; 111 kBq/pmol), and water (9.2

µl). After the reaction at 15ºC for 35 min, the reaction was stopped by heat treatment at 70ºC for 10 min. Two µl of sample-loading buffer was added to 10 µl of the reaction solution. The resulting solution (12 µl) was applied to 1% w/v agarose gel and was run at 100 V for 120 min. After the electrophoresis, the gel was analyzed by a Typhoon FLA 9500 (GE Healthcare) as described above.

MTT assay – WT or KO cells were cultured in 96-well microplates (5×10^3 cells/ml, 100 µl/well). The growth of NIH3T3 cells was measured by the MTT (3-(4,5-dimethylthiazol-2-yl)-2,5-diphenyl tetrazolium bromide) assay using MTT Cell Count Kit (Nacalai Tesque). MTT solution and color development solution were added to the culture at indicated time points. The absorbance at 470 nm was measured with EnSight (PerkinElmer) with the reference of 650 nm.

Real-time quantitative PCR – Total RNA was isolated from NIH3T3 using NucleoSpin® RNA Plus (Takarabio). cDNA synthesis reaction was carried out using ReverTra Ace® qPCR RT Master Mix with gDNA Remover (Toyobo). Real-time quantitative PCR (qPCR) was performed using TB Green™ Premix Ex Taq™ II (Tli RNaseH Plus) (Takarabio) with a pair of oligonucleotides listed in Table 1 as primers in a 0.2-ml 96 well plate. The reaction was carried out at 95°C for 30 s followed by 40 cycles of 5 s at 95°C and 30 s at 60°C in PCR Thermal Cycler Dice Real Time System Single (Takarabio). Relative expression was calculated by ΔΔCt method using HPRT (hypoxanthine phosphoribosyltransferase) as a control for data normalization.

Results and Discussion

Knockout of RNase H2 subunit A gene – RNase H2 is composed of three different subunits, one catalytic subunit (A) and two accessory subunits (B and C). We searched a target sequence where Cas9 cleaves double-stranded DNA using CRISPRdirect (https://crispr.dbcls.jp/) and the nucleotide sequence of the subunit A (accession number NM_027187). We selected exon 2 of the subunit A gene because it shows minimal off-target potentials and has CCCATGG comprising the PAM sequence (CCC) and the *Nco*I recognition site (CCATGG) at the 5' terminus (Fig. 1A). A plasmid for the expression of sgRNA and Cas9 was constructed (Fig. 1B).

After the transfection and cloning, four independent clones were obtained. The 356-bp fragment containing the entire exon 2 (72 bp) was amplified from the genomic DNA in the PCR with a primer combination of primer F and primer R. Figure 2A shows nucleotide sequence of the fragment amplified from the WT cells. It has the *Nco*I recognition site at the position 187. Figure 3A shows the analysis of agarose gel electrophoresis of the *Nco*I-untreated or treated fragments amplified from the WT cells or clones 1–4. In the WT and clones 2 and 3, around 170 bp-band was detected, which was thought to be the overlapping two fragments (187 and 165 bp). In clones 1 and 4, only around 350 bp-band was detected, suggesting that they were homo *Nco*I site-deleted clones. Sequence analysis revealed that clone 1 lacked one nucleotide ^{191}G, and clone 4 lacked 16 nucleotides corresponding to ^{176}CTACCAAGGTCCCAT^{191}G (Fig. 3B). We selected clone 4 for the subsequent analysis.

We examined the expression of the RNase H2 A subunit. Cellular extracts of the WT and KO cells were applied to SDS-PAGE followed by western blot with a

combination of anti-RNase H2A antibody and anti-β-actin antibody (Fig. 2B). In the WT cells, a 35-kDa protein band corresponding to the RNase H2 A subunit and a 45-kDa one corresponding to β-actin were detected. In the KO cells, the former was not detected, but the latter was detected, indicating that the KO cells did not express the RNase H2 A subunit.

Effects of knockout of RNase H2 gene on cell morphology and protein expression – Microscopic analysis showed that the size and shapes of the WT and KO cells were similar (Fig. 4). Two-dimensional gel electrophoresis of the cell lysates revealed that the patterns of protein spots of the WT and KO cells were similar (Fig. 5). These results indicated that knockout of RNase H2 had little effect on total protein expression.

Effects of knockout of RNase H2 gene on the RNase H activity – The RNase H activity of the extracts of the WT or KO cells was examined by a radioisotope-based RNase H2 assay. We first investigated the single ribonucleotide excision activity. An RNA/DNA hybrid (R1/D12) consisting of a 5'-[^{32}P]-labelled DNA_5-RNA_1-DNA_6 (R1) and an unlabeled complementary DNA (D12) was used as the substrate. Figure 6A and B show the denatured PAGE analysis of the products obtained from the reaction under various conditions. Unreacted R1/D12 showed a 12-nt band (lane 0 in Fig. 6A and B). When R1/D12 was incubated with recombinant human RNase H2, the 12-nt band was not detected, and the 5-nt band was detected (lane P in Fig. 6A and B), indicating that RNase H2 hydrolyzed the 5'-phosphodiester bonds of the ribonucleotide of R1. When R1/D12 was incubated with various amounts of the extracts of the WT cells for 10 min, the 5-nt band was detected at the protein amounts of 600 and 3,000 ng (lanes 6 and 7 of

WT in Fig. 6A). When R1/D12 was incubated with the extracts of the KO cells, the 5-nt band was not detected at all protein amounts examined (lanes 1–7 of KO in Fig. 6A). When R1/D12 was incubated with the extracts of the WT cells at 1,400 ng for 1.25–80 min, the 5-nt band increased with increasing time (lanes 1–7 of WT in Fig. 6B). When R1/D12 was incubated with the extracts of the KO cells, the 5-nt band was not detected at all time points examined (lanes 1–7 of KO in Fig. 6B). These results indicated that the WT cells had the single ribonucleotide excision activity, while the KO cells did not.

We next investigated the RNA strand degrading activity. An RNA/DNA hybrid (R12/D12) consisting of a 5'-[^{32}P]-labelled RNA_{12} (R12) and an unlabeled complementary DNA (D12) was used as the substrate. Figure 6C and D show the results. Unreacted R12/D12 showed a 12-nt band (lane 0 in Fig. 6C and D). When R12/D12 was incubated with recombinant human RNase H2, the 12-nt band was not detected, and multiple smaller bands were detected (lane P in Fig. 6C and D), indicating that RNase H2 hydrolyzed the 5'-phosphodiester bond of the ribonucleotide at multiple positions. When R12/D12 was incubated with various amounts of the extracts of the WT cells for 10 min, smaller bands were detected at the protein amounts of 600 and 3,000 ng (lanes 6 and 7 of WT in Fig. 6C). The same results were obtained for the KO cells (lanes 6 and 7 of KO in Fig. 6C). When R12/D12 was incubated with 1,400 ng of the extracts of the WT cells for 1.25–80 min, smaller bands were detected at 20, 40, and 80 min (lanes 5–7 of WT in Fig. 6D). The same results were obtained for the KO cells again (lanes 6 and 7 of KO in Fig. 6D). These results indicated that both WT and KO cells had the RNA strand degrading activity.

Effects of knockout of RNase H2 gene on the amounts of ribonucleotides

incorporated in the genomic DNA – We examined the amounts of ribonucleotides incorporated in the genomic DNA of the WT and KO cells. First, we examined the effect of the alkaline treatment of genomic DNA. The effect was assessed by the alkaline agarose gel electrophoresis analysis of the alkaline-treated genomic DNA (Fig. 7A). Densitometry of DNA fragment distribution revealed that genomic DNA of the KO cell exhibited increased mobility compared to that of the WT cells (Fig. 7B), indicating that the size of genomic DNA of the KO cells was made smaller by the alkaline treatment than that of the WT cells.

We next examined the effect of the recombinant *E. coli* RNase H treatment of genomic DNA. The effect was assessed by DNA polymerase I-dependent nick translation in the presence of α[^{32}P]-dCTP with the RNase H-treated genomic DNA as the template, followed the agarose gel electrophoresis analysis of the reaction products (Fig. 7C). When genomic DNA of the KO cells was treated with RNase H, clear band was detected, corresponding to the products of nick translation. When it was not treated, such band was not detected. Whether genomic DNA of the WT cells was treated or not, such band was not detected. These two results with the alkaline- and RNase H-treatments of genomic DNA suggest that the KO cells had more ribonucleotides incorporated in genomic DNA than the WT cells.

Effects of knockout of RNase H2 gene on the cell growth – We examined the growth of the WT and KO cells by MTT assay. Figure 8 shows the absorbance at 570 nm (A_{570}) of the culture medium to which MTT reagent was added at indicated time points. A_{570} increased with time and reached the highest at day 3 in the WT cells and at day 6 in the KO cells (Fig. 8A), indicating that the growth rate of the KO cells was

lower than that of the WT cells. The slopes of the line expressing the $\log_2$ (A_{570}) values (y) at day x of the WT and KO cells were 1.4 and 0.8 (Fig. 8B), suggesting that the growth rate of the KO cells was 60% of that of the WT cells.

Mouse embryonic fibroblasts (MEFs) isolated from the *Rnaseh2b*$^{-/-}$ *p53*$^{+/+}$ mice did not grow, whereas those from the *Rnaseh2b*$^{-/-}$ *p53*$^{-/-}$ mice exhibited proliferation (36). The growth rate of the *Rnaseh2b*$^{-/-}$ *p53*$^{-/-}$ mice MEFs was 64% of that of the *Rnaseh2b*$^{+/+}$ *p53*$^{-/-}$ mice MEFs (36). This was similar to our results for the KO and WT cells (Fig. 8). Human liver HeLa cells in which RNase H2 was knocked down by RNA interference exhibited an accumulation of the cells in the S and G2-M phases (54).

Effects of knockout of RNase H2 gene on the expression of interferon-stimulated genes (ISGs), and cGAS/STING genes – We examined the expression of ISGs and cGAS/STING genes of the WT and KO cells by qPCR (Fig. 9). Genes for interferon-induced proteins with tetratricopeptide repeats (IFIT1, IFIT2, and IFIT3), interferon regulatory factor 7 (IRF7), and CC-X-C motif chemokine 10 (CXCL10) were selected because they are the most abundantly expressed and well characterized in AGS (14, 53). The KO cells exhibited 2.7- and 1.8-fold higher expression of IFIT3 and IRF7 genes and 2.2-fold lower expression of CXCL10 genes than the WT cells. There were no difference in the expression of IFIT1, IFIT2, cGAS, and STING genes.

The levels of IFIT3 and IRF7 mRNA expression in the KO cells were 2.7- and 1.8-fold higher, respectively, than those of corresponsive expression in the WT cells (Fig. 9). It is suggested that elevated amounts of ribonucleotides incorporated in the genomic DNA increased the levels of IFIT3 and IRF7 mRNA expression. However, when MEFs isolated from tamoxifen-inducible RNase H2 knockout mice were cultured

in the presence of tamoxifen, the levels of IFIT3 and IRF7 mRNA expression were 40-fold higher than those of corresponsive expression in control MEFs (38). Therefore, we assume that the knockout of RNase H2 gene moderately increase the expression of ISGs. These MEFs also depicted AGS-related cellular events such as accumulation of micronuclei in the cytoplasm and activation of a cGAS/STING pathway (38). In this study, however, the levels of cGAS and STING mRNA expression in the KO cells were almost the same to those of corresponsive expression in the WT cells (Fig. 9). When these MEFs were forced into a G0 stage by serum starvation, such AGS-related cellular events disappeared (55). When astrocytes isolated from neuron-specific RNase H2 knockout mice were cultured under mitogenic conditions, the cells exhibited AGS-related cellular events (55). Such events were not observed in the brains of the neuron-specific RNase H2 knockout mice (55). The RNase H2 knockout human kidney HEK293T and liver HeLa-HA cells did not depict AGS-related cellular events; however they showed an abolishment of retroelement propagation (38). Together with other previous reports (12, 37, 56, 57), these results clearly show that the accumulation of ribonucleotides in genomic DNA is closely related to the absence of RNase H2. However, the degree of various subsequent AGS-related cellular events varies depending on the presence or absence of p53 in the cell, cell species, cell cycle, and environment in which the cells are located.

Conclusion – The RNase H2 gene knockout NIH3T3 cells lacked the activity to hydrolyze single ribonucleotides in DNA duplex, contained more ribonucleotides in genomic DNA than the WT cells, and exhibited retarded cell growth. However, they did not exhibit several tens of times higher expression of ISGs as observed in the MEFs

isolated from inducible RNase H2 knockout mice. Our results suggest that an accumulation of ribonucleotides in genomic DNA is closely related to the absence of RNase H2, but the degree of various subsequent cellular events varies depending on various factors.

Table 1. Primer sequences.

Primers	Sequences (5'-3')
mHPRT_fw	TCAGTCAACGGGGGACATAAA
mHPRT_rev	GGGGCTGTACTGCTTAACCAG
mIRF7_fw	ATGCACAGATCTTCAAGGCCTGGGC
mIRF7_rev	GTGCTGTGGAGTGCACAGCGGAAGT
mIFIT1_fw	GAACCCATTGGGGATGCACAACCT
mIFIT1_rev	CTTGTCCAGGTAGATCTGGGCTTCT
mIFIT2_fw	ATGAGTTTCAGAACAGTGAGTTTAA
mIFIT2_rev	AACTGGCCCATGTGATAGTAGACCC
mCXCL10_fw	GCCGTCATTTTCTGCCTCA
mCXCL10_rev	CGTCCTTGCGAGAGGGATC
mIFIT3_fw	TGGCCTACATAAAGCACCTAGATGG
mIFIT3_rev	CGCAAACTTTTGGCAAACTTGTCT
mSTING_fw	AAATAACTGCCGCCTCATTG
mSTING_rev	ACAGTACGGAGGGAGGAGG
mcGAS_fw	GAGGCGCGGAAAGTCGTAA
mcGAS_rev	TTGTCCGGTTCCTTCCTGGA

The sequences of mHPRT_fw and mHPRT_rev are from PrimerBank (https://pga.mgh.harvard.edu/ primerbank/), and those of other primers are from Ref. 36.

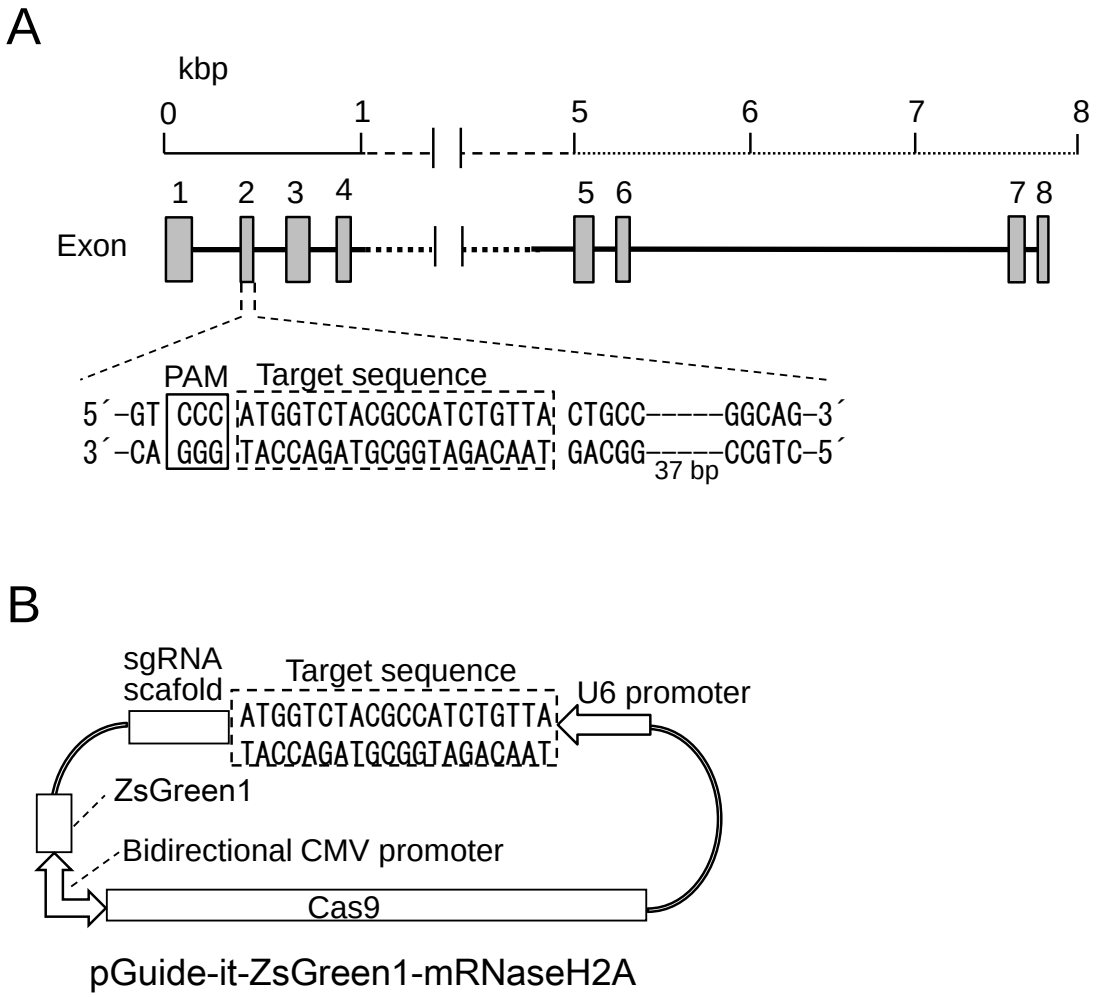

Fig. 1. Knockout of *Rnaseh2a* gene with the CRISPR/Cas9 system. (A) Target site in the *Rnaseh2a* gene coding RNase H2 A subunit. (B) Plasmid for the expression of sgRNA and Cas9. The PAM and target sequences are indicated by a box with solid and dashed lines, respectively.

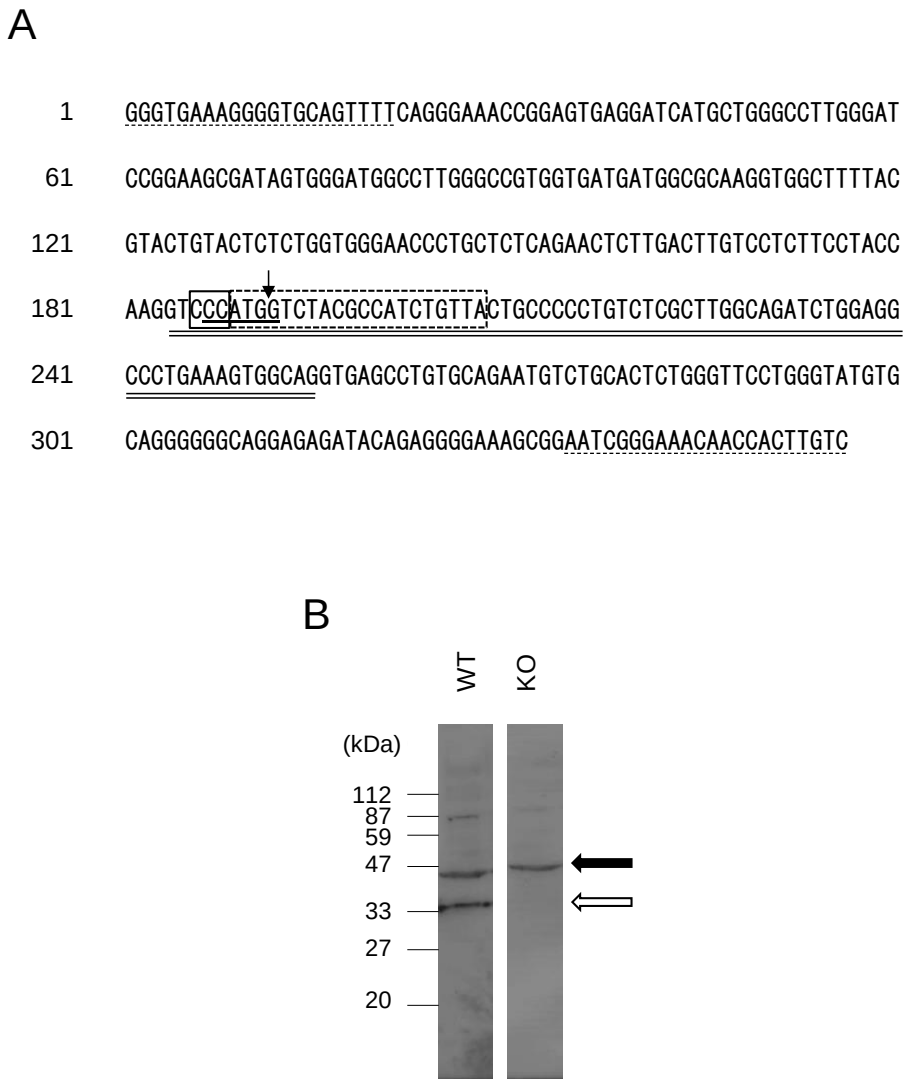

Fig. 2. Screening of *Rnaseh2a*$^{-/-}$ homozygote NIH3T3 cells. (A) Nucleotide sequence of the PCR product amplified from the genomic DNA of the wild-type NIH3T3 (WT) cells with a primer combination of primer F and primer R. The PAM and target sequences are indicated by a box with solid and dashed lines, respectively. The *Nco*I recognition site, primer binding sites and nucleotide sequences of the exon 2 are indicated by solid, dashed and double underlines, respectively. The solid arrow indicates the Cas9 cleavage site. (B) Western blot. Cellular extracts of the WT and KO cells were applied to 12.5% w/v SDS-polyacrylamide gel. After transferring the protein onto a PVDF membrane, it was incubated with mouse anti-β-actin and mouse anti-RNase H2 A subunit as a primary antibody and HRP-conjugated rabbit anti-mouse as a secondary antibody. The open and solid arrows indicate the bands corresponding to RNase H2 A subunit and β-actin, respectively.

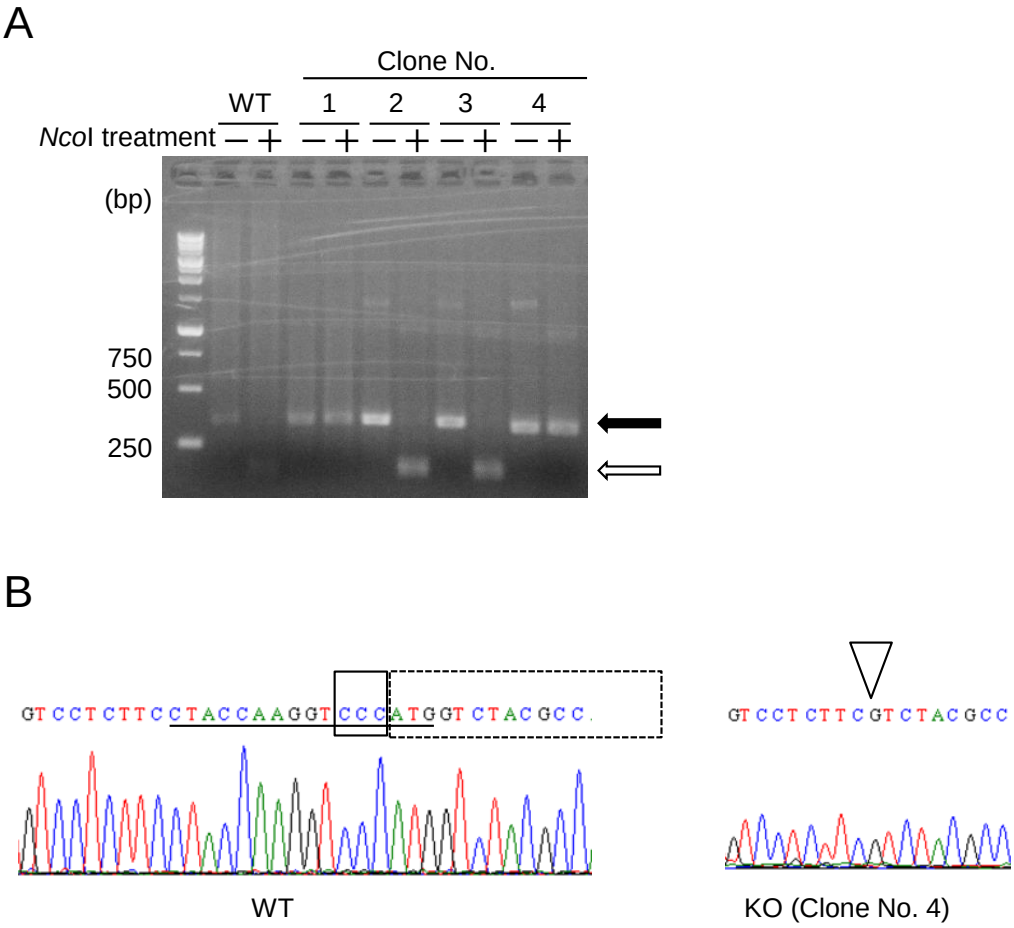

Fig. 3. Screening and analysis of *Rnaseh2a*$^{-/-}$ homozygote NIH3T3 cells. (A) Patterns of agarose gel electrophoresis. PCR products amplified from the genomic DNA of the WT and clones 1–4 cells were digested with *Nco*I and applied to 2% w/v agarose gel. The open arrow indicates the overlapping two bands (187 and 169 bp) corresponding to the PCR product which was cleaved by *Nco*I. The solid arrow indicates the band corresponding to the PCR product which was not cleaved. (B) Nucleotide sequences of the exon 2 of the *Rnaseh2a* gene in the WT and clone 4 (KO) cells. The solid underline in WT indicates the sequence which was deleted in clone 4, and the inverted open triangle in clone 4 indicates the site at which the deletion occurred. The PAM and target sequences are indicated by a box with solid and dashed lines, respectively.

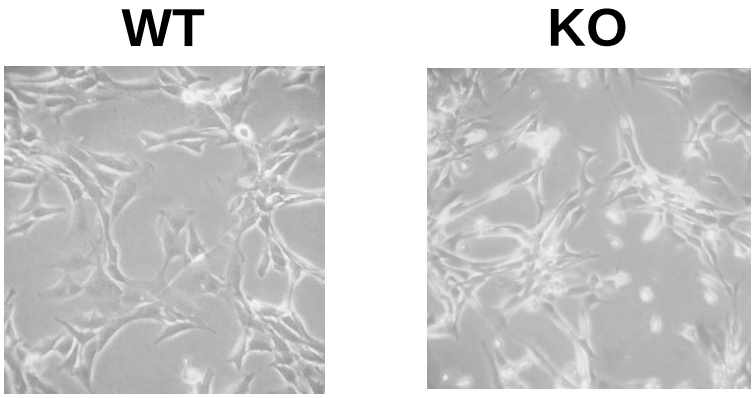

Fig. 4. Microscopic images of the WT and KO cells at ×200 magnification.

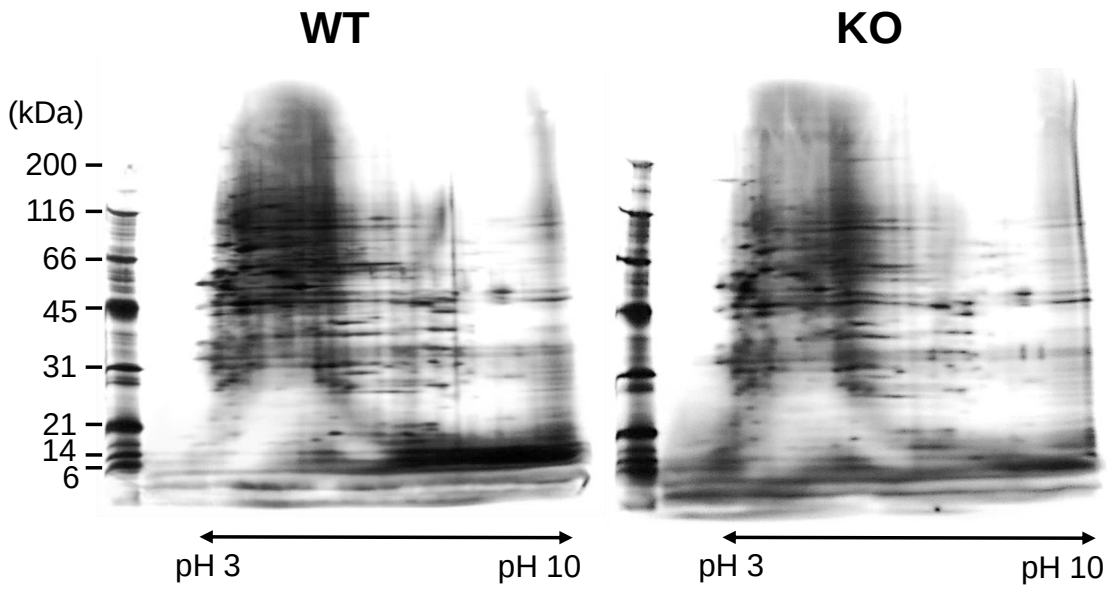

Fig. 5. Two-dimensional gel electrophoresis analysis of the cell lysates from the WT and KO cells. Cell lysate containing 10 mg protein was mixed with equal volumes of 5 M urea, 1 M thiourea, 1% w/v CHAPS, and 1% v/v Triton X-100, and the mixture was treated with 0.1 M acrylamide and 10 mg/ml DTT for 10 min at room temperature. Isoelectric focusing (IEF) was conducted using an agar gel with pH range of 3–10 in a capillary tube of 7.5 cm length and 2.5 mm I.D. Electrophoresis was carried out for 210 min at 300 V using 10 mM phosphoric acid and 0.2 M NaOH as an anode and cathode solution, respectively. After IEF, the gel was equilibrated in 50 mM Tris-HCl (pH 6.8) containing 2% w/v SDS and 0.001% w/v BPB for 10 min. The equilibrated gel was transferred onto precast 5–20% gradient polyacrylamide gels (9×8.3 cm). Electrophoresis was conducted for 85 min at a constant current of 20 mA per gel. Proteins in the gel were visualized by silver staining with Sil-Best Stain One (Nacalai tesque).

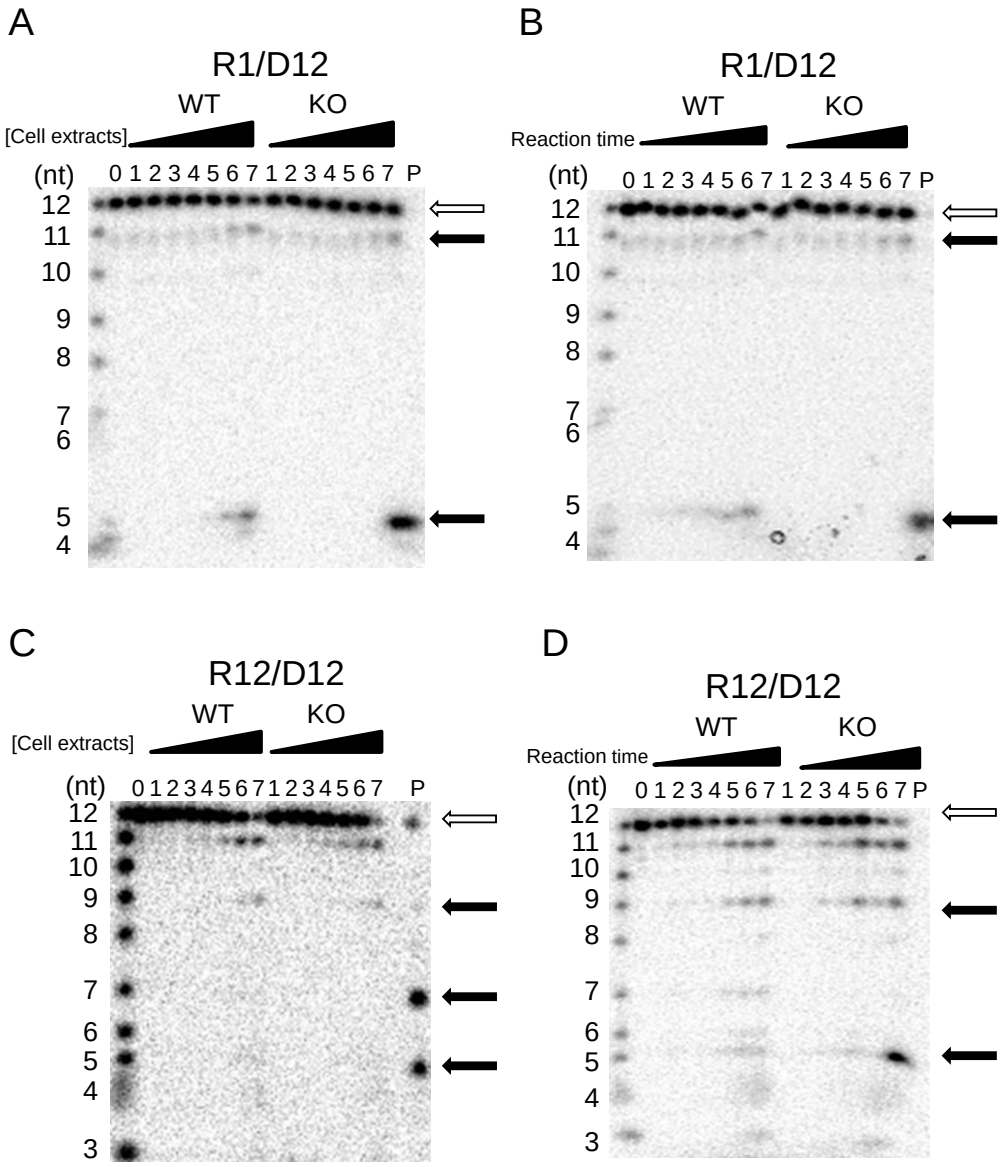

Fig. 6. RNase H activity of the extracts of NIH3T3 cells. (A–D) Patterns of denatured polyacrylamide gel electrophoresis. Reactions (7.5 μl) were carried out with either of 200 nM R1/D12 (A, B) and R12/D12 (C, D) at pH 8.0 at 25ºC. After the reaction, the reaction solutions were applied to 20% w/v denaturing polyacrylamide gel. Protein amounts (ng) of the cellular extracts in the reaction solution in lanes 0–7 were 0, 0.19, 0.96, 4.8, 24, 120, 600, and 3,000, respectively (A, C) or 1,400 (B, D). Reaction time points (min) in lanes 0–7 were 10 (A, C) or 0, 1.25, 2.5, 5, 10, 20, 40, and 80, respectively (B, D). Reaction was carried out for 10 min with the purified human RNase H2 (0.02 ng) instead of the cellular extract (lane P in A–D). The open and solid arrows indicate the bands corresponding to the 12-nt RNA fragment and cleavage products, respectively.

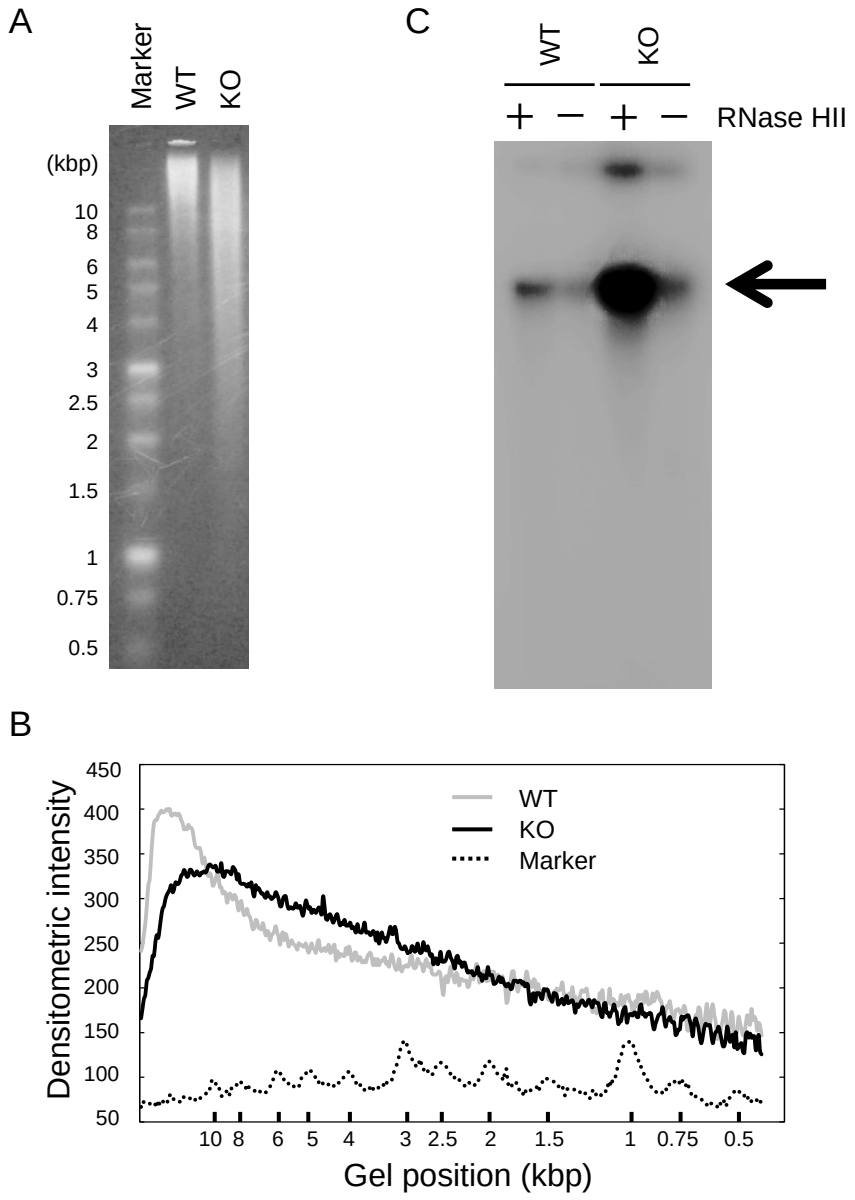

Fig. 7. Ribonucleotides incorporated in the genomic DNA of NIH3T3 cells. (A) Patterns of alkaline agarose gel electrophoresis. Alkaline-treated genomic DNA of the WT and KO cells was applied to 1% w/v alkaline agarose gel. (B) Densitometry scanning of the lanes of (A). (C) Nick translation. Genomic DNA of the WT and KO cells was nicked by *E. coli* RNase HII, followed by DNA polymerase I-dependent nick translation in the presence of [^{32}P]-dCTP. The reaction products were applied to 1% w/v agarose gel.

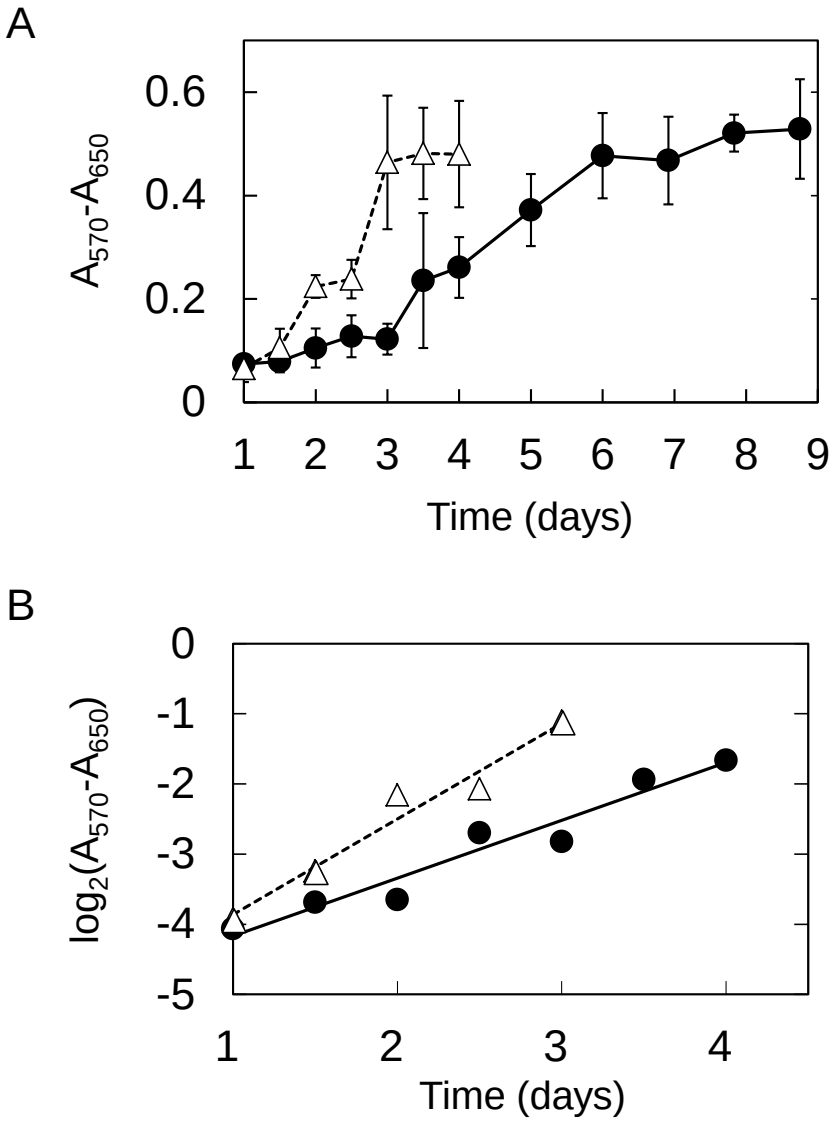

Fig. 8. Growth of NIH3T3 cells. (A, B) Growth curves. The WT and KO cells were added to 96-well microplates and cultured. At the time indicated, MTT reduction was measured. Open triangle and filled circle indicate WT and KO cells, respectively. Error bars indicate SD values for eight-time measurements (A). Vertical axis in Fig. 8A is changed to a logarithmic scale (B).

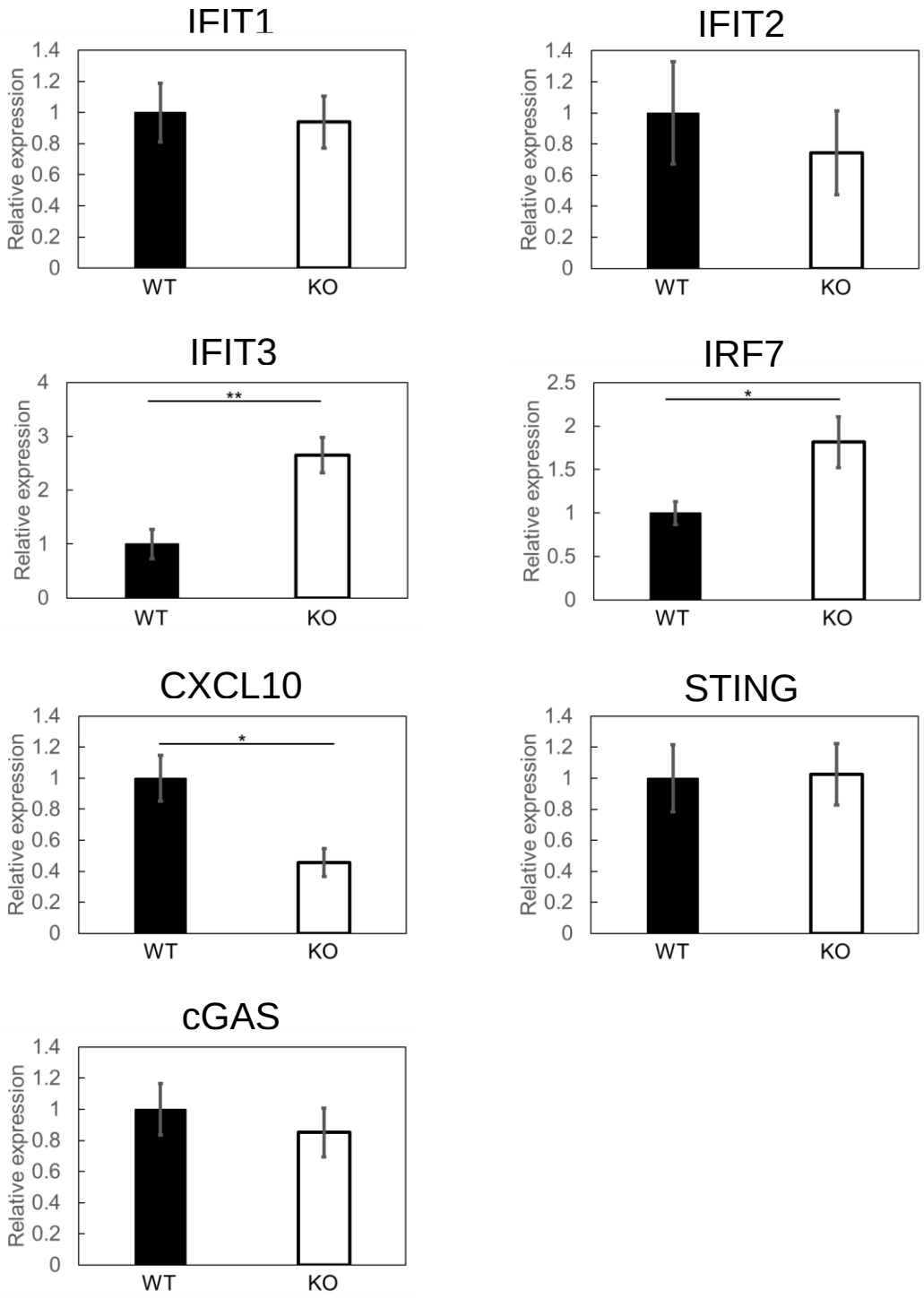

Fig. 9. Expression of ISGs and cGAS/STING in NIH3T3 cells. The expression of the genes was quantified by qPCR. Expression level was determined relative to hypoxanthine phosphoribosyltransferase (HPRT). Relative expression indicates the value compared to that in the WT cells. Error bars indicate SEM values for six-time measurements. **P* < 0.05, ***P* < 0.01. Unpaired Student's *t* test (two tailed, *n* = 6)

Chapter 5

Establishment of genome profiling-based mutation assay (GPMA) using mammalian cells

Introduction

As described in General introduction, DNA repair capacity has been analyzed by growth of yeast (11, 12). In yeast, DSB is induced in a gene related to the biosynthesis of histidine and the yeast can grow in a medium lacking histidine only when the damaged gene is completely repaired by a homologous recombination (12). Using this method, the contribution of RNase H2 to the repair of the damaged gene was assessed (12). However, the results obtained from the yeast are not immediately applicable to human because the amino acid sequence homology between yeast and human RNase H2 is low (approximately 40%) and the life cycle of yeast is quite different from that of human.

Genome profiling-based mutation assay (GPMA), which is different from the conventional phenotype-based testing, deserves to be characterized because it has been suggested to have much higher sensitivity than the Ames test which is a gold standard method to detect mutagenicity (13). Besides, the DNA-based mutation assay can potentially utilize any organism as a tester because this test does not require any special phenotypic trait (such as histidine metabolism, DNA repair activity, or fluorescence) of the organisms for its detection. Only the DNA extracted from an organism exposed to a mutagen is required for GPMA, implying that any type of organism can serve as a

tester.

Considering the estimation of mutagenicity to human, mammalian cell seems preferable to *E. coli* in GPMA. Furthermore, the construction of a novel method of evaluation for a DNA repair capacity is desired. In this chapter, the applicability of mammalian cells to GPMA was investigated.

Materials and Methods

Chemicals – The chemicals tested in this study were selected in databases: the National Library of Medicine, Toxicology Data Network, and the Chemical Carcinogenesis Research Information System (CCRIS). The level of mutagenicity of these reagents was evaluated based on the data from TOXNET and ECB-ESIS to determine the lowest concentration of each reagent that yields a positive effect in the Ames test (Table 1). The chemicals used were: acetaldehyde [CAS 75-07-0, CCRIS Recorded Number 1396], benzene [71-43-2, 70], diethyl ether [60-29-7], 4-dimethylaminoazobenzene [60-11-7], 1,2-dibromoethane [106-93-4], 2,4-dinitroflurobenzene [70-34-8, 1800], methyl acrylate [96-33-3, 1839], acrylonitrile [107-13-1, 8], diethyl sulfate[64-67-5, 242], chloral hydrate [302-17-0, 4142], hexamethylenetetramine [100-97-0, 2297], hydrazine sulfate [10034-93-2, 336], trimethyl phosphate [512-56-1, 610], benzophenone [119-61-9, 629], propylene oxide [75-56-9, 540], ethylene glycol [107-21-1, 3744], acetic anhydride [108-24-7, 688], allylamine [107-11-9, 4746], methanesulfonic acid [75-75-2, 2783], ammonium persulfate [7727-54-0, 1430], all of which were purchased from Sigma-Aldrich (USA), were intensively tested in this study. EthBr (Ethidium bromide) purchased from Aldrich,

USA. The chemicals were dissolved in Milli-Q water (Millipore, Japan) and passed through a nucleopore filter (0.22 μm, Millipore, USA). In GPMA, all the chemicals were tested either individually and were added into sterile tubes (containing 200 μl of the Davis medium and 2 μl of diluted bacterial preculture) for *E. coli* and 12-well plates (containing 3 ml of the RPMI1640 and 1.5×10^4 cells) for NIH3T3 at final concentrations of 100 ppb.

The growth medium and the generation of cultured cells – For GPMA, the Davis medium was prepared for *E. coli* culture. Only top grade commercially available reagents were used (from Wako Pure Chemical Industries, Ltd.). The medium for mammalian cell culture used here was RPMI1640 (Nacalai Tesque) containing 10% of fetal bovine serum (Nacalai Tesque) and 0.25% trypsin, 2% EDTA·2Na, and PBS (pH 7.2) (Nacali Tesque). Generation number, *G*, was estimated from the following equation:

$$G = \ln (N/N_0) \ln 2 \quad (1)$$

where N and N_0 represent the numbers of post-culture and starting bacteria (or mammalian cells), respectively. The G obtained from mutagen-free culture was also used for those cells cultured with mutagen for the same time period.

GPMA analysis – GPMA includes two main steps: (i) Induction of DNA mutation in cell culture and (ii) Detection of the induced DNA mutation by the Genome profiling (GP) method (58). In this Chapter, *E. coli* and NIH3T3 mouse fibroblast cells were

selected for tester organism. The GP method consists of (i) random PCR for sampling DNA fragments from the tester organism; (ii) DNA sequence analysis by micro-temperature gradient gel electrophoresis (μTGGE); and (iii) computer-aided normalization and processing of data. GP has already been demonstrated to be highly potential in measuring the genomic DNA alteration from diversities of organisms and cells (59–66).

Random PCR – This procedure serves to reduce and represent the voluminous genome information uniquely and reproducibly (67–69). Cultured *E. coli* cells were directly utilized for random PCR. DNA of NIH3T3 cells was extracted by GenElute Mammalian Genomic DNA Miniprep Kits (Sigma) and then used for random PCR. An aliquot (10^4-cell equivalent) of 1 μl and 1 ng (/μl) of diluted bacterial and mammalian cell cultures was used, respectively, for a 20-μl PCR. Random PCR was carried out using a single fluorescent primer (Cy3-labeled pfM12, with the sequence 5′-dAGAACGCGCCTG-3′) under conditions of low annealing temperature (26 °C) (67). Two internal reference DNAs were used: one of them (200 bp, T_m = 60°C) was amplified by conventional PCR from gene VIII of the bacteriophage fd genome (map position: 1341–1540) using two primers, MA1 (5′-Cy3-labeled dTGCTACGTCTCTTCCGATGCTGTCTTTCGCT-3′) and MA2 (5′-dTTGAATTCTATCGGTTTATCA-3′). The other internal reference DNA (900 bp, T_m = 61.4°C) was also amplified by PCR from pBR322 using the primers, Ref 6F (31 mer: 5′-Cy3-labeled-GCCGGCATCACCGGCGCCACAGGTGCGGTTG-3′) and Ref 6R (31 mer: 5′-TAGCGAGGTGCCGCCGGCTTCCATTCAGGTC-3′) as forward and reverse primers, respectively.

μTGGE (miniaturized version of temperature gradient gel electrophoresis) – This procedure is important for extraction of the sequence information without sequencing (69). PCR products were subjected to μTGGE using a microcassette (Taitec, Koshigaya, Japan) with a gel size of 2.5 × 2.5 × 0.1 cm (70). Samples were subjected to electrophoresis using a μTGGE apparatus, microTG (Taitec) or microTGGE (Lifetech, Iruma, Japan) with a temperature gradient (15–65°C) set perpendicularly to the direction of DNA migration (10 min at 100 V). Bands were identified by scanning the gel on a fluorescence imager, SAYAKA-IMAGER (DRC, Japan), with filters for excitation (550 nm) and emission (565 nm) for the Cy3 dye.

Computer-aided normalization – A set of feature points was assigned to each genome profile displayed on the computer and was converted to species identification dots (spiddos) (71). Furthermore, a measure of similarity between two genomes, the pattern similarity score (*PaSS*), was calculated using spiddos (13). At the first step, the computer tries to make spiddos pairwise in relation to two sets of spiddos and, thus, the same number of pairs is generated as that of the smaller set. Then, the *PaSS* is calculated between them following the known equation. Changing the combination of pairs, we repeated the process until the maximum *PaSS* for the two sets was found, which is the final *PaSS* for the two sets of spiddos (i.e., machine-defined spiddos pairs) (71).

Definition of mutagenicity – In principle, the decision of mutagenicity was made from the value of *ΔΔPaSS* (13). Namely, if this value for a chemical is significantly

positive sign considering the standard deviation (SD), then it is determined to be mutagenic. Besides this principle, setting an empirical threshold must be convenient.

Results and Discussion

Analysis of mutagenicity of ethidium bromide in NIH3T3 cells – At the beginning, viability, the growth rate, and detectability of mutations of the NIH3T3 cells were examined by culturing in a medium with or without the mutagen ethidium bromide (EthBr). NIH3T3 cells cultured for 7 days in the medium containing 1 ppm EthBr were obviously affected by this mutagen, resulting in growth inhibition and abnormal shapes of cells (Figs. 1 and 2A1–A4). Evidently, 10 ppm EthBr is too harsh for this cell line to survive normally. As shown in Fig. 2B, 5-day and 7-day cultures of NIH3T3 cells with 0.3 ppm EthBr revealed the mutagenicity of EthBr. Considering the composite nature of the NIH3T3 medium, which might contain components (ppm or more) inhibitory to the mutagen assay, this result is nothing but fortunate. Besides, even 5 days (3-generation equivalent) of culturing enabled us to detect the mutagenicity (Fig. 2B). At the same time, dependence of the level of mutagenicity (*ΔPaSS* value) on the concentration of a mutagen (0.3, 1, and 10 ppm) is evident in the results obtained after 5 days (equivalent to ~3 generations) of culturing. As expected, 1 ppm and, needless to say, 10 ppm EthBr were found to have a strong growth-inhibitory effect (Fig. 2).

Correlation of the levels of mutagenicity obtained in the GPMA with NIH3T3 and that with E. coli – Considering the results thus obtained, one possible set of standard conditions for mammalian-cell-based GPMA (mGPMA) could be proposed: a chemical

at 100 ppb and 5-day culture of NIH3T3 cells. Under these experimental conditions for mGPMA (even though 7-day culture was chosen here for clarity as the chemicals used were known to be not strong mutagens), six chemicals (##1–6 in Table 1) were screened for mutagenic effects (Fig. 3A). Three out of four chemicals (#1, #2, and #4) which are Ames test-positive were shown to be mutagenic and two chemicals (#5 and #6), according to the Ames test, non-mutagenic, were shown marginal (possibly non-mutagenic but cannot be clearly decided here) in this assay, leading to the resembled but substantially different assignment of mutagenicity from that of bacteria-based GPMA (bGPMA). Therefore, mGPMA seems to qualitatively determine mutagenicity of chemicals although this conclusion needs to be strengthened by as larger a number of mGPMA experiments as that of bGPMA. From Figure 3B which was generated by using single-trial data with some of multi-trial ones, the following intriguing results were obtained. A relatively high correlation (r = 0.77) was observed in the level of mutagenicity between bGPMA and mGPMA. In almost all of the chemicals evaluated, the levels of mutagenicity in mGPMA well correlated with those in bGPMA.

Because the intracellular metabolic networks of these two organisms are quite different, different responses to the same chemical are conceivable. As an example, benzene is known to be a barely mutagenic substance; however, it can be metabolized to mutagenic ones such as phenol (in the liver), subsequently to hydroquinone (in bone marrow), and then converted non-enzymatically to *p*-benzoquinone (72). All of them are mutagenic. Accordingly, the relatively higher mutagenicity of benzene (#1 of open triangle: tested with 3 trials) shown by mGPMA as compared to bGPMA might reflect such a metabolic effect of mammalian cells (though, here, not tested in the body system [*in vivo*]). Therefore, even though the experiments done here is still a preliminary stage,

these differences might reflect the respective intracellular metabolic networks. If so, mGPMA can be a better detector of mutagens (that can cause cancer) (73) in comparison with bGPMA.

Another piece of supporting evidence for the effectiveness of mGPMA (also bGPMA) is that all the Ames test-positive chemicals (15 chemicals shown in open triangls) (Fig. 3B) are located in the same area, right upper corner (except for #3 and #12) and are distant from the other five chemicals (Ames test-negative; shown in filled triangles) (Fig. 3B), confirming that mGPMA can discriminate mutagens from non-mutagens semi-quantitatively (Interestingly, this result allows us to tentatively set a more reliable threshold of *ΔΔPaSS* for determining mutagenicity in both bGPMA and mGPMA: 0.005). Therefore, further studies on diverse chemicals using mGPMA hold promise. Besides, the mammalian cell tester can naturally consist of human cells, which must be more relevant and more physiologically interesting (73).

Conclusion – The conditions of 100 ppb chemical concentration and 3–5 generations of NIH3T3 cells in culture could be selected tentatively. Because of congruence in the determination of mutagenicity between the bGPMA and Ames test, a clear interpretation could be obtained for the higher sensitivity of the DNA-based assay (GPMA) relative to phenotype-based ones (such as the Ames test): the difference in the sites being analyzed. The latter approach deals with a limited number of specific nucleotides, and the former approach targets the whole length of DNA. Thus, this study should help to elucidate the essential properties of GPMA, a relatively novel technology in the field of toxicology and be applied to an analysis of a DNA repair capacity in RNase H2 knockout NIH3T3 cells as described in Chapter 4.

Table 1. List of mutagenicity for chemicals and converted mutagenic strength (examined by the Ames test) of the reagents used.

Serial #	Reagents [CAS No.]		*ΔΔPaSS*[a]	Ames test			
				Minimum Dose[b]		Mutagenic Strength[c] (S)	Strength Level[d] (L)
				(μg/plate)	(ppm)		
1	Benzene	[71-43-2]	0.009±0.0009	75	3	0.33	1
2	Chloral hydrate	[302-17-0]	0.007±0.0007	30	1.2	0.83	1
3	Propylene oxide	[75-56-9]	0.007±0.0005	100	4	0.25	1
4	Diethyl sulfate	[64-67-5]	0.01±0.002	0.08	0.0032	312	4
5	Acetic anhydride	[108-24-7]	0.001±0.00	N	N	N	0
6	Methanesulfonic acid	[75-75-2]	-0.0005± 0.00	N	N	N	0
7	1,2-dibromoethane	[106-93-4]	0.007±0.0002	3.3	1.3	7.5	2
8	2,4-dinitroflurobenzene	[70-34-8]	0.007±0.0002	5	0.2	5	2
9	Diethyl ether	[60-29-7]	0.009±0.0006	6	0.24	4.1	2
10	4-dimethylaminoazobenzen	[60-11-7]	0.009±0.0005	0.5	0.02	50	3
11	Acetaldehyde	[75-07-0]	0.006±0.0005	100	4	0.25	1
12	Methyl acrylate	[96-33-3]	0.005±0.0003	25	1	1	1
13	Hexamethylenetetramine	[100-97-0]	0.01±0.000	5	0.2	5	2
14	Hydrazine sulfate	[10034-93-2]	0.01±0.0006	100	4	0.25	1
15	Benzophenone	[119-61-9]	0.005±0.0008	20	0.8	1.25	2
16	Acrylonitrile	[107-13-1]	0.009±0.0001	100	4	0.25	1
17	Trimethyl phosphate	[512-56-1]	0.01±0.001	31	1.24	0.8	1
18	Ethylene glycol	[107-21-1]	0.002 ±0.00	N	N	N	0
19	Allylamine	[107-11-9]	0.002± 0.000	N	N	N	0
20	Ammonium persulfate	[7727-54-0]	-0.002±0.0005	N	N	N	0

[a]The strength of mutagenicity of each chemical/group is evaluated by ***ΔΔPaSS*.**

[b]Minimum effective dose, *i.e.*, the minimum amount of reagents per plate (about 25 ml) which brought about an observable number of revertants (usually about 100/plate). ppm is parts-per-million.

[c]By definition, 25 /minimum-dose.

[d]If S is; N, ≥ 0 and ≤ 1, ≥ 1 and < 10, ≥ 10 and <100, ≥ 100 and <1000 or $\geq 10^3$ and $<10^4$, then, L = 0, 1, 2, 3, 4 or 5, respectively.

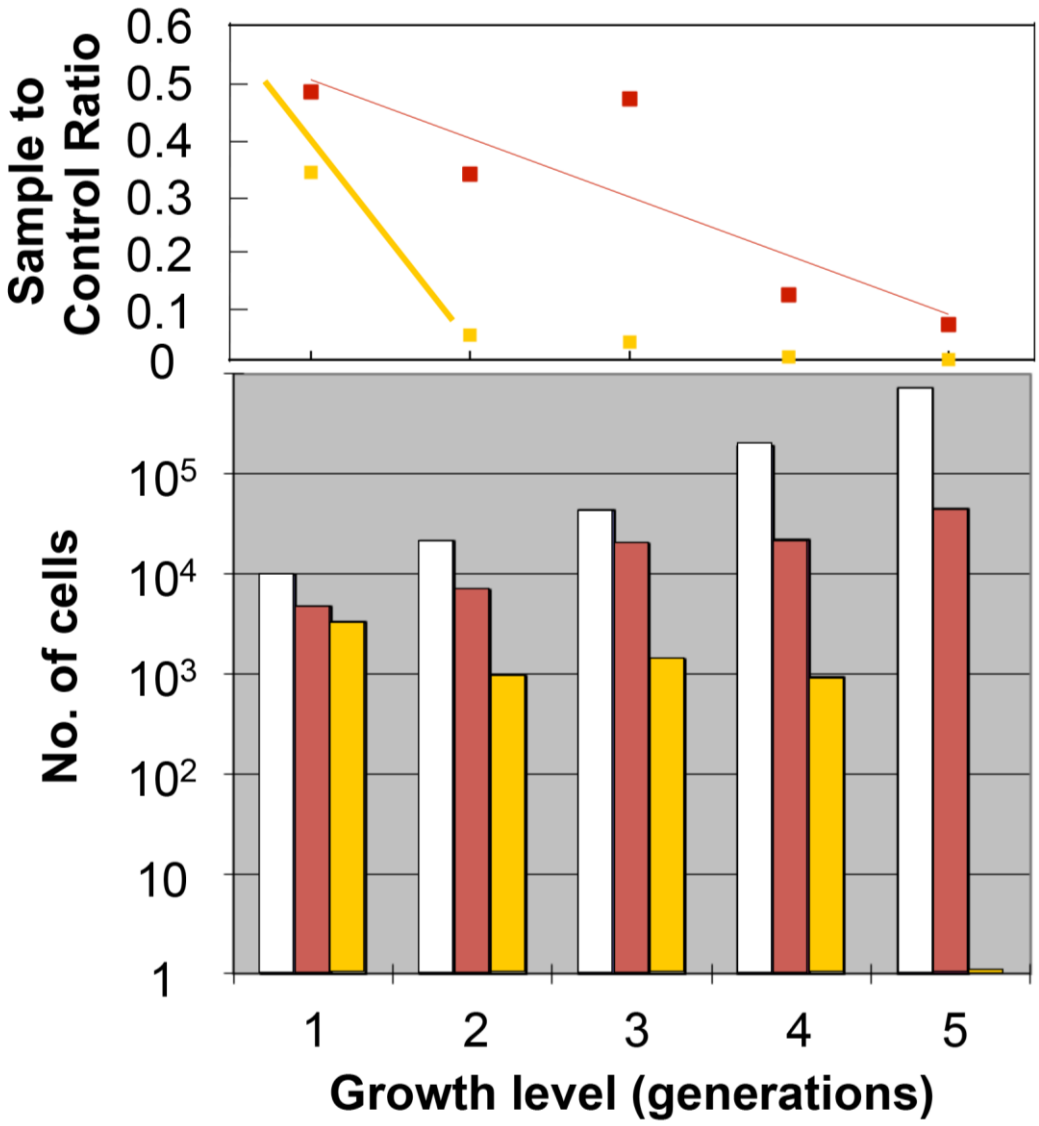

Fig. 1. Inhibition of NIH3T3 cell growth by high concentrations of EthBr. Two presentations are used: the normalized growth rate of NIH3T3 cells in the presence of EthBr as compared to the control (culture without EthBr) (top). A bar graph of NIH3T3 cell growth during culture with or without EthBr (bottom). Bars from left to right: 0, 1, and 10 ppm of EthBr. Note the difference in the vertical scale for both graphs.

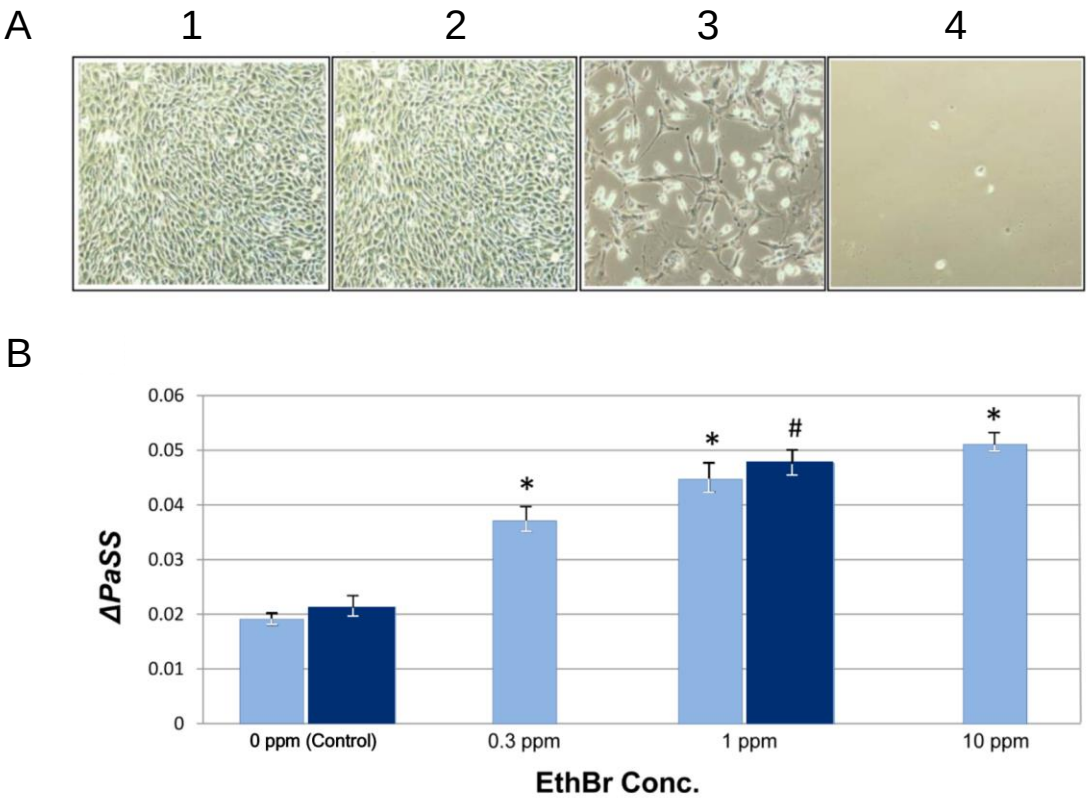

Fig. 2. Effects of mutagen EthBr on the growth and mutability of NIH3T3 cells. (A) Microscopic images of cells cultured in EthBr containing media. NIH3T3 cells were cultured at different concentrations of EthBr for 7 days: (A1) control NIH3T3 cells (without EthBr), (A2) with EthBr at 0.3 ppm, (A3) 1 ppm, and (A4) 10 ppm. (B) *ΔPaSS* values for NIH3T3 cells cultured in the medium containing different concentrations of EthBr. The width of bars represents the culture duration (three and five generations for normal and wider bars, respectively). The symbols, * and #, indicate $P<0.05$ in comparison with the control for three and five generations, respectively. Actually, cells were cultured for 5 or 7 days, which are called three or five generations, respectively, for convenience, although this relation can hold only for the case of control (cultivation without a mutagen). The trials were performed in duplicate.

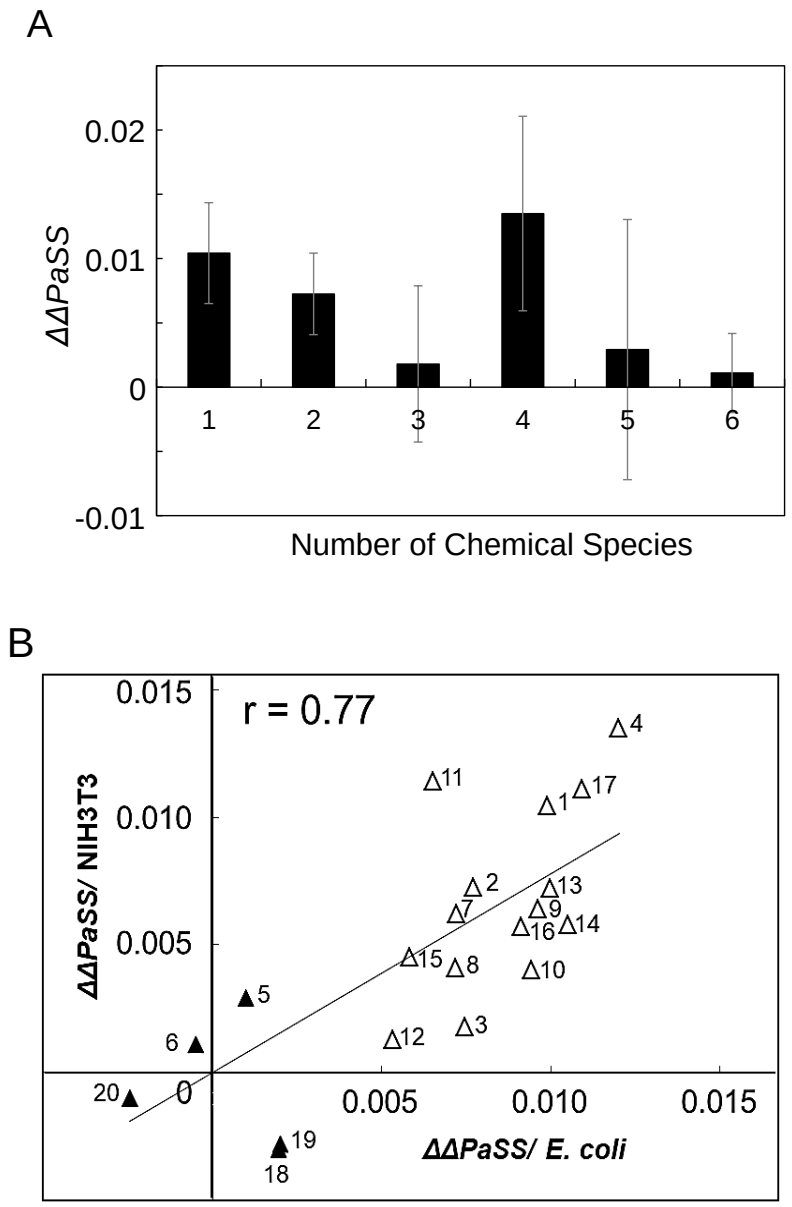

Fig. 3. Mammalian-cell-based GPMA (mGPMA). The mutagenicity assay of chemicals was performed on NIH3T3 cells. (A) Six chemicals (##1–6) were subjected to GPMA at the concentration of 100 ppb for 4 generations. The experimental data were obtained from three trials. (B) Correlation of two types of *ΔΔPaSS* (mutagenicity) measured by bGPMA (*E. coli*-based) and mGPMA (NIH3T3-based). Each plot is linked to its source chemical via a specific ID number (Table 1). Filled triangles represent the Ames test negative chemicals and the open triangles represent the Ames test positive chemicals. The results of #1-6 chemicals were the averaged data in triplicate trials and those of #7-20 chemicals were in a single trial. Correlation coefficient (r) = 0.77.

Summary

Chapter 1

The effects of neutral salts and pH on the activity and stability of human RNase H2 were examined. NaCl, KCl, RbCl, and NaBr increased the activity to 170–390% at 10–60 mM, while LiCl, LiBr, and CsCl inhibited it, suggesting that species of cation, but not anion, is responsible for the effect on activity. NaCl and KCl increased the stability by decreasing the first-order rate constant of the inactivation to 50–60% at 60–80 mM. The activity at 25–35°C exhibited a narrow bell-shaped pH-dependence with the acidic and alkaline pK_e (pK_{e1} and pK_{e2}) values of 7.3−7.6 and 8.1−8.8, respectively. Enthalpy changes (ΔH^o) of deprotonation were 5 ± 21 kJ mol^{-1} for pK_{e1} and 68 ± 25 kJ mol^{-1} for pK_{e2}. These results suggested that the ionizable groups responsible for pK_{e1} are two out of Asp34, Glu35, and Asp141 of DEDD motif, and that for pK_{e2} is Lys69 of DSK motif.

Chapter 2

We examined the activity and stability of six recombinant human RNase H2 variants bearing one AGS-causing mutation, A-G37S (Gly37 in the A subunit is replaced with Ser), A-N212I, A-R291H, B-A177T, B-V185G, or C-R69W. The activity of A-G37S was 0.3–1% of that of the wild-type RNase H2 (WT), while those of other five variants were 51–120%. In circular dichroism measurement, the melting temperatures of variants were 50–53°C, lower than that of WT (56°C). These results suggested that A-G37S had decreased activity and stability than WT, while other five variants had decreased stability but retained activity. In gel filtration chromatography of the purified enzyme preparation, WT migrated as a heterotrimer, while A-R291H eluted

in two separate peaks containing either the heterotrimer or only the A subunit, suggesting that some AGS-causing mutations affect the heterotrimer-forming stability of RNase H2.

Chapter 3

Val143 of human RNase H2 is located at the active site and is conserved in eukaryotic RNase H2. We explored the role of Val143 in catalytic activity and substrate specificity. Nineteen single variants at amino acid position 143 were expressed in *E. coli*, and all variants except for V143C and V143M were purified from the cells. When the activity of the wild-type human RNase H2 (WT) was set as 100%, the relative single ribonucleotide excision activity (activity A) and RNA strand degrading activity (activity B) of the 17 variants were in the range of 0.05–130 and 0.02–42%, respectively. When the ratio of the relative activity A to the relative activity B of WT was set as 1, the ratios of the 17 variants were in the range of 0.2–5.7. This indicated that the valine residue is optimal for balancing the two activities. The ratios for V143Y and V143W were relatively high (5.6 and 5.5, respectively), suggesting that the bulky residues like tyrosine and tryptophan at position 143 caused steric hindrance with the 2'-OH of the sugar moiety of the ribonucleotide at the 5' side of the scissile phosphodiester bond. These results suggested that Val143 is not critical for, but plays a role in determining catalytic activity and substrate specificity.

Chapter 4

We constructed RNase H2 knockout NIH3T3 cells (KO cells) by CRISPR/Cas9 system to explore the roles of mammalian RNase H2 in cells. KO cells hydrolyzed RNA

strands in RNA/DNA hybrid, but not single ribonucleotides in DNA duplex, while wild-type NIH3T3 cells (WT cells) hydrolyzed both. Genomic DNA in the KO cells was more heavily hydrolyzed than in the WT cells by the alkaline or RNase H2 treatment, suggesting that the KO cells contained more ribonucleotides in genomic DNA than the WT cells. The growth rate of the KO cells was 60% of that of the WT cells. Expression of interferon-stimulated genes (ISGs) in the KO cells was not markedly elevated compared to the WT cells. These results suggested that in NIH3T3 cells, RNase H2 is crucial for suppressing the accumulation of ribonucleotides in genomic DNA but not for increasing the expression levels of ISGs.

Chapter 5

Genome profiling-based mutation assay (GPMA) can be a superior method to evaluate the DNA repair capacity in cells and further the contribution of RNase H2 to it, because it is a DNA-based method. However, in GPMA, *E. coli* had been used as a test organism. To more accurately predict the effects of chemicals on human cells, the applicability of mammalian cells to GPMA was investigated. When NIH3T3 cells were cultured for 7 days in the presence of 1 or 10 ppm ethidium bromide (EthBr), cell growth was inhibited and cell shapes were abnormal. The mutagenicity was detected in the presence of 0.3–10 ppm EthBr. For 20 chemicals, the mutagenicity in GPMA was examined. When cells were cultured in the presence of a 100 ppb chemical, the mutagenicity in GPMA with NIH3T3 were well correlated with that in GPMA with *E. coli* with the correlation coefficient of 0.77. These results suggested that mammalian cells can be used in GPMA instead of *E. coli*. Use of RNase H2 knockout NIH3T3 cells, which was constructed in Chapter 4, is a future subject.

References

1. Cerritelli, S.M. and Crouch, R.J. (2009) Ribonuclease H: the enzymes in eukaryotes. *FEBS J*., **276**, 1494–1505
2. Champoux, J.J. and Schultz, S.J. (2009) Ribonuclease H: properties, substrate specificity and roles in retroviral reverse transcription. *FEBS J*., **276**, 1506–1516
3. Tadokoro, T. and Kanaya, S. (2009) Ribonuclease H: molecular diversities, substrate binding domains, and catalytic mechanism of the prokaryotic enzymes. *FEBS J*., **276**, 1482–1493
4. Rychlik, M.P., Chon, H., Cerritelli, S.M., Klimek, P., Crouch, R.J., and Nowotny, M. (2010) Crystal structures of RNase H2 in complex with nucleic acid reveal the mechanism of RNA-DNA junction recognition and cleavage. *Mol. Cell*, **40**, 658–670
5. Yang, W., Lee, J.Y., and Nowotny, M. (2006) Making and breaking nucleic acids: two-Mg^{2+}-ion catalysis and substrate specificity. *Mol. Cell*, **22**, 5–13
6. Sparks, J.L., Chon, H., Cerritelli, S.M., Kunkel, T.A., Johansson, E., Crouch, R.J., and Burgers, P.M. (2012) RNase H2-initiated ribonucleotide excision repair. *Mol. Cell*, **47**, 980–986
7. Williams, J.S. and Kunkel, T.A. (2014) Ribonucleotides in DNA: origins, repair and consequences. *DNA Repair*, **19**, 27–37
8. Cerritelli, S.M. and Crouch, R.J. (2016) The Balancing Act of Ribonucleotides in DNA. *Trends Biochem. Sci.*, **41**, 434–445
9. Crow, Y.J., Leitch, A., Hayward, B.E., Garner, A., Parmer, R., Griffith, E., Ali, M., Semple, C., Aicardi, J., Babul-Hirji, R., Baumann, C., Baxter, P., Bertini, E.,

Chandler, K.E., Chitayat, D., Cau, D., Déry, C., Fazzi, E., Goizet, C., King, M.D., Klepper, J., Lacombe, D., Lanzi, G., Lyall, H., Martínez-Frías, M.L., Mathieu, M., McKeown, C., Monier, A., Oade, Y., Quarrel, O.W., Rittey, C.D., Rogers, R.C., Sanchis, A., Stephenson, J.B., Tacke, U., Till, M., Tolmie, J.L., Tomlin, P., Voit, T., Weschke, B., Woods, C.G., Lebon, P., Bonthron, D.T., Ponting, C.P., and Jackson, A.P. (2006) Mutations in genes encoding ribonuclease H2 subunits cause Aicardi-Goutières syndrome and mimic congenital viral brain infection. *Nat. Genet*., **38**, 910–916

10. Coffin, S.R., Hollis, T., and Perrino, F.W. (2011) Functional consequences of the RNase H2A subunit mutations that cause Aicardi-Goutières syndrome. *J. Biol. Chem.*, **286**, 16984–16991
11. Storici, F., Bebenek, K., Kunkel, T.A., Gordenin, D.A., and Resnick, M.A. (2007) RNA-templated DNA repair. *Nature*, **447**, 338−341
12. Keskin, H., Shen, Y., Huang, F., Patel, M., Yang, T., Ashley, K., Mazin, A.V., and Storici, F. (2014) Transcript-RNA-templated DNA recombination and repair. *Nature*, **515**, 436−439
13. Futakami, M., Salimullah, M., Miura, T., Tokita, S., and Nishigaki, K. (2007) Novel mutation assay with high sensitivity based on direct measurement of genomic DNA alterations: comparable results to the Ames test. *J. Biochem.*, **141,** 675–686
14. Mackenzie, K.J., Carroll, P., Lettice, L., Tarnauskaite, Ž., Reddy, K., Dix, F., Revuelta, A., Abbondati, E., Rigby, R.E., Rabe, B., Kilanowski, F., Grimes, G., Fluteau, A., Devenney, P.S., Hill, R.E., Reijns, M.A., and Jackson, A.P. (2016) Ribonuclease H2 mutations induce a cGAS/STING-dependent innate immune response. *EMBO. J.*, **35**, 831–844

15. Pokatayev, V., Hasin, N., Chon, H., Cerritelli, S.M., Sakhuja, K., Ward, J.M., Morris, H.D., Yan, N., and Crouch, R.J. (2016) RNase H2 catalytic core Aicardi-Goutières syndrome-related mutant invokes cGAS-STING innate immune-sensing pathway in mice. *J. Exp. Med.*, **7**, 329–336
16. Yasukawa, K., Nemoto, D., and Inouye, K. (2008) Comparison of the thermal stabilities of reverse transcriptases from avian myeloblastosis virus and Moloney murine leukaemia virus. *J. Biochem.*, **143**, 261–268
17. Yasukawa, K., Mizuno, M., Konishi, A., and Inouye, K. (2010) Increase in thermal stability of Moloney murine leukaemia virus reverse transcriptase by site-directed mutagenesis. *J. Biotechnol.*, **150**, 299–306
18. Morishima, A., Yasukawa, K., and Inouye, K. (2012) A possibility of a protein-bound water molecule as the ionizable group responsible for pK_e at the alkaline side in human matrix metalloproteinase 7 activity. *J. Biochem.*, **151**, 501–509
19. Chon, H., Vassilev, A., DePamphilis, M.L., Zhao, Y., Zhang, J., Burgers, P.M., Crouch, R.J., and Cerritelli, S.M. (2009) Contributions of the two accessory subunits, RNASEH2B and RNASEH2C, to the activity and properties of the human RNase H2 complex. *Nucleic Acids Res.*, **37**, 96–110
20. Chon, H., Sparks, J.L., Rychlik, M., Nowotny, M., Burgers, P.M., Crouch, R.J., and Cerritelli, S.M. (2013) RNase H2 roles in genome integrity revealed by unlinking its activities. *Nucleic Acids Res.*, **41**, 3130–3143
21. You D.J., Jongruja, N., Tannous, E., Angkawidjaja, C., Koga, Y., and Kanaya S. (2014) Structural basis for salt-dependent folding of ribonuclease H1 from halophilic archaeon *Halobacterium* sp. NRC-1. *J. Struct. Biol.*, **187**, 119–128

22. Inouye, K., Lee, S.B., Nambu, K., and Tonomura, B. (1997) Effects of pH, temperature, and alcohols on the remarkable activation of thermolysin by salts. *J. Biochem.*, **122**, 358–364

23. Shaban, N.M., Harvey, S., Perrino, F.W., and Hollis T. (2010) The structure of the mammalian RNase H2 complex provides insight into RNA·DNA hybrid processing to prevent immune dysfunction. *J. Biol. Chem.*, **285**, 3617–3624

24. Brucet, M., Querol-Audí, J., Bertlik, K., Lloberas, J., Fita, I., and Celada, A. (2008) Structural and biochemical studies of TREX1 inhibition by metals. Identification of a new active histidine conserved in DEDDh exonucleases. *Protein Sci*., **17**, 2059–2069

25. Pollack, S.J., Atack, J.R., Knowles, M.R., McAllister, G., Ragan, C.I., Baker, R., Fletcher, S.R., Iversen, L.L., and Broughton, H.B. (1994) Mechanism of inositol monophosphatase, the putative target of lithium therapy. *Proc. Natl. Acad. Sci. USA*, **91**, 5766–5770

26. Chapados, B.R., Chai, Q., Hosfield, D.J., Qiu, J., Shen, B., and Tainer, J.A. (2001) Structural biochemistry of a type 2 RNase H: RNA primer recognition and removal during DNA replication. *J. Mol. Biol*., **307**, 541–556

27. Muroya, A., Tsuchiya, D., Ishikawa, M., Haruki, M., Morikawa, M. Kanaya, S., and Morikawa, K. (2001) Catalytic center of an archaeal type 2 ribonuclease H as revealed by X-ray crystallographic and mutational analyses. *Protein Sci.*, **10**, 707–714

28. Figiel, M., Chon, H., Cerritelli, S.M., Cybulska, M., Crouch, R.J., and Nowotny, M. (2011) The structural and biochemical characterization of human RNase H2 complex reveals the molecular basis for substrate recognition and Aicardi-Goutières

syndrome defects. *J. Biol. Chem.*, **286**, 10540–10550

29. Joshi, M.D., Sidhu, G., Pot, I., Brayer, G.D., Withers, S.G., and Mclntosh, L.P. (2000) Hydrogen bonding and catalysis: a novel explanation for how a single amino acid substitution can change the pH optimum of a glycosidase. *J. Mol. Biol*., **299**, 255–279
30. Zhang, K. and Auld, D.S. (1995) Structure of binary and ternary complexes of zinc and cobalt carboxypeptidase A as determined by X-ray absorption fine structure. *Biochemistry*, **34**, 16306–16312
31. Takeharu, H., Yasukawa, K., and Inouye, K. (2011) Thermodynamic analysis of ionizable groups involved in the catalytic mechanism of human matrix metalloproteinase 7 (MMP-7). *Biochim. Biophys. Acta*, **1814**, 1940–1946
32. Bastock, J.A., Webb, M., and Grasby, J.A. (2007) The pH-dependence of the *Escherichia coli* RNase HII-catalysed reaction suggests that an active site carboxylate group participates directly in catalysis. *J. Mol. Biol.*, **368**, 421–433
33. Jeong, H.S., Backlund, P.S., Chen, H.C., Karavanov, A.A., and Crouch, R.J. (2004) RNase H2 of *Saccharomyces cerevisiae* is a complex of three proteins. *Nucleic Acids Res.*, **32**, 407–414
34. Reijns, M.A., Bubeck, D., Gibson, L.C., Graham, S.C., Baillie, G.S., Jones, E.Y., and Jackson, A.P. (2011) The structure of the human RNase H2 complex defines key interaction interfaces relevant to enzyme function and human disease. *J. Biol. Chem.*, **286**, 10530–10539
35. Uehara, R., Cerritelli, S.M., Hasin, N., Sakhuja, K., London, M., Iranzo, J., Chon, H., Grinberg, A., and Crouch, R.J. (2018) Two RNase H2 mutants with differential

rNMP processing activity reveal a threshold of ribonucleotide tolerance for embryonic development. *Cell Rep.*, **25**, 1135–1145

36. Reijns, M.A., Rabe, B., Rigby, R.E., Mill, P., Astell, K.R., Lettice, L.A., Boyle, S., Leitch, A., Keighren, M., Kilanowski, F., Devenney, P.S., Sexton, D., Grimes, G., Holt, I.J., Hill, R.E., Taylor, M.S., Lawson, K.A., Dorin, J.R., and Jackson, A.P. (2012) Enzymatic removal of ribonucleotides from DNA is essential for mammalian genome integrity and development. *Cell*, **149**, 1008–1022
37. Hiller, B., Achleitner, M., Glage, S., Naumann, R., Behrendt, R., and Roers, A. (2012) Mammalian RNase H2 removes ribonucleotides from DNA to maintain genome integrity. *J. Exp. Med.*, **209**, 1419–1426
38. Bartsch, K., Knittler, K., Borowski, C., Rudnik, S., Damme, M., Aden, K., Spehlmann, M.E., Frey, N., Saftig, P., Chalaris, A., and Rabe, B. (2017) Absence of RNase H2 triggers generation of immunogenic micronuclei removed by autophagy. *Hum. Mol. Genet.*, **26**, 3960–3972
39. Crow, Y.J., Chase, D.S., Schmidt, J.L., et al. (2015) Characterization of human disease phenotypes associated with mutations in *TREX1*, *RNASEH2A*, *RNASEH2B*, *RNASEH2C*, *SAMHD1*, *ADAR*, and *IFIH1*. *Am. J. Med. Genet. A.* **167A**, 296–312
40. Parniak, M.A., Min, K.L., Budihas, S.R., Le Grice, S.F., and Beutler, J.A. (2003) A fluorescence-based high-throughput screening assay for inhibitors of human immunodeficiency virus-1 reverse transcriptase-associated ribonuclease H activity. *Anal. Biochem.*, **322**, 33–39
41. Gao, Y. and Yang, W. (2016) Capture of a third Mg^{2+} is essential for catalyzing DNA synthesis. *Science*, **352**, 1334–1337

42. Yang, W., Weng, P.J., and Gao, Y. (2016) A new paradigm of DNA synthesis: three-metal-ion catalysis. *Cell Biosci*., **6**, 51
43. Yoon, H. and Warshel, A. (2017) Simulating the fidelity and the three Mg mechanism of pol η and clarifying the validity of transition state theory in enzyme catalysis. *Proteins*, **85**, 1446–1453
44. Okano, H., Baba, M., Hidese, R., Iida, K., Li, T., Kojima, K., Takita, T., Yanagihara, I., Fujiwara, S., and Yasukawa, K. (2018) Accurate fidelity analysis of the reverse transcriptase by a modified next-generation sequencing. *Enzyme Microb. Technol.*, **115**, 81–85
45. Arakawa, T., Ejima, D., Tsumoto, K., Ishibashi, M., and Tokunaga, M. (2007) Improved performance of column chromatography by arginine: Dye-affinity chromatography. *Protein Expr. Purif.*, **52**, 410–414
46. Günther, C., Kind, B., Reijns, M.A., Berndt, N., Martinez-Bueno, M., Wolf, C., Tü ngler, V., Chara, O., Lee, Y.A., Hübner, N., Bicknell, L., Blum, S., Krug, C., Schmidt, F., Kretschmer, S., Koss, S., Astell, K.R., Ramantani, G., Bauerfeind, A., Morris, D.L., Cunninghame Graham, D.S., Bubeck, D., Leitch, A., Ralston, S.H., Blackburn, E.A., Gahr, M., Witte, T., Vyse, T.J., Melchers, I., Mangold, E., Nöthen, M.M., Aringer, M., Kuhn, A., Lüthke, K., Unger, L., Bley, A., Lorenzi, A., Isaacs, J.D., Alexopoulou, D., Conrad, K., Dahl, A., Roers, A., Alarcon-Riquelme, M.E., Jackson, A.P., and Lee-Kirsch, M.A. (2015) Defective removal of ribonucleotides from DNA promotes systemic autoimmunity. *J. Clin. Invest.*, **125**, 413–424
47. Aden, K., Bartsch, K., Dahl, J., Reijns, M.A.M., Esser, D., Sheibani-Tezerji, R., Sinha, A., Wottawa, F., Ito, G., Mishra, N., Knittler, K., Burkholder, A., Welz, L., van Es, J., Tran, F., Lipinski, S., Kakavand, N., Boeger, C., Lucius, R., von

Schoenfels, W., Schafmayer, C., Lenk, L., Chalaris, A., Clevers, H., Röcken, C., Kaleta, C., Rose-John, S., Schreiber, S., Kunkel, T., Rabe, B., and Rosenstiel, P. (2019) Epithelial RNase H2 maintains genome integrity and prevents intestinal tumorigenesis in mice. *Gastroenterology*, **156**, 145–159

48. Hyjek, M., Figiel, M., and Nowotny, M. (2019) RNase H: Structure and mechanism. *DNA Repair*, **84**, 102672
49. Steitz, T.A. (1999) DNA polymerases: structural diversity and common mechanisms. *J. Biol. Chem.*, **274**, 17395–17398
50. Zhang, L., Zhou, Y., Cheng, C., Cui, H., Cheng, L., Kong, P., Wang, J., Li, Y., Chen, W., Song, B., Wang, F., Jia, Z., Li, L., Li, Y., Yang, B., Liu, J., Shi, R., Bi, Y., Zhang, Y., Wang, J., Zhao, Z., Hu, X., Yang, J., Li, H., Gao, Z., Chen, G., Huang, X., Yang, X., Wan, S., Chen, C., Li, B., Tan, Y., Chen, L., He, M., Xie, S., Li, X., Zhuang, X., Wang, M., Xia, Z., Luo, L., Ma, J., Dong, B., Zhao, J., Song, Y., Ou, Y., Li, E., Xu, L., Wang, J., Xi, Y., Li, G., Xu, E., Liang, J., Yang, X., Guo, J., Chen, X., Zhang, Y., Li. Q,, Liu. L,, Li. Y., Zhang, X., Yang, H., Lin, D., Cheng, X., Guo, Y., Wang, J., Zhan, Q., and Cui, Y. (2015) Genomic analyses reveal mutational signatures and frequently altered genes in esophageal squamous cell carcinoma. *Am. J. Hum. Genet.* **96**, 597–611
51. Arudchandran, A., Cerritelli, S.M., Narimatsu, S., Itaya, M., Shin, D.Y., Shimada, Y., and Crouch, R.J. (2000) The absence of ribonuclease H1 or H2 alters the sensitivity of *Saccharomyces cerevisiae* to hydroxyurea, caffeine and ethyl methanesulphonate: implications for roles of RNases H in DNA replication and repair. *Genes Cells*, **5**, 789–802
52. Nick McElhinny, S.A., Watts, B.E., Kumar, D., Watt, D.L., Lundström, E.B.,

Burgers, P.M., Johansson, E., Chabes, A., and Kunkel, T.A. (2010) Abundant ribonucleotide incorporation into DNA by yeast replicative polymerases. *Proc. Natl. Acad. Sci. USA*, **16**, 4949–4954

53. Härtlova, A., Erttmann, S.F., Raffi, F.A., Schmalz, A.M., Resch, U., Anugula, S., Lienenklaus, S., Nilsson, L.M., Kröger, A., Nilsson, J.A., Ek, T., Weiss, S., and Gekara, N.O. (2015) DNA damage primes the type I interferon system via the cytosolic DNA sensor STING to promote anti-microbial innate immunity. *Immunity*, **42**, 332–343
54. Pizzi, S., Sertic, S., Orcesi, S., Cereda, C., Bianchi, M., Jackson, A.P., Lazzaro, F., Plevani, P., and Muzi-Falconi, M. (2015) Reduction of hRNase H2 activity in Aicardi-Coutières syndrome cells leads to replication stress and genome instability. *Hum. Mol. Genet.*, **24**, 649–658
55. Bartsch, K., Damme, M., Regen, T., Becker, L., Garrett, L., Hölter, S.M., Knittler, K., Borowski, C., Waisman, A., Glatzel, M., Fuchs, H., Gailus-Durner, V., Hrabe de Angelis, M., and Rabe, B. (2018) RNase H2 loss in murine astrocytes results in cellular defects reminiscent of nucleic acid-mediated autoinflammation. *Front. Immunol.*, **9**, 587
56. Rabe, B. (2013) Aicardi-Goutières syndrome: clues from the RNase H2 knock-out mouse. *J. Mol. Med.*, **91**, 1235−1240
57. Kalhorzadeh, P., Hu, Z., Cools, T., Amiard, S., Willing, E.M., De Winne, N., Gevaert, K., De Jaeger, G., Schneeberger, K., White, C.I., and De Veylder, L. (2014) *Arabidopsis thaliana* RNase H2 deficiency counteracts the needs for the WEE1 checkpoint kinase but triggers genome instability. *Plant Cell*, **26**, 3680−3692

58. Naimuddin, M., Kurazono, T., Zhang, Y., Watanabe, T., Yamaguchi, M., and Nishigaki, K. (2000) Species-identification dots: a potent tool for developing genome microbiology. *Gene*, **261**, 243−250

59. Kouduka, M., Matuoka, A., and Nishigaki, K. (2006) Acquisition of genome information from single-celled unculturable organisms (radiolaria) by exploiting genome profiling (GP). *BMC Genomics*, **7**, 135

60. Kouduka, M., Sato, D., Komori, M., Kikuchi, M., Miyamoto, K., Kosaku, A., Naimuddin, M., Matsuoka, A., and Nishigaki, K. (2007) A solution for universal classification of species based on genomic DNA. *Int. J. Plant Genomics*, **2007**, 27894

61. Ahmed, S., Komori, M., Tsuji-Ueno, S., Suzuki, M., Kosaku, A., Miyamoto, K., and Nishigaki, K. (2011) Genome profiling (GP) method based classification of insects: congruence with that of classical phenotype-based one. *PLoS One*, **6**, e23963

62. Hamano, K., Ueno-Tsuji, S., Tanaka, R., Suzuki, M., Nishimura, K., and Nishigaki, K. (2012) Genome profiling (GP) as an effective tool for monitoring culture collections: A case study with *Trichosporon*. *J. Microbiol. Methods*, **89**, 119−128

63. Suwa, N., Ikegaya, H., Takasaka, T., Nishigaki, K., and Sakurada, K. (2012) Human blood identification using the genome profiling method. *Leg. Med.*, **14**, 121−125

64. Diwan, D., Komazaki, S., Suzuki, M., Nemoto, N., Aita, T., Satake, A., and Nishigaki, K. (2014) Systematic genome sequence differences among leaf cells within individual trees. *BMC Genomics*, **15**, 142

65. Sharma, H., Ohtani, F., Kumari, P., Diwan, D., Ohara, N., Kobayashi, T., Suzuki, M., Nemoto, N., Matsushima, Y., and Nishigaki, K. (2014) Familial clustering of

mice consistent to known pedigrees enabled by the genome profiling (GP) method. *Biophysics*, **10**, 55−62

66. Diwan, D., Masubuchi, Y., Furukawa, T., and Nishigaki, K. (2016) Ordered genome change of plant and animal body cells revealed by the genome profiling method. *FEBS Lett*., **590**, 2119−2126
67. Sakuma, Y. and Nishigaki, K. (1994) Computer prediction of general PCR products based on dynamical solution structures of DNA. *J. Biochem*., **116**, 736−741
68. Nishigaki, K., Naimuddin, M., and Hamano, K. (2000) Genome profiling: a realistic solution for genotype-based identification of species. *J. Biochem*., **128**, 107−112
69. Nishigaki, K., Saito, A., Hasegawa, T., and Naimuddin, M. (2000) Whole genome sequence-enabled prediction of sequences performed for random PCR products of *Escherichia coli*. *Nucleic Acids Res*., **28**, 1879−1884
70. Biyani, M. and Nishigaki, K. (2001) Hundredfold productivity of genome analysis by introduction of microtemperature-gradient gel electrophoresis. *Electrophoresis*, **22**, 23−28
71. Hesbert, A., Bottin, M.C., de Ceaurriz, J., Protois, J.C., and Cavelier, C. (1984) Testing natural indigo for genotoxicity. *Toxicol. Lett.*, **21**, 119−125
72. Salimullah, M., Hamano, K., Tachibana, M., Inoue, K., and Nishigaki, K. (2005) Efficient SNP analysis enabled by joint application of the μTGGE and heteroduplex methods. *Cell. Mol. Biol. Lett*., **10**, 237−245
73. Meek, B. and Doull, J. (2009) Pragmatic challenges for the vision of toxicity testing in the 21st century in a regulatory context: another Ames test? . . . or a new edition of ‘‘the Red Book’’? *Toxicol. Sci*., **108**, 19−21

Acknowledgements

This study was carried out in Laboratory of Enzyme Chemistry, Division of Food Science and Biotechnology, Graduate School of Agriculture, Kyoto University.

I am deeply grateful to Dr. Kiyoshi Yasukawa, Professor of Kyoto University, for his invaluable guidance, kind support, and constant encouragement.

I am indebted to Dr. Teisuke Takita, Assistant Professor of Kyoto University, for his incisive comments and moral support.

I acknowledge to Dr. Kenji Kojima, Assistant Professor of Kyoto University, for his useful advice and careful tutelage.

I thank all other members of Laboratory of Enzyme Chemistry.

I also thank Dr. Koichi Nishigaki, Dr. Manish Biyani, and Dr. Parmila Kumari for their technical advice and helpful discussion.

This study was supported by Grant-in-Aid for Scientific Research from Japan Society for the Promotion of Science (no. 18J14339).

Finally, I give special thanks to my family and friends for their assistance and encouragement.

March 2020

Misato Baba

List of publications

1. Baba, M., Kojima, K., Nakase, R., Imai, S., Yamasaki, T., Takita, T., Crouch, R. J., and Yasukawa, K. (2017) Effects of neutral salts and pH on the activity and stability of human RNase H2. *J. Biochem.*, **162**, 211–219
2. Nishimura, T., Baba, M., Ogawa, S., Kojima, K., Takita, T., Crouch, R. J., and Yasukawa, K. (2019) Characterization of six recombinant human RNase H2 bearing Aicardi-Goutiéres syndrome causing mutations. *J. Biochem.,* **166**, 537–545
3. Baba, M., Kojima, K., Nishimura, T., Sugiura, T., Takita, T., Uehara, R., Crouch, R. J., and Yasukawa, K. Val143 of human ribonuclease H2 is not critical for, but plays a role in determining catalytic activity and substrate specificity. *PLoS one* in revision
4. Tsukiashi, M., Baba, M., Kojima, K., Himeda, K., Teisuke, T., and Yasukawa, K. (2019) Construction and characterization of ribonuclease H2 knockout NIH3T3 cells. *J. Biochem*., **165**, 249–256
5. Kumari, P.*, Gautam, S. G.*, Baba, M.*, Tsukiashi, M., Matsuoka, K., Yasukawa, K., and Nishigaki, K. (2017) DNA-based mutation assay GPMA (genome profiling-based mutation assay): reproducibility, parts-per-billion scale sensitivity, and introduction of a mammalian-cell-based approach. *J. Biochem.*, **162**, 395–401. *equally contributed to this paper